Ship Roll Damping Analysis

Von der Fakultät für Ingenieurswissenschaften,

Abteilung Maschinenbau und Verfahrenstechnik,

der Universität Duisburg-Essen

zur Erlangung des akademischen Grades

eines

Doktors der Ingenieurswissenschaften

Dr.-Ing.

genehmigte Dissertation

von

Henry Peter Piehl

aus

Hamburg

Gutachter: Prof. Dr.-Ing. Bettar Ould el Moctar
Prof. Dr.-Ing. Moustafa Abdel-Maksoud

Tag der mündlichen Prüfung: 22. April 2016

Contents

List of Figures

List of Tables

Nomenclature

α	volume fraction
α, β, γ	differential equation coefficients
$G\bar{M}$	metazentric height
$\beta = \mathrm{Re/K}$	Stokes parameter
$\boldsymbol{\beta} = [\beta_1, \beta_2, \ldots]$	unknown regression coefficients
$\boldsymbol{\epsilon}$	error vector
$\mathbf{\Phi}$	matrix derivative
$\ddot{\mathbf{x}}$	second time derivative
$\ddot{\phi}$	roll acceleration
Δ	displacement (buoyancy)
δ	natural linear damping coefficient
$\delta(x, y)$	Dirac point source
δ_0	dimensionless natural linear damping coefficient
δ_{ij}	discrete Dirac point source
$\dot{\mathbf{x}}$	first time derivative
$\dot{\phi}$	angular roll velocity
$\dot{u}$	velocity derivative (acceleration)
ϵ	turbulent dissipation rate
η	dynamic viscosity
Γ	domain boundary
$\hat{\omega}$	dimensionless characteristic angular frequency
$\hat{B}_{44}$	dimensionless roll damping coefficient
λ	ship model scale
$\mathbf{A}$	mass or inertia matrix
$\mathbf{A}\boldsymbol{\lambda} = \mathbf{b}$	linear system of equations
$\mathbf{B}$	damping matrix
$\mathbf{b}$	dependent variable vector
$\mathbf{C}$	hydrostatic restoring matrix
$\mathbf{f}$	volume force
$\mathbf{F}(\mathbf{z})$	vector function
$\mathbf{G}$	fundamental solution matrix
$\mathbf{J}(\mathbf{z})$	Jacobian matrix
$\mathbf{n}$	normal direction
$\mathbf{P}$	parameter matrix

$\mathbf{u}$ ..... velocity vector
$\mathbf{u}_i'$ ..... RANS velocity fluctuation
$\mathbf{x}$ ..... motion state vector
$\mathcal{V}$ ..... rotational energy
μ ..... dynamic viscosity
∇ ..... displacement (volume)
ν ..... kinematic viscosity
Ω ..... computational domain
ω ..... angular velocity
ω ..... turbulent frequency
ω_0,ω_n ..... natural angular velocity
$\overline{\mathbf{u}_i}$ ..... RANS mean velocity
ϕ ..... roll angle
$\phi(t)$ ..... time dependent roll angle
$\phi(t_i)$ ..... roll angle time series
ϕ_0, $\hat{\phi}$ ..... initial roll angle
ϕ_A ..... roll angle amplitude
ϕ_i,ϕ_{i+1} ..... consecutive roll angle maxima
ϕ_{res} ..... resulting roll amplitude
ϕ_{stat} ..... static roll amplitude
ρ ..... density
Co ..... Courant number
Fr ..... Froude number
KG ..... center of gravity over base line
K ..... Keulegan-Carpenter number
LCB ..... longitudinal center of gravity
raz ..... roll axis height over waterlevel
Re ..... Reynolds number
Θ ..... time in radian
φ ..... flow potential
A ..... reference area
A_ϕ ..... linear inertia coefficient
a_k, b_k ..... Fourier transformation coefficients
B ..... total roll damping coefficient
$B()$ ..... roll damping equation
B_{e} ..... equivalent damping coefficient
B_{44} ..... roll damping coefficient
$B_\phi(\dot{\phi})$ ..... nonlinear roll damping function
B_{BK} ..... bilge keel damping coefficient
B_{E} ..... eddy damping coefficient

B_{F} ..... friction damping coefficient
$B_{\mathrm{geo}}()$ ..... geometric roll damping function
$B_{\mathrm{kin}}()$ ..... kinematic roll damping function
B_{L} ..... lift damping coefficient
B_{ship} ..... ship breadth
B_{W} ..... wave damping coefficient
$C(\phi)$ ..... restoring moment function
C_1,C_3,C_5 ..... polynomial restoring moment coefficients
C_D ..... drag coefficient
C_F ..... friction coefficient
C_F, C_f ..... friction coefficient
C_L ..... lift coefficient
C_M ..... inertia coefficient
C_R ..... residual coefficient
C_T ..... total resistance coefficient
$C_{\mathrm{f,ITTC}}$ ..... ITTC friction coefficient
$F(t)$ ..... time dependent force
$F(x, y)$ ..... derivative of $G(x, y)$
F_b ..... buoyancy force
F_D ..... drag force
F_G ..... weight force
F_L ..... lift force
F_m ..... measured force
F_p ..... pressure force
F_V ..... viscous force
$G(x, y)$ ..... fundamental solution of potential problem
g_{ij} ..... discrete fundamental solution
$GZ(\phi)$ ..... righting arm function
I ..... turbulent intensity
I_{add} ..... added mass inertia
I_{hull} ..... moment of inertia of ship
I_{xx},I_ϕ ..... total moment of inertia
k ..... turbulent kinetic energy
k_{xx} ..... radius of gyration
L ..... linear momentum
l ..... turbulent length scale
L_{PP} ..... length between perpendicular
L_{WL} ..... length water line
m ..... mass
M_ϕ ..... roll moment

M_{err} ..... excitation moment
M_{dyn} ..... dynamic roll moment
M_{res} ..... resulting total roll moment
M_{sim} ..... simulated roll moment
M_{stat} ..... hydrostatic roll moment
N ..... Bertin damping coefficient
N_{eff} ..... damping coefficient
p ..... pressure
P_α ..... parameter variation set with multiindex
R_F ..... friction force
R_T ..... total resistance force
S ..... surface area
S_{wet} ..... wetted surface
T ..... draft
t ..... time
T_0 ..... natural roll period
T_{cyc} ..... periodic cycle length
T_{roll} ..... roll period
t_i ..... discrete time steps
U ..... characteristic velocity
$u(t)$ ..... time dependent velocity
U_A, U_m ..... velocity amplitude
V ..... domain
x ..... coordinate axis direction along ship
y ..... coordinate axis direction port side
y,$\dot{y}$,$\ddot{y}$ ..... ODE variable, first and second derivative
y^+ ..... dimensionless wall distance
z ..... coordinate axis direction upward

1. Introduction

The increased demand for transport capacity led to new container ship designs with a large bow flare that are able to carry more containers. These new hull shapes influence the ship stability and may lead to large roll angle amplitudes, which lead to high accelerations and thereby to a high safety risk for human life, ship and cargo.

One example for the severe danger of large roll angles is the 1998 incident of the APL China in a storm near the Aleutian Islands. The large stern and bow flare are considered to be the reasons for the onset of parametric rolling which eventually led to the loss of almost 400 containers and structural ship damage.

The roll motion of a ship around its longitudinal axis can be regarded as a dynamical system. The energy and motion state of this system defined by roll angle ϕ, roll angle velocity $\dot{\phi}$ and angular acceleration $\ddot{\phi}$. The properties of the roll motion behavior are determined by the ship hull shape, the mass distribution and the motion of the surrounding water. When energy (in form of wind, wave or current) is fed into the roll motion system, the roll angle amplitude ϕ_A increases. The reverse effect of a loss of energy, that decreases the roll angle amplitude, is termed *roll damping* and is caused by many flow effects: wave radiation, viscous friction, eddy separation, lift effects, etc. To be able to predict or prevent large roll angles and roll acceleration, it is important to understand the physical principals of roll motion and especially roll damping.

The assessment of dynamic stability of ships in the early design phase is needed. In today's naval engineering practice, the roll motion of a ship is computed with computational methods based on the potential theory. These methods are sufficiently fast for ship design purposes. However, they lack the ability to predict viscous roll damping, which has to be determined with other means such as model tests, viscous field methods or empirical prediction methods. Physical tests, in turn, are costly, time consuming and suffer from scale effects.Empirical methods such as the Ikeda method are also restricted in their use, as their development was based on a restricted number of hull shapes (e.g. slender bodies) and may not be valid for modern ship designs.

Another approach to compute the roll damping is the use of computational fluid dynamic (CFD) methods that numerically solve the flow problem based on Reynolds averaged Navier-Stokes (RANS) equations. However, the high computational costs prevents its use in the design phase.

The demand for a roll damping prediction method and the above described deficit in the current roll damping assessment methods led to the objective of this thesis:

a) Deeper analysis of the roll damping mechanisms by investigating the governing equation and identifying the influencing factors of the roll damping coefficients of modern hull shapes.

b) Development of a mathematical model for the roll damping prediction of modern ship hulls.

The research approach to achieve these objectives is, first, to conduct numerical roll damping analysis for a systematic variation of hull shapes. Second, to apply a nonlinear regression analysis method in order to derive a mathematical roll damping prediction model.

The following paragraph provide a short overview of the structure of this thesis and the covered topics:

2. Background Chapter 2 provides an overview of the governing equations for fluid and rigid body dynamics, numerical and experimental test procedures and the most common roll damping analysis and prediction methods.

3. Mathematical Model Chapter 3 introduces the concept for the development of the prediction model and the mathematical treatment of ship roll motion. A second order ordinary differential equation (ODE) is solved to compute the roll motion. This chapter presents the basic model assumptions, a method for the analytical solution of linear ODE's and the numerical computation of arbitrary nonlinear ODE's. The main part of the chapter focuses on the analysis of roll motion time series and the determination of the roll damping coefficients. Two methods for predicting the inertia and restoring moments are presented in the last part of the chapter.

4. Viscous Roll Damping The theory and computation of viscous roll motion using the finite volume method (FVM), turbulence modeling and fluid-rigid body interaction are addressed in chapter 4. The theoretical part is followed by a presentation of several case studies that were used to validate the computational methods with the results of experimental model tests. The chapter concludes with a description of the simulation method of *forced roll motion* which is used in fifth chapter for the systematic investigation.

5. Regression Analysis Chapter 5 contains a description of the hull shape variation and the computation of a database with the results of the systematic roll damping simulations. The development of the mathematical roll damping model is based on a regression analysis of the obtained roll damping coefficient.

The thesis concludes with a summary of the development procedure for the mathematical model, the used methods and the achieved results. The section is followed by an assessment of the model limitations and an outlook on further research.

The topic of this thesis originates from the work in the research project *MatRoll* which was part of the joint research collaboration *Best-Roll*. The research field of Best-Roll covered the model tests, PIV measurements, development roll damping prediction methods and application and further development of RANS-CFD methods.

The current study is closely related to the final project report and several conference articles published within the scope of the MatRoll project:

[2] Piehl, H., and el Moctar, O., 2015. *Development of a Mathematical Roll Damping Model with Polynomial Regression Analysis*. Proceedings of the ASME 2015 34th International Conference on Ocean, Offshore and Arctic Engineering, St. John's, Canada.

[3] Piehl, H., and el Moctar, O., 2014. *Bilge keel forces and vortex shedding – a numerical analysis with openfoam*. Proceedings of the ASME 2014 33rd International Conference on Ocean, Offshore and Arctic Engineering, San Francisco, USA.

[4] Piehl, H., and el Moctar, O., 2013. *Entwicklung von mathematischen Modellen zur Berechnung der Rolldämpfung moderner Schiffsformen – Mat-Roll/ Best-Roll*. BMWi Forschungsprogramm – Schiffahrt und Meerestechnik für das 21. Jahrhundert; final report.

[5] Piehl, H., and el Moctar, O., 2013. *Roll decay model test of a post panamax container ship – experimental and numerical analysis*. Proceedings of the ASME 2013 32nd International Conference on Ocean, Offshore and Arctic Engineering, Nantes, France.

[6] Piehl, H., and el Moctar, O., 2012. *Vortex shedding from a bilge keel in a transient turbulent flow*. Proceedings of the ASME 2012 31st International Conference on Ocean, Offshore and Arctic Engineering, Rio de Janeiro, Brazil.

[7] Piehl, H., Höpken, J., and el Moctar, O., 2011. *Influence of shape variation on hydrodynamic damping of rigid body motion*. Proceedings of the 14th Numerical Towing Tank Symposium, Poole, United Kingdom.

2. Background

Before being able to develop a mathematical roll damping prediction model, the state of the art and theoretic background of roll motion analysis needs to be summarized. The chapter begins with the governing equations of the two physical principles that are linked to ship roll motion: the dynamic motion of the hull itself and the fluid flow around the hull. Next, the different roll motion test methods are described. Finally the principle of the *damping* of the roll motion and the most common methods to assess the amount of roll damping are described. Instead of the different mathematical notations that are used in most of the publications a uniform notation is used in the following sections.

Some of the reviewed publications date back to the early 1950s ([8]) and even before (Froude 1862 [9]), but regardless of their maybe outdated methods, their analytical formulations help to identify the main influence parameter and provide good insight into the fundamental principles of ship roll motion.

Over time the importance of the computer has increased dramatically. Early publications on roll motion use exclusively analytical models, but beginning with the 1950s, computers were used more and more. Initially, just for the numerical simulation of the roll motion equation, then to compute the shape coefficients of ship sections.

Later, with the development of two- and three-dimensional potential theory based methods, the computer is used to determine the inertia coefficients and restoring moments. With the development of viscous field methods it was possible to simulate the three-dimensional flow around a rolling ship.

2.1. Ship Motion

In naval architecture the term *rolling* defines the motion of a ship around its longitudinal axis. In Fig. 2.1 the outline of the Duisburg test case (DTC) with the position and orientation of the ship coordinate system is shown. The origin is placed at the intersection of base line and aft perpendicular. The roll angle is defined as a rotation around the x-axis. The actual roll axis of rolling ship is an non-stationary axis parallel to the x-axis.

Figure 2.2 shows the outline of the inclined main section (indicated in the middle of Fig. 2.1) of the DTC (el Moctar et al. [10])and the forces acting on the hull.

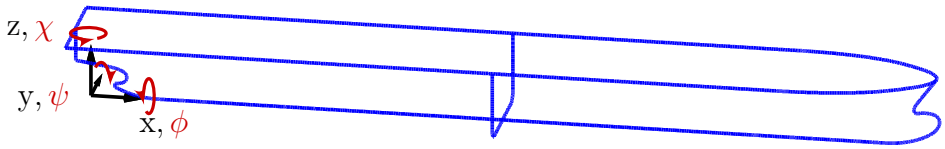

Figure 2.1.: Outline of the Duisburg test case with position and orientation of the ship coordinate system.

Two components of the fluid forces are shown in the figure: the pressure force F_p in normal direction to the hull surface and the friction force F_f in tangential direction. The integration of the fluid forces over the hull surface generate a buoyancy force F_b and a restoring moment M_ϕ around a longitudinal-axis through the center of buoyancy (black circle at the point of application of F_b). If the hull is in an equilibrium state with zero motion velocity the viscous force is also zero and the pressure force consist only of the hydrostatic pressure. In this case the weight force F_g and the buoyancy force cancel each other out.

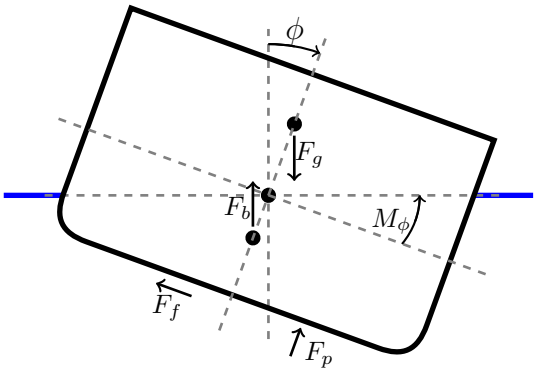

Figure 2.2.: Forces and moments acting on a heeling ship

In order to derive a mathematical roll damping model from experiments or numerics, the ship roll motion has to be analyzed. If the ship is assumed to be a rigid body its motion can be described with Newton's law of motion, forming a system of second order ordinary differential equations (2.1). With this set of equations the ship motion can be computed depending on external forces.

Equation (2.1) states the motion equation form for six degrees of freedom (three translational and three rotational). The bold lower case letters indicate vectors and capital letters matrices which contain the linearized hull coefficients for the inertia, damping and restoring terms. The motion state of a body depends on the position vector $\mathbf{x}$ and the velocity vector $\dot{\mathbf{x}}$.

$$\mathbf{A}\ddot{\mathbf{x}} + \mathbf{B}\dot{\mathbf{x}} + \mathbf{C}\mathbf{x} + \mathbf{f} = 0 \tag{2.1}$$

The first term on the left side of Eq. (2.1) denotes the inertia forces depending on the vector of acceleration $\ddot{\mathbf{x}}$ and the mass matrix $\mathbf{A}$ containing the inertial coefficients. The second term contains the damping forces depending on the velocity $\dot{\mathbf{x}}$ and the damping matrix $\mathbf{B}$. The third term denotes the restoring force, depending on the position vector $\mathbf{x} = [x, y, z, \phi, \theta, \psi]$ and restoring matrix $\mathbf{C}$, containing the hydrostatic coefficients.

Table 2.1.: Degrees of freedom of a ship

j	direction of motion	axis	symbol
1	surge	translation along x	x
2	sway	translation along y	y
3	heave	translation along z	z
4	**roll**	**rotation around x**	$\boldsymbol{\phi}$
5	pitch	rotation around y	ψ
6	yaw	rotation around z	χ

Table 2.1 lists the six degrees of freedom (DoF) with a description and their symbol. In order to simplify the investigation of the roll motion, Eq. (2.1) is reduced to a single differential equation with one degree of freedom:

$$\underbrace{I\ddot{\phi}}_{\text{inertia}} + \underbrace{B\dot{\phi}}_{\text{damping}} + \underbrace{\rho g \nabla \overline{GZ}(\phi)}_{\text{restoring}} = \underbrace{M_\phi}_{\text{external}} \tag{2.2}$$

In this one dimensional notation (Eq. (2.2)), the roll angle ϕ is the only free variable. The structure of the equation is the same as in the system of equations in Eq. (2.1). The coefficients of the equation are the moment of inertia I, the roll damping coefficient B, the fluid density ρ, the displacement ∇ and the function of the righting arm $\overline{GZ}(\phi)$. For small roll angles $\overline{GZ}(\phi)$ can be linearized to $\overline{GM}_t\phi$.

The numerical solution of the equation of motion (with a fixed axis, Eq. (2.2)) or in general for six degrees of freedom (Eq. (2.1)) also belongs to the category of numerical methods. In most publications the numerical solution of the differential equation is computed with multi stage Runge-Kutta time integration schemes. The results of the computations are time series of the roll angle which can be used to determine the quality of the roll damping model or to derive the roll damping coefficients (Bass, Haddara [11], Spouge [12], Chan, Xu und Huang [13], Schmitke [14], Roberts [15], Taylan [16], Umeda [17] and Jang [18]).

2.2. Fluid Dynamics

The viscous, incompressible flow around a rolling ship can be determined by solving the Navier-Stokes (NS) equations. The NS equations are defined by a set of coupled equations: the conservation of momentum (2.4) and the continuity equation (2.3) (Kundu and Cohen [19]). They depend on the flow velocity vector $\mathbf{u}$, the scalar pressure p and the volume force $\mathbf{f}$ (eg. gravitation). The fluid properties are defined by the density ρ and the kinematic viscosity ν.

$$\nabla \cdot \mathbf{u} = 0 \tag{2.3}$$

$$\underbrace{\frac{\partial \mathbf{u}}{\partial t}}_{\text{time derivative}} + \underbrace{(\mathbf{u} \cdot \nabla)\,\mathbf{u}}_{\text{convection}} = \underbrace{-\frac{1}{\rho}\nabla p}_{\text{pressure gradient}} + \underbrace{\nu \Delta \mathbf{u}}_{\text{diffusion}} + \underbrace{\frac{1}{\rho}\mathbf{f}}_{\text{volume force}} \tag{2.4}$$

Equation (2.3) and (2.4) state the incompressible (constant density), isothermal, unsteady Navier-Stokes equations in their differential form. The first term of Eq. (2.4) is the time derivative of the velocity. This – so called *inertial term* – indicates that the flow is time dependent and therefore a transient numerical solver has to be used to simulate the flow.

In order to account for ship buoyancy and water waves a two-phase flow problem with a free interface (water surface) has to be solved. A common approach to numerically model the free interface is the volume of fluid (VOF) method [20].

Due to the viscous stress near a wall, a turbulent boundary layer (Pope [21] and Schlichting [22]) is build up, that influences the roll damping of the ship hull. In addition to the friction of the boundary layer, the viscosity can lead to the shedding of large vortex structures which decrease the kinetic energy of a moving ship, thus *damping* the roll motion.

A characteristic measure for the turbulence of a flow is the Reynolds number *Re* Eq. (2.5). This dimensionless quantity is defined as quotient of inertia and viscous forces. It is defined by the velocity magnitude U_A, a characteristic length L and the kinematic viscosity ν. If the flow direction is tangential to the ship hull or wall, the length L is defined as length of the body while in the case of a flow in normal direction to the wall L is the width of the body. *Re* allows to estimate the shear stress magnitude and is used to estimate whether a flow is laminar or how strong the turbulence intensity is.

$$\mathrm{Re} = \frac{U_A L}{\nu} \tag{2.5}$$

$$\mathrm{Fr} = \frac{U_A}{\sqrt{gL}} \tag{2.6}$$

$$\mathrm{K} = \frac{U_A T}{L} \tag{2.7}$$

In addition, the Reynolds number is used to scale the flow conditions in a model test to create similar turbulent conditions as in the flow around a full scale ship.

For a full scale ship hull the Reynolds number is of the magnitude of $Re = 10^9$. For this Re-magnitude and size of computational domain the turbulent behavior of a fluid has to be modeled with a turbulence model (Ferziger and Perić [23] and in Versteeg and Malalasekera [24]). A direct numerical simulation (DNS) of a full ship is almost impossible.

Another important flow quantity is the Froude number Fr (Eq. (2.6)), which depends on U_A and L as well, but also on the gravitation constant g (instead of ν as in Re). The Froude number Fr represents the quotient of the inertia force and a gravitational force and allows to relate the velocity of a ship to the propagation speed of water waves.

To further characterise a dynamic, oscillating flow, a third property, the Keulegan-Carpenter number K (Eq. (2.7)) is used. This number sets velocity U_A and length L in relation to the time period T of an oscillating flow.

2.2.1. Computational Fluid Dynamics

In practice, roll motion simulations based on potential flow theory are still state of the art. Potential flow solver are used to compute the inertia coefficients and to predict the diffraction and radiation of waves around a ship hull (see Ursell [8], Salvesen et al. [25], Salvesen [26] and Zhang et al. [27]). In a potential flow the fluid is assumed to be inviscid and irrotational. However, potential theory may be used to obtain the added mass coefficients and the roll damping due to radiated waves.

State of the art potential flow methods are 2D strip and 3D panel methods. An advantage of the strip method is its – in comparison to three-dimensional panel methods – shorter computation time and less complex implementation. The drawback is, that wave radiation and lift effects due to forward speed are not considered.

Parallel to the increasing computer power, numerical field methods for the simulation of ship motion were developed. The numerical methods used in the literature vary in their complexity and ability to account for a different flow phenomena (eg. two phase flow, turbulence, ship motion). Jaouen [28] simulated a forced roll motion in 2D without free surface effects to investigate roll damping. Main feature of the investigation of Graham [29] was the coupling of a viscous field method in close range to a rectangular cross section with a potential flow solver for the far-field. In 2005, Kluwe and Schmode [30] used a bilge keel attached to a cylindrical hull to simulate roll motion without free-surface effects. And in 2011 Bonfiglio [31] used OpenFOAM with RANS and free surface to compute the flow around a rolling 2D hull section.

The mesh-free vortex method is mainly used for 2D cases. Graham [32] and Brown [33] used this method to compute the vortex shedding from a roll hull

section. Seah, Celano and Yeung [34] coupled their vortex method with a rigid body model to simulate the roll decay of a floating cylinder.

2.3. Experimental Methods

Three different test methods are used to investigate roll damping behavior [35]:

1. In the **roll decay** test, a free floating ship (model or full scale) is inclined to a certain roll angle ϕ_0 and is then released. The ship begins a roll oscillation with a decaying amplitude (see section 2.3.1).

2. The method of the **forced moments** uses also a free floating ship model but for this test the roll motion is driven by an external oscillating moment.

3. The **forced motion** test uses a model that is fixed to a gear that rotates with a prescribed oscillating roll motion. In contrast to the two previous methods during this test instead of the roll angle the reaction moment of the fluid is measured.

Full scale test are rare, in most publications the roll damping analysis is applied to model test results. In order to investigate general principles of roll damping, tests with simplified model hulls are used [1]. While Blume [35] used model ships, the hull shapes in these cases are often a simple prismatic body with the cross section shape of a ship hull. To test the roll damping behavior the hull sections are forced to perform a harmonic roll motion and the reaction moment is measured and analyzed. Ikeda used partly or fully submerged prismatic ship section for these tests (Ikeda [36], Tanake [37], [38], [39], [40]). In [41], Ikeda used a rotating 3D ellipsoid. Jung [18] conducted roll decay tests with prismatic ship sections and investigated the vortex shedding at the bilge keel with particle image velocimetry (PIV). One of the rare full scale roll decay tests found in literature were analyzed by Schmitke [14]. A naval vessel was inclined to an initial roll angle by a large ex-centric weight and the roll damping was derived from the decreasing amplitudes and time period of the roll motion.

Apart measurements in a test facility with well known environmental conditions, it is possible to measure the roll motion due to roll excitation in natural sea ways. Here, however, the test conditions cannot be controlled.

2.3.1. Roll Decay

From a practical perspective, roll decay tests with zero ships speed are relatively easy to conduct. The model ship is set into the test basin and trimmed to the required floating position. For the analysis of the test results the position of the

center of gravity and the moment of inertia are required which can be determined by measuring the decaying oscillation of the ship hull without water contact. The test procedure of the roll decay experiment is to incline a ship to a certain roll angle ϕ. The buoyancy forces will generate a restoring moment. When the ship is released it performs a rotation about its roll axis back to the upright position and further to the other side. The ship rolls until the restoring moment decelerates the motion to a point of maximal inclination, after that the ship rolls back in upright direction. This periodic roll oscillation repeats itself until the motion energy of the ship is lost due to damping effects or keeps on rolling if its driven by external forces such as waves.

The time series of the roll angle $\phi(t)$ is recorded with an optical or inertial reference system. A plot of a roll decay time series (Fig. 2.3) shows the main properties of a damped roll motion. The ship performs the harmonic roll oscillation with a certain roll period T_{roll} starting from rest with an initial roll angle ϕ_0 or with an initial roll velocity $\dot{\phi}_0$. A measure for roll damping can be derived from the decrement of each successive roll angle maxima.

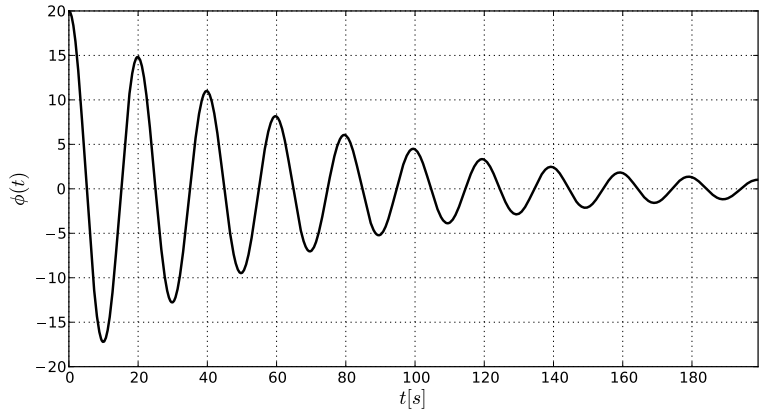

Figure 2.3.: Time series of a roll decay motion

An alternative setup for the roll decay test is a ship model with a fixed position of the roll axis. In this case, only the roll motion is free, all other degrees of freedom are fixed. This setup allows to record the roll angle with a mechanical measurement system. The setup of roll decay tests with forward velocity is more complex and can be divided into two different approaches. In the first case the model is towed and has no own propulsion. In this case the point of attack has to be in line with the (mean) roll axis of the ship. In the second case, the model ship is equipped with a motor, propeller and rudder and is self-propelled.

Aloisio [42] investigated the vortex shedding at bilge keels with PIV measurements during roll decay tests of a naval vessel. Irvine, Longo and Stern [43] presented the results from roll decay model tests of a DTMB 5415 naval vessel. This test setup was also used for benchmark tests in the Gothenburg 2010 workshop [44]. A special characteristic of the test setup was that only the roll motion of the ship was free and all other degrees of freedom were fixed. This test setup is particularly suited for comparisons with numerical methods.

2.3.2. Forced External Moments

Model tests with forced external moments differ from roll decay tests in that they use a harmonic oscillating moment instead of an initial roll angle. The excitation moment M_{err} is generated by ex-centric weights, which rotate about a fixed vertical axis with the angular velocity ω_0. This method is described by Blume [35] in more detail.

Spouge [12] uses the same method whose advantage is that the constant excitation allows repeated measurements at the same roll amplitudes. The energy fed into the system by the external moment is dissipated by the loss of energy through roll damping. The system reaches a harmonic motion equilibrium with constant roll period and amplitude.

Blume [35] defines the roll damping coefficient (Eq. (2.8), the notation N_{eff} for the damping coefficient is used) as the quotient of static roll amplitude ϕ_{stat} and the resulting roll amplitude ϕ_{res} . The natural angular roll velocity is denoted ω_0, the fluid density ρ, the gravitational constant g, the displacement ∇ and the mean metacentric height $\overline{GM}_t$.

$$N_{\text{eff}} = \frac{\rho g \nabla \overline{GM}_t}{\omega_0} \frac{\phi_{\text{stat}}}{\phi_{\text{res}}} \tag{2.8}$$

The static amplitude ϕ_{stat} is the roll angle amplitude the ship would have, when no neither a damping moment nor any other external moment would act on the ship. If the ex-centric weight rotates with angular velocity ω a harmonic roll motion with the amplitude ϕ_{res} is generated. The damping of the ship, causes a shift of the *dry* natural roll frequency ω_0 towards the excitation frequency ω. These tests are conducted for different excitation frequencies. By using the effect that the magnitude of the damping is at its lowest when the ship oscillates at its natural frequency the test can be used to determine the natural roll period of the model ship.

Blume [35] used both test methods (roll decay and forced moments) to investigate three ships with different shapes. The roll decay methods proved to be less suitable for test with high ship velocity. Because of the strong damping not enough roll maxima could be used for the damping analysis before the roll motion

had decayed. The results of the investigation of the different shape coefficients (Salvesen et al. [25]) showed that large section moment coefficients generate the largest roll damping coefficients. For small roll angles and a low ship velocity the difference in roll damping behavior between the three ships were only small.

2.3.3. Forced Motion

Apart from tests with 2D cross sections and simple hull shapes (as described in section 2.3) the method of a forced roll motion is not commonly used. In contrast to numerical computation where this type of test setup can be easily simulated, the experimental setup for a forced motion of a ship is more difficult than the roll decay method.

2.4. Roll Damping Analysis

William Froude was a pioneer in the field of roll damping research. In 1862 [9] he published the results of his roll damping experiments. The first use of a bilge keel with the purpose of increasing the roll damping was also found in Froude's publication. He conducted roll damping experiments of bilge keels by attaching a plate to a pendulum and measuring the roll period.

In physical terms roll damping stands for the loss of rotational energy of a ship. In general the amount of roll damping is specified with the roll damping coefficient B_{44}. The index 44 results from the position of the coefficient in the fourth row and forth column of damping matrix $\mathbf{B}$ in Eq. 2.1. Higher order damping models use more than one coefficient to approximate the damping behavior. They either model the roll damping with a polynomial approach or as an analytically derived sum of damping coefficients depending on different flow effects (Eq. 2.9).

The roll motion is – compared with other types of ship motion – nonlinear and only weakly dampened. Furthermore, the small numerical value of the roll damping coefficient implies that it is more complex to determine and suffers a high stochastic fluctuation. For the assessment of ship safety, an accurate prediction of roll motions is crucial. The roll damping behavior of a ship depends on many parameter such as hull shape and loading condition.

The methods for the prediction of roll damping can be categorized by the different approaches and assumptions used for their development. Model or full scale tests and numerical simulations can be used to develop new prediction methods or to determine the damping coefficients of an individual ship hull. The experiments and numerical simulations may differ in the amount of test series and model assumptions. The *fitting* of the model equations to the test results is achieved by the analysis of the measured roll angle time series, an analysis of the motion energy or

by a direct regression analysis of the test results and the model equation. The complexity of the damping model varies from single scalar damping coefficients, higher order damping equations to more complex models that use statistical methods to derive the model equations.

2.4.1. Ikeda's Roll Damping Components

The articles published by Ikeda and Himeno [45] in the years between 1977 and 1981 form the basis for the development of mathematical roll damping model. They provide the theoretical background for the roll motion of ships and introduce equations that model the roll damping. They validated their roll damping models with results from extensive model tests.

Ikeda worked on the assumption that roll damping is composed of several independent effects. Each of the damping components in his method refers to a certain flow effect. The total linear roll damping coefficient Eq. (2.9) is the sum of these components. The prediction methods for each of the damping components were published by Ikeda, Himeno, Komatsu, Tanaka and Fujiwara [41], [46], [47], [48], [49] and [50].

$$B = \underbrace{B_{\mathrm{F}}}_{\text{friction}} + \underbrace{B_{\mathrm{E}}}_{\text{eddy}} + \underbrace{B_{\mathrm{L}}}_{\text{lift}} + \underbrace{B_{\mathrm{W}}}_{\text{wave}} + \underbrace{B_{\mathrm{BK}}}_{\text{bilge keel}} \tag{2.9}$$

A detailed description of the mathematical modeling of the different components is listed in appendix A.1.

In 1965 Kato [51] used Blasius's plate friction theory for laminar flows to derive an equation for the steady friction roll damping. Today his equation is known as the Kato-formula. Tamiya [52] extended this equation in 1972 to include instationary boundary layer flow. Early roll damping prediction methods regard the ship hull as a summation of 2D flow problems (similar to the strip method). This approach was restricted to zero ship velocity cases. However, through the use of the Kato-formula, it was possible to predict the roll damping of ships with forward speed.

At the end of the 1960s Tanake published a series of articles ([37], [38], [39] and [40]) in which he describes his roll damping measurements on a rolling ellipsoid with forward velocity. He introduced the partitioning of the damping coefficient into two components, one for the normal force on the hull and one for the normal force on the bilge keel.

2.4.2. Modified Ikeda Method

The determination of the roll damping based on the the above described component method depends on shape coefficients computed with a strip method. Therefore

the geometric description of the ship has to be available in order to compute the damping coefficient. In 2008 Ikeda [53] published a simplified version of his prediction method that allows the determination of the damping coefficient in an early design stage. This *simple* Ikeda method can be obtained as Fortran source code (Ikeda [54]). In appendix A.4 an example application of the simple Ikeda method is shown. Instead of using a strip method the shape coefficients are estimated with polynomial approximations depending on the main ship dimensions. The drawback of this simplified approach is that the roll damping prediction is limited to hull parameter within a moderate range.

2.4.3. Equivalent Roll Damping Coefficients

The long history of roll damping analysis has yielded a number of different definitions for roll damping. The following paragraph gives an overview of the most commonly used formulations for roll damping. Furthermore, to capture the nonlinear behavior of roll damping, higher order equations are used. In order to compare these models to linear damping coefficients, a equivalent damping coefficient can be computed.

Equation (2.10) states the one-dimensional ordinary differential equation for roll motion. $\phi(t)$ denotes the roll angle, ϕ_A maximal roll angle amplitude , angular velocity $\dot{\phi}(t)$ and angular roll acceleration $\ddot{\phi}(t)$. In addition the equation depends on the nonlinear damping function $B_\phi(\dot{\phi})$, the linear inertial coefficient A_ϕ, the linear restoring coefficient C_ϕ and the time dependent external roll moment $M_\phi(t)$.

$$A_\phi\ddot{\phi} + B_\phi(\dot{\phi}) + C_\phi\phi = M_\phi(t) \tag{2.10}$$

Higher order nonlinear damping function:

$$B_\phi = B_1\dot{\phi} + B_2\dot{\phi}|\dot{\phi}| + B_3\dot{\phi}^3 + \dots \tag{2.11}$$

Transformation to mathematical standard notation:

$$\ddot{\phi} + 2\alpha\dot{\phi} + \beta\dot{\phi}|\dot{\phi}| + \gamma\dot{\phi}^3 + \omega_n^2\phi = M_\phi(t) \tag{2.12}$$

with the natural angular velocity ω_n and the following substitutions:

$$2\alpha = \frac{B_1}{A_\phi}, \quad \beta = \frac{B_2}{A_\phi}, \quad \gamma = \frac{B_3}{A_\phi},$$
$$\omega_n = \sqrt{\frac{C_\phi}{A_\phi}}, \quad m_\phi = \frac{M_\phi}{A_\phi}$$

For model ships the influence of the surface tension of the water may be incorporated with the additional term $\dot{\phi}/|\dot{\phi}|$. However for typical sized model ships this

term is not significant. In [45] Himeno proposes a test setup with a forced harmonic roll motion $\phi_A \sin(\omega t)$ and the measurement of the reaction moment. The model coefficients could be determined by fitting the solution of the differential equation to the time series of the reaction moment. The nonlinear damping equation $B_\phi(\dot{\phi})$ can be approximated by the equivalent linear coefficient B_e [45].

$$B_e = B_1 + \frac{8}{3\pi}\omega\phi_A B_2 + \frac{3}{4}\omega^2\phi_A^2 B_3 \tag{2.13}$$

It is common to transform the damping coefficients to dimensionless numbers (indicated by a $\widehat{}$ symbol over) by multiplying the terms with functions of the ship breadth B_{ship}, the displacement ∇ and the gravitational constant g. The index i denotes the polynomial order of the coefficients (B_1, B_2, and so on).

$$\widehat{B}_e = \frac{B_e}{\rho\nabla B^2}\sqrt{\frac{B}{2g}}, \quad \widehat{B}_i = \frac{B_i}{\rho\nabla B_{\text{ship}}^2}\left(\sqrt{\frac{B_{\text{ship}}}{2g}}\right)^{2-i}, \quad \widehat{B}_{44} = \frac{B_{44}}{\rho\nabla B_{\text{ship}}^2}\sqrt{\frac{B_{\text{ship}}}{2g}} \tag{2.14}$$

This transformation also holds for the equivalent linear coefficient, higher order coefficients and the total damping coefficient. The angular velocity ω may be transformed with a similar method to another characteristic number $\widehat{\omega}$ and is related to the Froude number (Ikeda [53] and Jaouen [28]).

$$\widehat{\omega} = \omega^* = \omega\sqrt{\frac{B_{\text{ship}}}{2g}} \tag{2.15}$$

Furthermore, Ikeda shows in [53] with equation 2.16 a connection to Bertins [55] N-coefficients, which are also damping coefficients that can be transformed to $\widehat{B}_{44}$ with:

$$N = \widehat{B}_{44}\frac{\pi B_{\text{ship}}\widehat{\omega}}{\text{GM}\phi_A} \tag{2.16}$$

For roll decay tests equation (2.12) is often used in the form of Eq. (2.17) with the initial condition $\phi(t=0) = \phi_A$.

$$\ddot{\phi} + 2\delta\dot{\phi} + \omega_0^2\phi = 0 \tag{2.17}$$

In equation (2.17) the roll damping is modeled with the natural linear coefficient δ ($\widehat{=}\alpha$ in Eq. (2.12)) and the natural angular velocity ω_0 ($\widehat{=}\omega_n$ in Eq. (2.12)). Equation (2.18) is an analytical solution of Eq. (2.17) under the assumption that the damping is sufficiently small and that the initial velocity is zero $\dot{\phi}(t=0) = 0$.

$$\phi(t) = \phi_A e^{-\delta t}\cos\omega_0 t \tag{2.18}$$

The exponential function with the exponent δ is a term that models the energy loss due to roll damping. The damping coefficient $\delta[s^{-1}]$ can also be made dimensionless by multiplying the coefficient with the natural angular velocity Eq. (2.19).

$$\delta = \delta_0 \omega_0 \tag{2.19}$$

By transforming the exponential term of the solution of the motion equation (Eq. (2.18)) equation (2.20) can be used to compute the damping coefficient δ depending on the roll period T_{roll} and two consecutive roll angle maxima ϕ_i and ϕ_{i+1} (Molland [56]).

$$\delta = \frac{1}{T_{\text{roll}}} \log_2 \left(\frac{\phi_i}{\phi_{i+1}} \right) \tag{2.20}$$

2.4.4. Regression Methods

In general, regression methods can be used to derive a roll damping prediction method without prior knowledge of the governing equations. For example an artificial neural network simply needs a database, containing the input variables and the results of the unknown system, to compute a roll damping prediction method for this system (Meshbahi et al. [57], Xing and McCue [58] and Han [59]). A drawback of these methods is that they don't provide an insight on the intrinsic properties and physical behavior of roll damping.

Another approach is to use existing *Ansatz* equations for the damping coefficients and derive a roll damping method by fitting the the model to experimental or simulated results. These fitting methods belong to the field of regression analysis as well. For this purpose usually the least squares (LS) method (Bronstein [60]) is applied.

The analysis of roll decay and forced motion tests require an analytic solution of the motion equation. For motion equations with only a linear damping coefficient exist simple analytical solutions (see appendix A.2). For higher order damping terms more complex solution methods need to be applied (Laplace and Fourier transformation or perturbation methods [12]). To reduce the number of unknown coefficients often a strip or panel method is used to compute the added mass and restoring forces prior to the regression analysis.

Spouge [12] describes two mathematical models that can be used in the regression analysis of roll motion time series. The first linear method uses the phase shift of the time dependent roll angle to the excitation moment. The second method uses the kinetic energy $\mathcal{V}(t)$ (Eq. (2.21)), composed of the sum of the rotation energy and the potential energy stored in the inclined ship hull. The area moment of inertia is denoted I_{44} and the function $C(\phi)$ is the polynomial expansion of the

restoring moment (see Eq. (3.30)).

$$\mathcal{V}(t) = \tfrac{1}{2} I_{44} \dot{\phi}^2 + \int_0^{\phi} C(\phi) d\phi \tag{2.21}$$

The two *energy* methods presented by [12] are based on Froude ([9]) and Roberts ([15]) and both use the integral of the restoring moment to compute the energy loss during the roll motion. However they differ in their analysis procedure: The method based on Froude uses the slope (derivation) of the restoring moment while the method based on Roberts' approach analyzes the results of the time series integration directly. Using the direct value instead of the derivation makes the analysis procedure more stable. Another difference of the two methods is the different interval length they use for the integration.

The resulting coefficients of both methods deviate up to 10% from each other, although if compared in a graph the difference is negligible. A problem often encountered during the analysis of roll decay tests is the large decrease of the roll amplitude. This effect can originate from the non-developed flow field at the beginning of the roll motion and the strong roll damping occurring at full forward velocity.

Most of the regression methods show similar results: for small roll angle amplitudes the resulting coefficient are close to each other, while for large roll angles the coefficients tend to diverge. Another different in the damping results is the weighting of linear and quadratic coefficients. For the Froude energy method the linear coefficients tend to be higher than the linear coefficient. Of both methods the energy method based on Roberts produces the best fit, although is more sensitive to errors of height and position of the roll angle maxima. This sensitivity can be compensated by the use of a cubic spline smoothing of the time series data.

Bass and Haddara [11] use a similar method for their regression analysis only that they compute the integrals over the complete time series. Their approach has the advantage that all data points are used for the analysis instead of only using the roll angle maxima. This allows an evening out of the disturbances in the roll angle signal and to analyze short time series.

$$\ddot{\phi} = 2\omega_\phi \delta \left(\dot{\phi} + E_1 |\phi| \dot{\phi} + E_2 \phi^2 \dot{\phi} + E_3 |\dot{\phi}| \dot{\phi} + E_4 \dot{\phi}^3 \right) + \omega_\phi^2 \left(\phi + \mu \phi^3 \right) = F(t) \tag{2.22}$$

In [11] the authors apply an extended damping model Eq. (2.22) with the less common damping coefficients E_1 and E_2 and a function for the restoring moment with a relative low order. The best approximation of the measured time series was achieved with Eq. (2.23).

$$B(\phi, \dot{\phi}) = \dot{\phi} + |\phi| \dot{\phi} + |\dot{\phi}| \dot{\phi} \tag{2.23}$$

In general the model with a linear and quadratic term ($B_1\dot{\phi} + B_2|\dot{\phi}|\dot{\phi}$) is the most commonly used damping model. The linear plus cubic model ($B_1\dot{\phi} + B_3\dot{\phi}^3$) on the other hand allows a simpler mathematical transformation and its approximation to the experiments is sufficient enough (Dalzell [61]).

3. Mathematical Model

The main objective of this thesis is to find an equation that models the functional connection between the hull shape and its roll damping behavior. The term *mathematical* is used to point out, that the final prediction model will not be a *black box* with an unknown internal algorithm, but will be an algebraic equation that connects basic shape parameter to find a *natural law* that relates the hull shape with the roll damping coefficient. That means, that in comparison to a typical regression method like Artificial Neural Networks (ANN), the knowledge of the actual model equation will provide an additional insight into the principles of roll damping. The direct work with the mathematical terms allows to find the best compromise between prediction quality and robustness of the method.

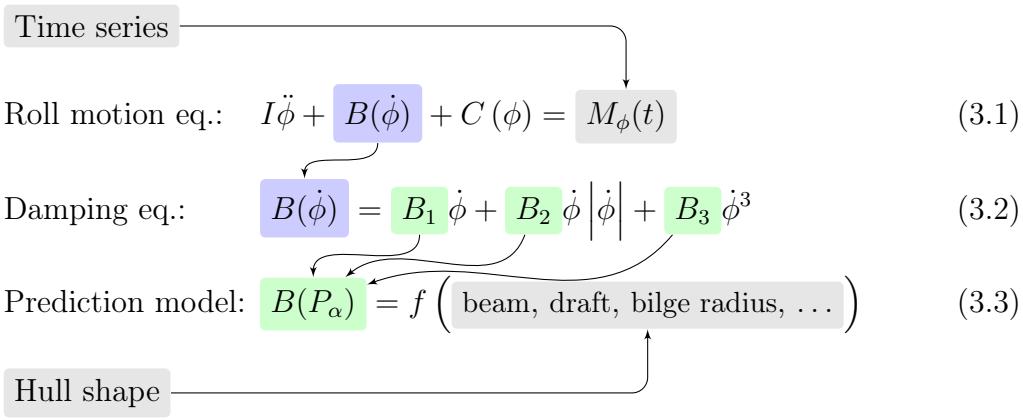

Equation (3.1)-(3.3) list the three main equations in this thesis: the differential equation that models the roll motion of a ship (3.1), an equation for the nonlinear roll damping term (3.2) and the jet unknown roll damping prediction formula (3.3). The arrows indicate how the equations are connected and how they are related to the hull shape and time series data.

The roll motion equation (3.1) models the dynamic roll behavior of a ship. Inertia, damping and restoring moment are unknown coefficients or functions and the external moment $M_\phi(t)$ is given in form of time series results from model tests (Sec. 4.2.5) or CFD simulation (Chap. 4). Equation (3.2) states a commonly used Ansatz function (see Eq. (3.13)) that models the nonlinear roll damping with a polynomial expansion of the roll angle velocity $\dot{\phi}$. The damping coefficients B_1, B_2, B_3 are obtained by time series analysis (Sec. 3.2). The third equation

denotes the roll damping prediction equation $B(P_\alpha)$ that will be derived by correlating (Sect. 5.3) the damping coefficients to P_α, which is the vector or set that contains the hull shape parameter.

The method used to determine this *correlation* is termed *regression analysis* (see Sec. 5.3) and can be divided into two phases: First, in the *training* phase, the input data is analysed and the results are used to *configure* the model equation. Then, in the *application* phase, the configured model is used to predict the roll damping for a new hull design.

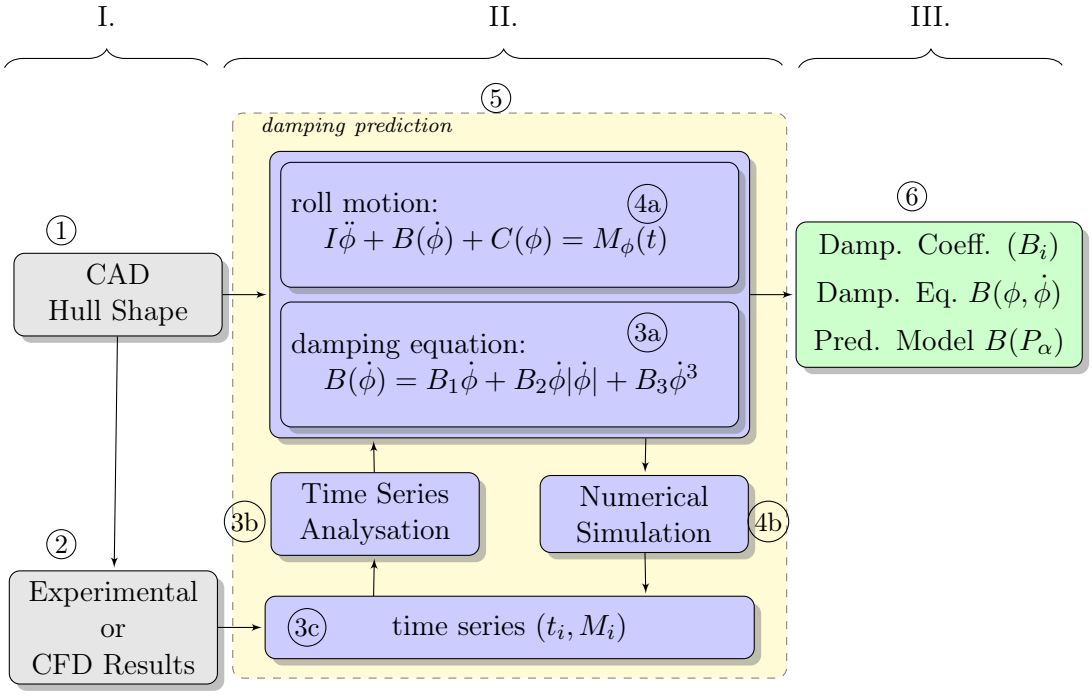

Figure 3.1.: Structure of the development process for the roll damping prediction model

Figure 3.1 shows the principle structure of the development process for the prediction model. The diagram is horizontally divided into three parts: I. the generation of the training data, indicated by the gray blocks on the left, II. the training process, shown by the light yellow block in the center and III. the outcome of the development process in the light green block on the right.

The general approach of the development concept is summarized in the following steps:

I. The training data that is generated by:

(1) Variation of shape properties of a ship hull that are expected to have a large influence on the roll damping behavior. One set of shape parameter are gathered in a parameter vector: $P_\alpha = [\text{beam, draft, bilge radius, ...}]$ and all parameter combinations are stored in N sets $P_{\alpha,i}$ with $i = 1 \dots N$.

(2) For each hull shape variation P_α, a viscous CFD simulation of a rolling ship is conducted, that results in a roll moment time series: $M_\phi(t) \rightarrow (t_i,\, M_i)$

IIa. The actual training process is split into two consecutive steps: First, the determination of a damping equation 3.2, that results in the best *fit* to the roll motion time series:

(3) The derivation of $B(\phi, \dot{\phi})$ is done iteratively by selecting an Ansatz function (point 3a in Fig. 3.1) for the damping equation (3.2) and applying time series analysis (point 3b) to the roll moment times series (point 3c) in order to obtain the damping coefficients B_1, B_2, B_3.

(4) Next, the quality of the model fit is determined by numerically solving the differential roll motion (Eq. (3.1), point 4a) and comparing the resulting time series (point 4b) to the CFD results (point 3c).

By repeating this process for all variations of P_α, a database with all hull shape variations and the according damping coefficients is generated.

IIb. The second, consecutive training step is the derivation of the actual roll damping prediction model:

(5) With nonlinear regression methods, the damping coefficients are correlated to the hull parameter, which results in a mathematical equation for the roll damping $B_i \propto P_{\alpha,i} \rightarrow B(P_\alpha)$

This process also consists of an iterative procedure that selects and evaluates different Ansatz functions for the prediction equation (3.3).

III. The outcome of this procedure is:

(6) the selection of the *best* fitting damping model $B(\phi,\, \dot{\phi})$,

(6) a database with hull shape variations and the their according damping coefficients $[P_\alpha,\, B_i]$ and

(6) the roll damping prediction model $B(P_\alpha)$.

In order to apply a consistent methodology for the derivation of the prediction model, the process shown in Fig. 3.1 is implemented into a computational framework that manages the data structures and computation procedures.

The selection of the hull shape parameter and their variation range is described in section 5.1. The evaluation of the time series analysis results can be done by solving the roll motion equation analytically – if the equation is simple enough – or by numerical simulation (both methods are presented in Sec. 3.1)

The computation procedure for the roll damping coefficients depends on whether the input data was obtained by roll decay or forced motion tests. The time series analysis methods for both of these cases are described in Sec. 3.3.

The fact that the basic roll motion model is a nonlinear differential equation and that, in addition the damping term, the inertia and restoring moments are also dominated by the complex flow conditions around the ship hull, present a particular challenge. In order to allow for a better distinction between the influence of each term in equation (3.1) and to reduce the amount of uncertainty in the prediction process, the value of the inertia and restoring moments are also determined. The hydrostatic restoring moment $C(\phi)$ can be computed with the procedure described in section 3.4 and the *added mass* component of the inertia I can be predicted with the method presented in section 3.5.

3.1. Analytical and Numerical Solution of the Roll Motion Equation

In a first approach it is sufficient to model the free roll motion of a ship with a linear homogeneous differential equation (Eq. (2.2)).

$$\underbrace{I\ddot{\phi}}_{\text{inertia}} + \underbrace{B\dot{\phi}}_{\text{damping}} + \underbrace{\Delta\overline{\text{GM}}\phi}_{\text{restoring}} = 0 \tag{3.4}$$

The roll motion depends on three angular moment terms: the inertia moment, depending on the inertia coefficient I and the angular acceleration $\ddot{\phi}$; the damping moment depending on the damping coefficient B and the angular velocity $\dot{\phi}$; the density ρ, the gravitation g, the displacement ∇ and the restoring moment $\rho g \nabla \overline{\text{GM}}\phi = \Delta\overline{\text{GM}}\phi$ depending on the roll angle ϕ. For free roll decay, the right side of the equation is zero. If the roll motion is driven by an external roll moment $M_\phi(t)$ on the right side of Eq. (3.1) the equation becomes an inhomogeneous differential equation.

For this *simple* homogeneous linear differential equation a solution can be derived analytically. First, the one dimensional differential equation is reformulated into Eq. (3.5a), with $2\delta\omega_0 = B/I$ and $\omega_0^2 = \Delta\overline{\text{GM}}/I$. Further, the initial condi-

tions for the roll angle (3.5b) and the roll velocity (3.5c) are defined.

$$\ddot{\phi} + 2\delta\omega_0\dot{\phi} + \omega_0^2\phi = 0 \tag{3.5a}$$
$$\phi(0) = \phi_0 \tag{3.5b}$$
$$\dot{\phi}(0) = \dot{\phi}_0 \tag{3.5c}$$

The parameter ω_0 denotes the natural angular frequency and δ the natural damping coefficient (the coefficient is equivalent to B, just the physical unit is changed).

The analytical solution of a simple roll motion equation can be derived with the method of Laplace-transformations (The complete derivation procedure of this solution method is listed in appendix A.2). Applying this method to Eq. (3.1) results in the analytic solution (3.6). Here, the initial velocity is assumed to be zero ($\dot{\phi}(0) = 0$) and the substitution $D = \sqrt{1-\delta^2}$ is used.

$$\phi(t) = e^{-\delta\omega_0 t}\left(\phi_0 \cos(\omega_0 D t) + \left(\frac{\dot{\phi}_0}{\omega_0 D} + \frac{\delta\phi_0}{D}\right)\sin(\omega_0 D t)\right) \tag{3.6}$$

If the roll motion is forced by a simple harmonic function $M_\phi(t) = M_0 \sin(\omega t)$, the differential equation is still analytically solvable. But for an arbitrary excitation moment or a nonlinear damping model a generally applicable method to obtain an analytic solution is not available.

In order to determine the roll motion for an arbitrary differential equation – with nonlinear damping and restoring terms – the solution often has to be computed numerically. Equation (3.7) shows a typical roll motion equation with high order damping ($B(\dot{\phi})$) and restoring ($C(\phi)$) terms and an unknown external roll moment $M_\phi(t)$.

$$A_\phi\ddot{\phi} + \underbrace{B_1\dot{\phi} + B_2|\dot{\phi}|\dot{\phi} + B_3\dot{\phi}^3}_{B(\dot{\phi})} + \underbrace{C_1\phi + C_3\phi^3 + C_5\phi^5}_{C(\phi)} = M_\phi(t) \tag{3.7}$$

The theory and the numerical algorithm for the solution of such an nonlinear second order differential equation is described in appendix A.3. The nonlinearity is treated with the *Newton method* and the time derivative is approximated with a *Crank-Nicolson time integration* scheme. The numerical algorithm described in appendix A.3 is an essential part of the development process of the mathematical damping model. In order to improve the damping model, the simulated roll motion is compared with the time series obtained with experimental or numerical methods, which allows to measure the quality of the damping model.

Figure 3.2 shows the roll decay time series of a linear motion equation computed both with the analytical solution and the python script. The perfect match shows the correct derivation of the analytical solution (A.2) and the implementation of the Newton method (A.3).

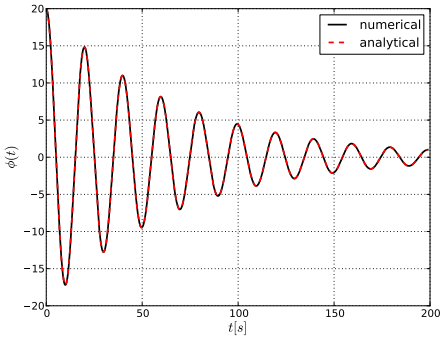

Figure 3.2.: Numerical and analytical solution of roll ODE with initial condition

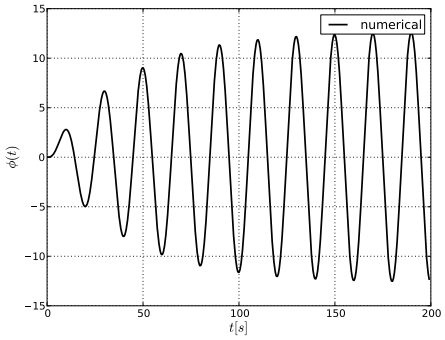

Figure 3.3.: Numerical solution of roll ODE with forced moment excitation

The time series show in figure 3.3 was simulated by starting the motion from rest and driving the roll motion by an external oscillating moment. While the motion energy in the time series in Fig. 3.2 continuously decreases, the roll amplitude (and thereby the motion energy) of the time series in Fig. 3.3 grows until the energy, fed into the system by the external moment, is equal to the energy lost by roll damping. The system is then in an equilibrium state.

3.2. Time Series Analysis

The objective of the time series analysis is to determine the underlying mathematical model and parameter of a time series. The following section describes the methods and analysis procedures used to process a time series and extract the required information.

The time series of the roll motion of a ship – obtained either by experiments or numerical simulation – is defined by a list of $i \in 0 \dots n$ discrete roll angle values ϕ_i and the corresponding time stamp t_i (Eq. (3.8)).

$$\phi(t_i) \widehat{=} [(t_0, \phi_0),\ (t_1, \phi_1),\ \dots,\ (t_n, \phi_n)] \tag{3.8}$$

The properties of a time series are explained with the example time series shown in Fig. 3.4. In context with roll damping, the time series is always a harmonic function, with an almost constant roll period. In case of roll decay tests the roll period can shift slightly, due nonlinear effects at large roll angles. Time series resulting from CFD simulation may have a varying time step size, while data from experiments may suffer from noise.

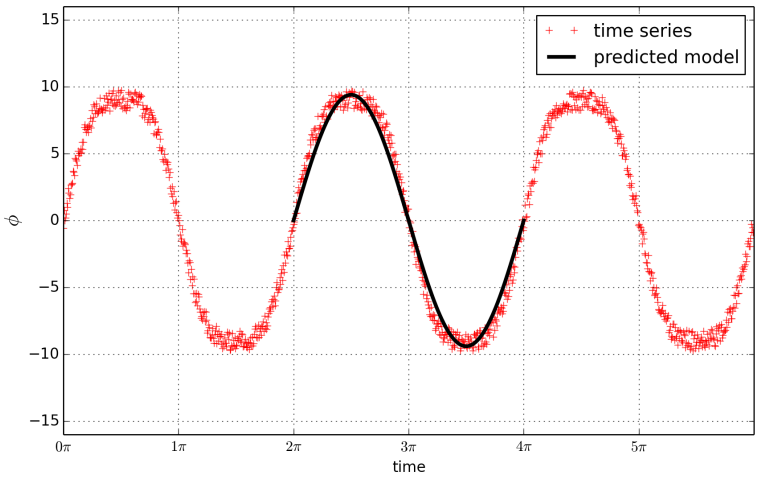

Figure 3.4.: Noisy time series with fitted linear model

This artificial time series (red + symbols) is a harmonic function superimposed with noise. To make the analysis process more realistic, the time step size Δt is not constant. The black line in Fig. 3.4 shows the resulting function computed with one of the following methods.

The first step in the analysis procedure is to *guess* an Ansatz equation that best fits the input data. Equation (3.9) defines a function g that depends on the time t and the unknown coefficients $\boldsymbol{\beta} = [\beta_1, \beta_2, \beta_3]$ with amplitude β_1, angular frequency β_2 and phase shift β_3.

$$g(t_i, \boldsymbol{\beta}) = \beta_1 \cos(\beta_2 t_i + \beta_3) \tag{3.9}$$

The determination $\boldsymbol{\beta}$ can be conducted with two different methods. One way is to determine each parameter separately by the use of discrete Fourier transformation (DFT), spectral analysis and calculation of zero crossings and is described in the next paragraph. The second method is called *least squares* (LS) fitting and is described in the paragraph following the next.

3.2.1. Fourier Transformation

Fast Fourier Transformation (FFT, [60], [62]) is used to compute the frequency spectrum of the time series. By selecting the frequency f with the highest amplitude the angular frequency $\beta_2 = 2\pi f$ and period $T = 1/f$ is determined. If the the time step size of the signal is not constant, the sample rate of the time series has to be unified. This is achieved by defining a fixed Δt and compute new data points with linear interpolation.

The parameter β_3 denotes the time shift of the harmonic function with respect to time $t = 0$. This parameter is required for DFT computations in the next step. The time shift β_3 is determined by finding the zero crossings of the time series. These time points are found by computing the numerical derivation with a central difference scheme and selecting the local maxima and minima of the resulting time series. In case of a noisy time series, it may be necessary to smooth the data prior to certain mathematical operations, in order to prevent multiple zero crossings next to each other. The smoothing can be done with the Bezier-spline interpolation method available in [63].

Once the zero crossings are determined, the begin and end of a motion cycle is defined by two time points t_a and t_b of consecutive positive or negative signal slopes. The time shift β_3 is the time span between start time of the series t_0 and the begin of the cycle t_a. The time points of the zero crossings can also be used to compute the time period.

$$a_k = \frac{\omega_k \Delta t}{\pi} \sum \phi_i \sin(\omega_k t_i) \tag{3.10}$$

$$b_k = \frac{\omega_k \Delta t}{\pi} \sum \phi_i \cos(\omega_k t_i) \tag{3.11}$$

Finally, the DFT analysis allows to determine linear harmonic components of the time series. Equations (3.10) and (3.11) list the discrete version of Fourier transformation integrals. Inside the summation symbols the roll angle values get multiplied with sine and cosine functions of the same angular frequency $\omega_k = \beta_2$ as determined earlier. Equations (3.10) and (3.11) represent the discrete formulation of a convolution integral that results in the coefficients a_k and b_k, which define the amplitudes of the sine and cosine components of the time series. The last unknown parameter β_1 can be determined by simple evaluation of Eq. (3.11).

3.2.2. Least Squares

The LS method ([60], [64]) numerically minimizes the error function (3.12), resulting in a set of optimal $\boldsymbol{\beta}$-parameter that fit the time series with the smallest deviation. Here, ϕ_i is one of the n discrete roll angle values and $f(t_i, \boldsymbol{\beta})$ is the model function.

$$\min_{\boldsymbol{\beta}} \sum_{i=0}^{n} \left[\phi_i - f(t_i, \boldsymbol{\beta})\right]^2 \tag{3.12}$$

While DFT analysis only allows to determine linear harmonic components of a time series, the LS method allows to determine the coefficients of nearly arbitrary

model equations. Equation (3.12) denotes a so called *minimum problem*. Subtracting the Ansatz equation (3.9) from the data points generates a error function, which is then minimized with [63].

The principle approach for a least squares fit is to use a series expansion of the damping and restoring terms in the motion equation (3.1)

$$B(\dot{\phi}) = B_1\dot{\phi} + B_2|\dot{\phi}|\dot{\phi} + B_3\dot{\phi}^3 \tag{3.13}$$

$$C(\phi) = C_1\phi + C_3\phi^3 + C_5\phi^5 \tag{3.14}$$

The high order terms in equation (3.7) are derived from a power series expansion of the roll velocity $\dot{\phi}$ (3.13) and the roll angle ϕ (3.14).

The parameter B_1, B_2 and B_3 denote the linear, quadratic and cubic damping coefficient and C_1, C_3 and C_5 the linear, cubic and quintic restoring coefficient. The second order damping term contains the absolute value of the roll velocity. This operation is used to ensure a change of sign at the zero crossing of the function. For the same reason the restoring moment used only coefficients with odd orders.

To analyze roll motion data, equation (3.7) has to be transformed into different formulations, according to the test or simulation method. For roll decay tests the right hand side of the equation is set to zero. A forced moment boundary condition is defined by adding the excitation moment $M_{\mathrm{err}}(t)$. The forced motion test on the other hand, is modeled by replacing the free variable ϕ and its derivatives $\dot{\phi}$ and $\ddot{\phi}$ by harmonic functions. This reduces the differential equation an algebraic function which can be directly used for the LS procedure.

At large roll angles ($> 10°$) the restoring moment is not longer a linear function with the constant $\overline{GM}$, but has to use the lever arm function $GZ(\phi) = C(\phi)$. The use of a series expansion of $C(\phi)$ with higher order polynomials allows to compute the restoring moment for large roll angle.

The quality of the computed coefficients can be determined by the accuracy of the results and the robustness of the regression method. The accuracy of damping model and regression method can be assessed by defining specific damping coefficients, conducting a numerical simulation with the motion equation (3.1) and then applying the regression method to the resulting time series. The accuracy of the regressions methods depends on how small the difference between resulting coefficients and initial coefficients is. The robustness of the regression method can be investigated by reducing the data points or adding a random signal to the time series. The quality of the damping model itself cannot be tested with this approach since both regression method and differential equation use the same model equation.

3.3. Roll Damping Coefficients

The roll damping cannot be measured directly, but has to be determined through time series analysis methods. In the following sections two of the most common procedures are described. Both procedures apply the time series analysis methods described in the previous section (Sec. 3.2). The procedure of determine the roll damping coefficient depends on the test method and the measured unit.

The following two sections describe the analysis method for a roll decay test where the roll angle ϕ was measured and a forced motion test where moment M_ϕ was measured.

3.3.1. Roll Decay

The time series data used in this section originate from model tests conducted by the HSVA [65]. The roll decay analysis was published in Piehl and el Moctar [5] (together with a comparison of experimental and numerical tests, described in section 4.2.5).

A necessary model assumption required for the analysis of roll decay data is to neglect the influence of all degrees of freedom except the roll motion. The main characteristic properties of the motion function (2.17) is the natural damping coefficient δ_0 and the natural roll period $T_0 = \frac{2\pi}{\omega_0}$. The damping coefficient can either be noted as a dimensionless natural roll damping coefficient δ_0 or as $\delta = \delta_0\omega_0[s^{-1}]$, by multiplication with the natural angular velocity.

$$\delta_0 = \frac{1}{2\pi} \ln\left(\frac{\phi_n}{\phi_{n+1}}\right) \tag{3.15}$$

The most common way to obtain δ_0 from a roll angle time series is to measure the position and amplitude of roll angle extrema and calculate the logarithmic decrement of two successive roll amplitudes ϕ_n and ϕ_{n+1} (Eq. (3.15), [56]). The time points of the roll amplitudes can also be used to determine the roll period. For the automated calculation of the damping coefficient, the whole analysis procedure was implemented in a python program.

The extrema shown in Fig. 3.5 were computed by calculating the gradient of the signal and selecting the zero crossing. In order to prevent multiple false selections due to a noisy signal, the time series is previously smoothed. In a next step positive and negative amplitudes are processed separately in order to compensate a possible offset of the roll angle time series.

If the roll amplitudes fall under a threshold of 1° the time series is truncated, because at a roll motion near its extinction the roll period tends to drift away. At tests with forward speed, the roll motion does not completely vanish, but a small oscillation of the roll angle, driven by the forward speed, remains.

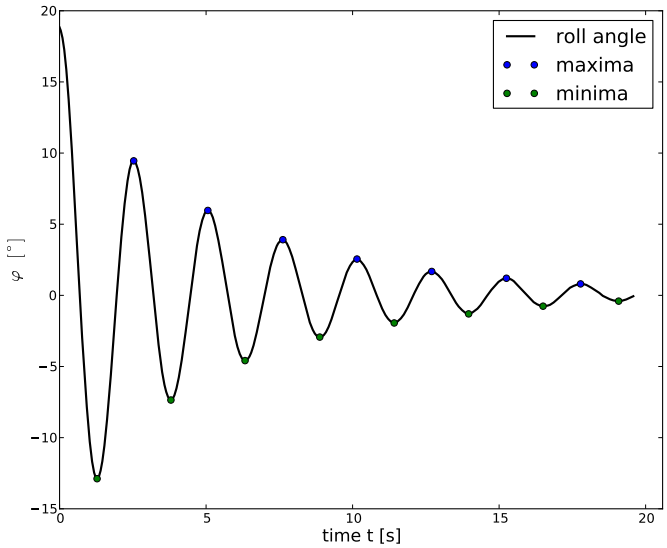

Figure 3.5.: Roll decay time series of the DTC for draft D=12m, velocity U=1.47m/s; automatic selected amplitudes

Figure 3.6 shows a plot of the damping coefficient over the mean roll amplitude. The plot indicates a nonlinear dependency on the roll angle amplitude. Instead of the constant coefficient δ_0 the roll decay function can be better approximated with a linear or quadratic damping model, also shown in the graph.

An alternative analysis method is to look at the time dependent motion energy of the rolling ship. The energy of the roll ship decays over time due to energy loss based on friction and inertial flow effects (waves, vortices). The first term in Eq. (3.16) represents the kinetic energy depending on the angular velocity, while the second term denotes the potential energy stored in the inclination of the ship against the restoring moment.

$$E_{\text{tot}} = E_{\text{kin}} + E_{\text{pot}} = \frac{1}{2} I \dot{\phi}^2 + \int_0^{\phi} \Delta \overline{\text{GM}} \phi d\phi \tag{3.16}$$

Figure 3.7 shows the change of the motion energy visualized by the phase plane trajectory of the complex motion state z, where the imaginary part $Im(z)$ is the roll angle velocity $\dot{\phi}$ and the real part $Re(z)$ is the roll angle ϕ. Starting with an initial roll angle and angular velocity the motion state moves on a spiral path towards the equilibrium point $(\phi, \dot{\phi}) = (0, 0)$. The radial distance $|z| = \sqrt{\phi^2 + \dot{\phi}^2}$ of a point on the spiral path is proportional to the motion energy of a rolling ship.

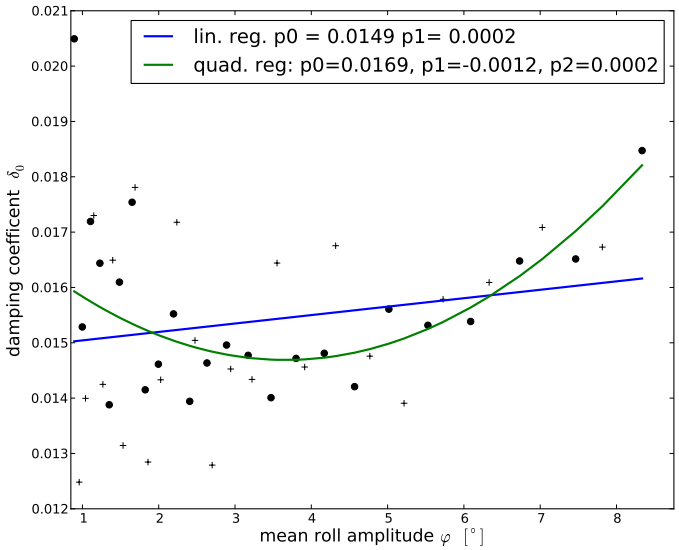

Figure 3.6.: Roll decay time series of the DTC for draft D=14m, velocity U=0m/s; damping coefficient over roll angle

By using least squares regression, an exponential test function $f(t) = \phi_0 e^{-\delta t}$ was fitted to the radial distance time series derived from the motion state Fig. 3.8. The natural roll period of a time series was determined by applying a FFT analysis on the roll angle time series and selecting the frequency with the maximal value in the amplitude spectrum.

Both methods result in nearly the same values for the roll period and the damping coefficient. For signals with only few oscillations or a very low sampling rate the method of measuring the zero-crossings to obtain the roll period is more robust than the FFT method.

The energy method, based on a complex motion state z has the advantage that it uses all data points of the time series and not only the extrema. It also allows to look at nonlinear behavior during a roll cycle. Another advantage is that this method is more robust for time series with high damping coefficients, where only very few roll cycles occur before the oscillation amplitude drops under the threshold. The ability of the first method, to calculate higher order damping coefficients could be extended to the second method.

The quality of the calculation methods for the damping coefficient was controlled visually (Fig. 3.9) by plotting the envelope function $f = \pm\phi_0 e^{-\delta t}$ over the roll angle time series, where ϕ_0 is the initial roll angle amplitude.

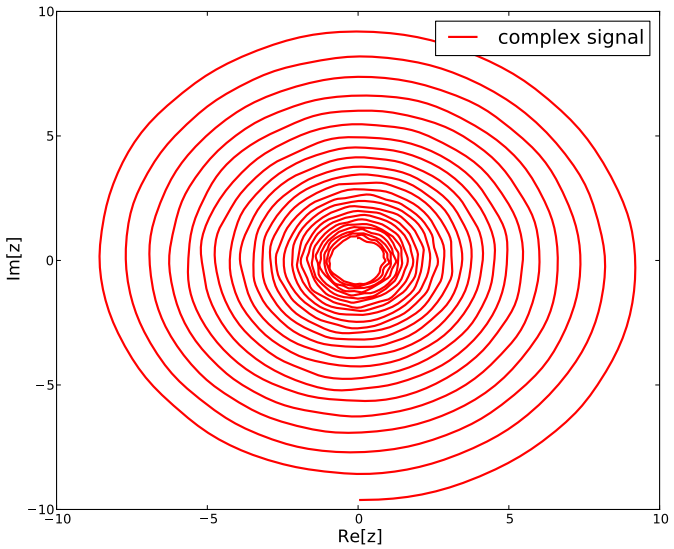

Figure 3.7.: Complex roll motion state z in phase space

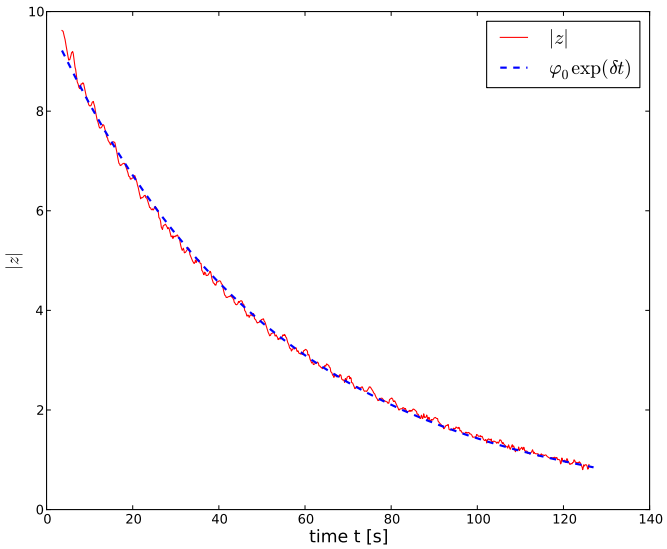

Figure 3.8.: Radial distance function of the motion state and fitted exponential curve

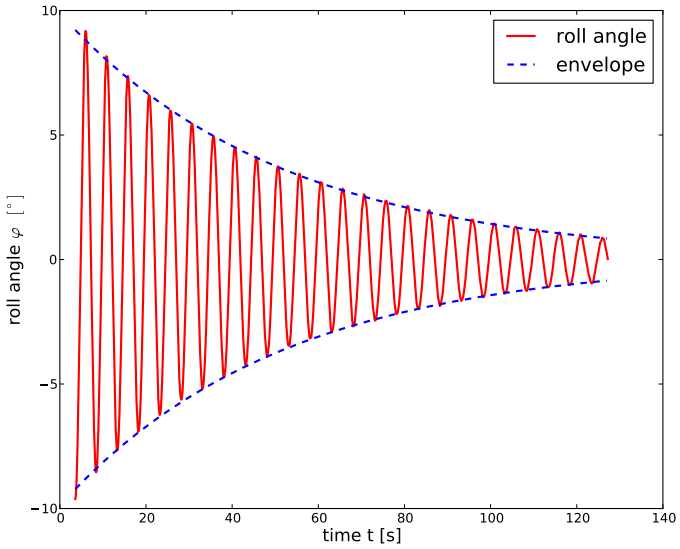

Figure 3.9.: Roll decay time series of the DTC: draft D=14m, velocity U=0m/s; oscillating roll angle and envelope over time

3.3.2. Forced Motion

In forced motion tests, the ship does not perform a free motion (as in roll decay tests), but is forced to follow a prescribed kinematic motion. Because of this restriction the equation that describes the motion the ship is transformed from the differential equation (3.17) to a linear algebraic equation.

$$I\ddot{\phi} + B\dot{\phi} + \Delta\overline{\mathrm{GM}}\phi = M_\phi(t) \tag{3.17}$$

In equation (3.17) the former free variable ϕ and its derivatives are replaced by the forced time-dependent roll angle $\phi(t)$, angular velocity $\dot{\phi}(t)$ and angular acceleration $\ddot{\phi}(t)$:

$$\phi(t) = \quad \phi_A \sin(\omega t) \tag{3.18a}$$
$$\dot{\phi}(t) = \quad \phi_A \omega \cos(\omega t) \tag{3.18b}$$
$$\ddot{\phi}(t) = -\phi_A \omega^2 \sin(\omega t) \tag{3.18c}$$

Inserted in eq. 3.17 results in

$$-I\phi_A\omega^2 \sin(\omega t) \quad + \quad B\phi_A\omega\cos(\omega t) + \Delta\overline{\mathrm{GM}}\phi_A \sin(\omega t) = \mathrm{M}_\phi(t) \tag{3.19}$$

and subtracting the known hydrostatic restoring moment $M_{\mathrm{dyn}} = M_\phi - M_{\mathrm{stat}}$ leads to:

$$-I\phi_A\omega^2 \sin(\omega t) + \mathrm{B}\phi_A\omega\cos(\omega t) = \mathrm{M}_{\mathrm{dyn}}(t) \tag{3.20}$$

The hydrostatic restoring moment can be obtained by measurement of the moment in calm water or by calculation (see Section 3.4). In both cases, the influence of the primary wave system on the restoring moment is neglected. This transformation is also applicable for higher order damping models. The damping model for linear plus cubic terms:

$$I\ddot{\phi} + B_1\dot{\phi} + B_3\dot{\phi}^3 + \Delta\overline{\mathrm{GM}}\phi = M_\phi(t) \tag{3.21}$$

leads to

$$-I\phi_A\omega^2 \sin(\omega t) + \mathrm{B}_1\phi_A\omega\cos(\omega t) + \mathrm{B}_3\phi_A^3\omega^3\cos^3(\omega t) = \mathrm{M}_{\mathrm{dyn}}(t) \tag{3.22}$$

and finally, the trigonometric identity

$$\cos^3(\omega t) = \frac{3}{4}\cos(\omega t) + \frac{1}{4}\cos(3\omega t) \tag{3.23}$$

allows to establish a mathematical relation between the third order damping term and a the third harmonic in the dynamic damping moment. This connection becomes important for the interpretation of the results Fig. 4.35 in Sec. 4.3.1.

$$-I\phi_A\omega^2\sin(\omega t) + \left[B_1\phi_A\omega + B_3\frac{3}{4}\phi_A^3\omega^3\right]\cos(\omega t) + B_3\frac{1}{4}\phi_A^3\omega^3\cos(3\omega t) = \mathrm{M}_{\mathrm{dyn}}(t) \tag{3.24}$$

In the following section, the time series analysis procedure for forced motion data is described. During a forced motion test the measured quantity is the roll moment M_ϕ, which is the reaction to the forced roll motion $\phi(t) = \phi_A \sin(\omega t)$.

Figure 3.10 shows an example of the roll moment time series computed with the CFD toolbox OpenFOAM. The alphanumeric string in the title of the figure was used to identify the simulation case parameter in the systematic simulations described in Sec. 5.2. The character sequence `dS1D3a1633` mean, that the shape variation S001 of the DTC ship hull was used with a draft of $D = 14\,\mathrm{m}$ without bilge keel or rudder. The height of the roll axis over water level was $raz = 0.0\,\mathrm{m}$, the ship speed $U = 12.861\,\mathrm{m/s}$, the roll period $T_{\mathrm{roll}} = 19.0\,\mathrm{s}$ and the roll amplitude $\phi_A = 20\,°$.

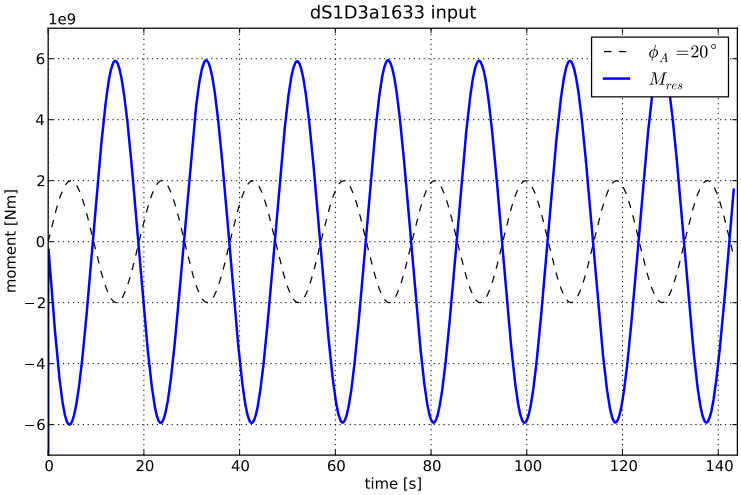

Figure 3.10.: Roll moment time series computed with OpenFOAM

First, the data is read from file and checked, if the time series is sufficient long enough to provide at least three full roll cycles for the analysis procedure. Next, it is checked if each cycle contains enough data points and whether the time step size is constant or not. If not the FFT and DFT analysis described in section 3.2 require that the time series has to be unified. Also, if the time series is too noisy, a smoothing operation is applied, to ensure that the zero crossing method correctly finds the beginning and ending of a roll cycle. The subsequent time series analysis steps will be applied to the not smoothed data.

Once the data is read and checked, the time series is split into multiple sets, each containing the data of one roll cycle. The time series is split at each zero crossing of a falling slope of the roll angle $\phi(t)$. By analyzing each cycle separately its is possible to detect a potential change from cycle to cycle.

In model tests and CFD simulations the total roll moment $M_{\mathrm{res}}(t)$ is recorded. If the restoring moment is unknown, it can be estimated with the hydrostatic computation method described in Sect. 3.4. Subtracting the hydrostatic restoring moment from the total moment results in the dynamic roll moment (3.25), which is composed of an inertia $M_{\mathrm{inertia}}(t)$ and a damping part $M_{\mathrm{damp}}(t)$.

$$M_{\mathrm{dyn}}(t) = M_{\mathrm{res}}(t) - M_{\mathrm{stat}}(t) \tag{3.25}$$

The sine and cosine terms in Eq. (3.25) show that the linear inertia and damping moment are 90° phase shifted and thereby independent of each other. This property allows the analysis method to determine both inertia and damping coefficients. In general, the amplitudes $\hat{M}$ of the different moments follow the rule $\hat{M}_{\mathrm{stat}} >> \hat{M}_{\mathrm{inertia}} >> \hat{M}_{\mathrm{damp}}$.

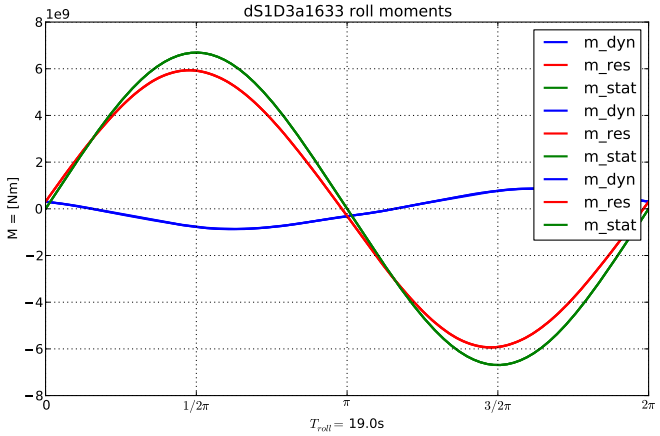

Figure 3.11.: Total, static and dynamic roll moment for three roll cycles (almost identical for each cycle)

Figure 3.11 shows an overlay of the last three roll cycles of the time series shown in Fig. 3.10. In addition to the measured resulting roll moment, the figure shows the predicted hydrostatic moment and the computed dynamic moment.

A qualitative comparison of the three time series (M_{res}, M_{dyn} and M_{stat}) in Fig. 3.11 shows an unexpected effect of the different roll moments: The hydrostatic restoring moment has a larger amplitude than the total roll moment M_{res}. This effect can be explained by the inertia moment which acts against the roll acceleration and the damping moment which acts against the velocity.

Another feature is the time shift of the peak of the dynamic moment. The dynamic moment has a phase shift compared to the hydrostatic moment which is in phase with the roll angle. This phase shift originates from the damping moment and can also be used to determine the damping coefficient.

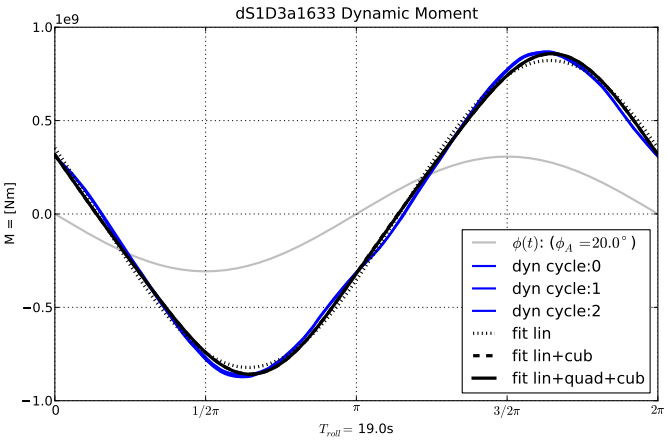

Figure 3.12.: Dynamic moment and damping models of varying polynomial order

Figure 3.12 shows in blue the dynamic moment cycles from Fig. 3.11 together with the time series of the roll angle in gray to emphasis the phase shift to the dynamic moment. The three cycles are almost the same which shows that transient oscillation effects have disappeared and that no non-harmonic distortions (eg. from wave reflections) occur.

To compute the amplitude coefficients from the dynamic moment either the DFT or the LS analysis described in Sec. 3.2 can be used (For nonlinear damping model, the LS analysis achieves better results). By splitting the time series into separate cycles and determining the coefficients individually, more statistical information can be derived. This approach allows to compute the mean value, standard deviation and a possible transient effect trend from cycle to cycle.

$$a_1\ddot{\phi}(t) + b_1\dot{\phi}(t) = M_{\mathrm{dyn}(t)} \quad \text{lin.} \tag{3.26}$$

$$a_1\ddot{\phi}(t) + b_1\dot{\phi}(t) + b_3\dot{\phi}^3(t) = M_{\mathrm{dyn}(t)} \quad \text{lin.+cub.} \tag{3.27}$$

$$a_1\ddot{\phi}(t) + b_1\dot{\phi}(t) + b_2|\dot{\phi}(t)|\dot{\phi}(t) + b_3\dot{\phi}^3(t) = M_{\mathrm{dyn}(t)} \quad \text{lin.+quad.+cub.} \tag{3.28}$$

Equation (3.26)-(3.28) list roll damping model of increasing complexity. With every of these models the coefficients a_1, b_1, b_2, etc can be determined. Using these coefficients, the corresponding model and the roll angle function $\phi(t)$ in Eq. (3.24) a *synthetic* roll moment time series M_{syn} can be generated. When plotted together with the measured dynamic moment cycles in Fig. 3.12 it can be assessed which model matches the time series the best.

$$Q = ||M_{\mathrm{dyn}} - M_{\mathrm{syn}}||_2 \tag{3.29}$$

Apart from a visual comparison the quality of the damping model can also be numerically evaluated. By calculating the euclidean norm $||\cdot||_2$ from the difference

of the dynamic and the *synthetic* moment, a value Q (3.29) can be determined that provides a numerical measure for the deviation between damping model and measured data. The model with the lowest Q achieves the best fit to the time series. The linear plus quadratic plus cubic model (3.28) has the smallest Q, but is only slightly better than the linear plus cubic model (3.27).

Once the amplitude coefficients of the damping model (b_1, b_2,...) are determined, the non-dimensional damping coefficients $\hat{B}_{44,lin}$ and $\hat{B}_{44,equi}$ can be computed according to the definitions in Sec. 2.4.

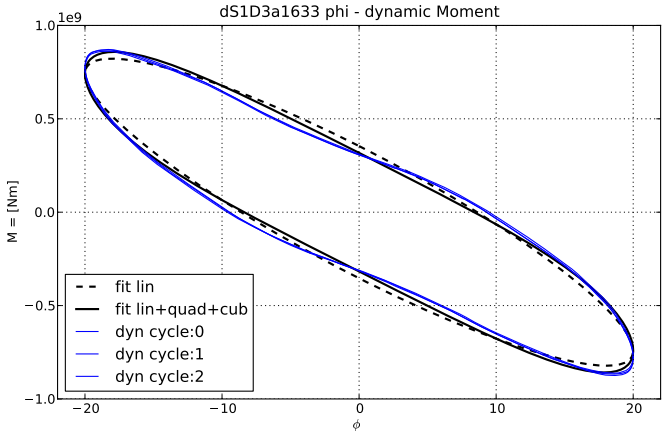

Figure 3.13.: Phase plot of the dynamic roll moment

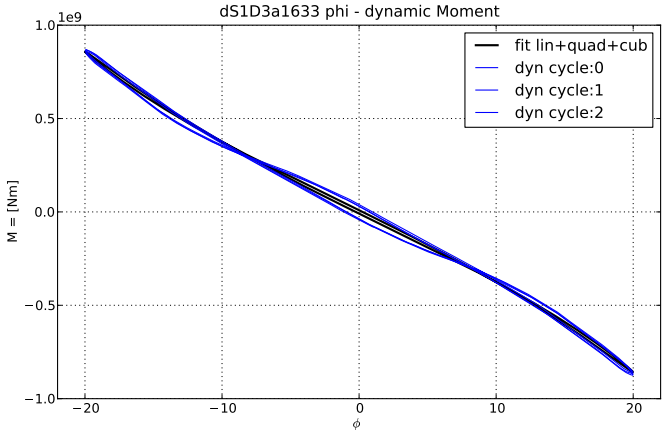

Figure 3.14.: Phase plot of the dynamic moment; shifted by Δt

Figure 3.13 shows an alternative way to plot and analyze the dynamic roll moment. If the dynamic moment is plotted over the roll angle a circular phase plot

is generated. The shape of the circle contains the information about the amount of damping in relation to inertia.

The damping can be expressed in form of a phase shift angle, ranging from 0° (no damping, the plot would be a straight line) to 90° (only damping, the plot forms a perfect circle). In the case of the dynamic moment shown in Fig. 3.13 the non linear effect can be seen in form of a higher harmonic that oscillates around the circular shape. The phase plot also gives a better impression of how good the synthesized time series fits the dynamic moment.

Once the linear coefficients a_1 and b_1 are determined, they can be used to compute the phase shift Δt. Shifting the dynamic moment times series by $-\Delta t$ removes the linear damping component from the time series. Figure 3.14 shows the same time series as Fig. 3.13 but with this negative phase shift applied. In this form, the higher order model terms can be determined with a polynomial Ansatz function fitted to the data, which is equivalent to the harmonic function used in Eq. (3.23).

In the case of large roll angle amplitudes a nonlinear effect occurs which cannot be captured with the above described damping model. This is due to the fact that it stems from the nonlinear restoring moment and only correlates with the roll angle ϕ but not with the angular velocity $\dot{\phi}$, which controls the damping moment. The effect of the nonlinear restoring moment is described in Sec. 3.4.

3.4. Restoring Moment

A function for restoring moment M_{stat} is required for the simulation of the roll motion. Although the moment can be approximated with the $M_{\text{stat}} \approx \Delta\overline{GM}\phi$, this equation is only a coarse estimate and neglects the nonlinear moment for large roll angles. For a new hull shape or if the loading condition is not defined, the metacentric height $\overline{GM}$ may not be available and has to be estimated or computed.

In addition to the restoring moment the other ship parameter also need to be determined in order to categorize the hull shape variations and generate data sheets. Furthermore a tool is needed that allows to compute specific lines along the curved hull surface in order to determine the position of future bilge keel plates. For this purpose the python routines described in this section were further extended into a CAD design tool for parametric bilge keels (see appendix A.5).

The following section describes procedures which were used to automatically compute the hull shape coefficients, ship lines and hydrostatic restoring moment for a given loading condition.

Python provides a programming interface (API) to the Visualization ToolKit (VTK) [66] which allows to access to most of the required mathematical operations. At program start the hull geometry is read from a CAD file in STL format (the STL format uses triangle tessellation to define a 3D surface) and converted to a

VTK data object (a list of triangles defined by three vertices). Additional input parameter are the draft, the position and direction of the roll axis, the roll angle range and the position of the aft perpendicular.

In a first step the hull surface is translated to the given draft and divided by a cutting plane into a surface above and below the water plane. The underwater surface is used to computed the wetted area, the hydrostatic pressure, the beam, the length between perpendiculars, the buoyancy force (displacement), the block coefficient, prismatic coefficient and center of buoyancy. Table 5.1 lists the ship coefficients for the base form of the three investigated ship types, computed with the above described python program.

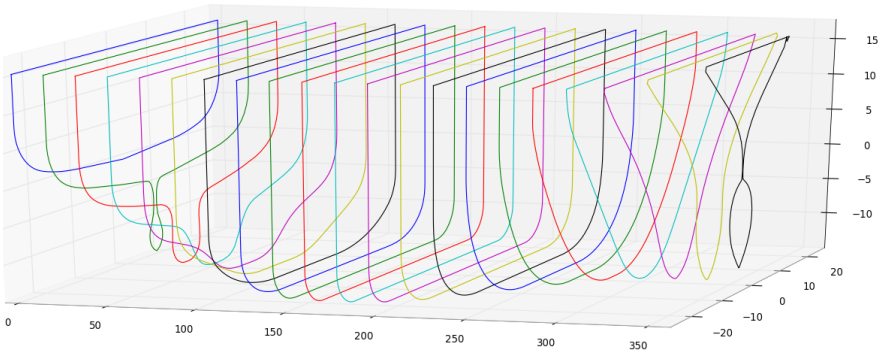

Figure 3.15.: Isometric view of the sections of the DTC along the longitudinal axis

Another VTK operation is the intersection of a surface and a plane which results in a list of line elements. Intersecting the hull surface with the water plane allows to compute the water plane area and coefficient. Moving the intersection plane along the coordinate axis allows to compute the ship lines. Figure 3.15 shows an isometric view of the section cuts along the longitudinal axis. These sections are used in Sec. 3.5 for the computation of the added mass.

The restoring moment is determined by rotating the hull in small steps and computing the hydrostatic force one each facet of the hull surface. The total restoring moment results from the sum of the pressure force on each facet and its respective lever arm. Figure 3.16 shows the restoring moment of the PanaMax ship for three different roll axis heights above the water plane. The figure shows the effect that a lower center of gravity (assumed to coincide with the roll axis) increases the stability and the restoring moment has a noticeable nonlinear slope for roll angle above 10°.

The roll angle depended restoring moments are used to create a time series the for restoring moment $M_{\text{stat}}(\phi)$. By using the previously described time series

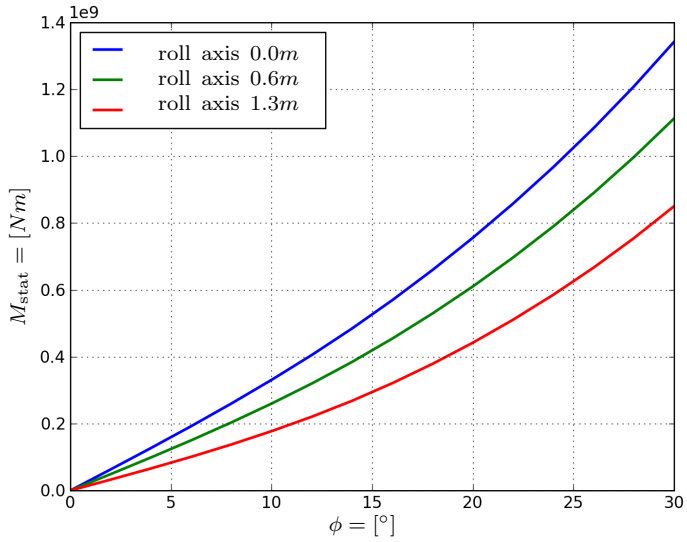

Figure 3.16.: Restoring moment for the PanaMax for three roll axis heights

analysis procedure the polynomial equation (3.30) can be fitted to the restoring moment.

$$C(\phi) = C_1\phi + C_3\phi^3 + C_5\phi^5 \tag{3.30}$$

The resulting coefficients C_1, C_3 and C_5 are then used for the hydrostatic restoring moment in Eq. (3.7). The influence of the higher order terms can be measured by the quotients C_1/C_3 and C_1/C_5. The smaller the quotient are, the stronger the nonlinear behavior of the restoring moment is. With a fifth order approximation (eq. (3.30)), the error between restoring moment and fitted moment is less than 0.001 degree for any roll angle up to 20 degrees.

3.5. Added Mass

Beside the damping moment and the restoring moment discussed in the two previous sections, the dynamic roll motion (see Eq. (2.2)) is governed by the inertia of the ship. The analysis process presented Sec. 3 and also illustrated in figure 3.1 indicates why a good estimate of the ships roll inertia can be used to improve development procedure. Although the inertia is not directly required to determine the linear damping coefficient, the inertia coefficient is needed for the simulation of the roll equation (3.1) and helps to simplify the separation of the dynamic roll moment into its inertia and damping components.

In principle, a body, that is immersed in a fluid and submitted to acceleration, experiences two types of reaction forces: An inertia force due to the body's mass

and a surface force due to acceleration of the surrounding fluid. This fluid force seems to increase the mass inertia of the body, hence the term *added mass*.

For the roll motion around the x-axis the total moment of inertia I_{xx} is defined as the sum of the mass inertia of the ship hull and the hydrodynamic inertia:

$$I_{xx} = I_{\text{hull}} + I_{\text{add}} \tag{3.31}$$

This inertia coefficient directly effects the roll motion behavior by its influence on the roll period and also, but to a lesser extent, the roll damping (see Sec. 3.1). The inertia coefficient is also related to the shape coefficients used in the simple Ikeda method (see Sec. A.4).

In the following section, the most common empirical estimation rules are briefly stated, follow by detailed description of the strip method and the boundary element method (BEM).

In a first approach, the added mass may be estimated empirically: According to Biran [67] the added mass (for roll motion) can be assumed to be 15% of the ship displacement with an additional 6% if bilge keels are present. In [56] the additional area moment of inertia is defined to be 10% of the ships dry mass inertia. If the beam of the ship is known, the moment of inertia $I_{xx} = mk_{xx}^2$ can be approximated by using an empirical equation for the radius of gyration $k_{xx} = 0.4 \cdot \text{beam}[m]$ (Biran [67]). In general, the more the shape of the hull deviates from a cylinder, the larger is the added mass and its influence on the roll motion.

The objective of this thesis is to study the influence of the hull shape on roll damping. For this purpose, these empirical rules are not accurate enough or they were derived from slim hull shapes, which deviate too much from modern, bulky hulls.

In order to obtain a better, shape dependent approximation of the added mass, the strip method in combination with a 2D potential flow solver can be applied. This approach represents a good compromise between a rough empirical estimate and a very time consuming computation of a 3D viscous flow problem.

The term strip method denotes the procedure to divide the ship hull into strips (see Fig. 3.15), determine the added mass for each of these 2D problems and compute the total added mass by summing up the contribution of each section. The key principle of the strip method is that 3D flow effects can be neglected and that the shape dependent inertia coefficient can be obtained with a simplified flow model, in this case a non viscous potential flow. Commonly the inertia coefficients are being estimated using a Lewis form transformation [67], but in order to include the influence of the bilge keels, the BEM is used.

In BEM, the fluid flow is discretized only on the domain boundary. This feature allows to account for any hull shape and bilge keel geometry while offering a short computation time. The following section presents a compact summary of the BEM

procedure. The mathematical theory and discretization schemes are described in detail in the book by Liu *Fast Multipole Boundary Element Method: Theory and Applications in Engineering* [68] and in the article Liu et al [69].

The governing equation for a potential flow problem can be derived from the continuity equation (2.3) by assuming the flow to be steady, incompressible and irrotational (which also implies zero viscosity). The assumption that the flow is irrotational ($\nabla \times \mathbf{u} = 0$) and the vector identity that states that the curl of the gradient of any scalar field Φ is always zero ($\nabla \times \nabla\Phi = 0$) [60], is used to derive the velocity potential

$$\mathbf{u} = \nabla\Phi \tag{3.32}$$

Replacing the velocity vector $\mathbf{u}$ with the gradient of the velocity potential $\nabla\Phi$ in the steady, incompressible continuity equation $\nabla \cdot \mathbf{u} = 0$ results in the Laplace equation for a potential flow:

$$\nabla \cdot (\nabla\Phi) = \nabla^2\Phi = 0 \tag{3.33}$$

By including a volume or point source f, the Laplace equation becomes the Poisson equation:

$$\nabla^2\Phi + f = 0 \quad \text{in } \Omega \tag{3.34}$$

The equation is defined on the domain Ω with the boundary $\Gamma = \Gamma_D \cup \Gamma_N$. The boundary conditions can be given by either Dirichlet (subscript D) or Neumann (subscript N) conditions:

$$\Phi = \Phi_0 \quad \text{on } \Gamma_D \tag{3.35}$$

$$\frac{\partial\Phi}{\partial n} = q_0 \quad \text{on } \Gamma_N \tag{3.36}$$

On the assumption that there exists a fundamental solution $G(\mathbf{x}, \mathbf{y})$, depending on a source point $\mathbf{x}$ and a field point $\mathbf{y}$ and replacing the source term with the Dirac point source $\delta(\mathbf{x}, \mathbf{y})$, equation (3.34) becomes an Ansatz solution for the potential problem:

$$\nabla^2 G(\mathbf{x}, \mathbf{y}) + \delta(\mathbf{x}, \mathbf{y}) = 0 \tag{3.37}$$

The theory of the boundary element method is based on the equivalent transformation of the flow equation (3.34) defined on domain Ω into a boundary integral equation (BIE) defined only on the boundary Γ of the domain. The derivation of the BIE is based on Green's second identity:

$$\int_\Omega \left(\eta\nabla^2\xi - \xi\nabla^2\eta\right) d\Omega = \int_\Gamma \left(\eta\frac{\partial\xi}{\partial n} - \xi\frac{\partial\eta}{\partial n}\right) d\Gamma \tag{3.38}$$

Using identities $\xi = \Phi(\mathbf{y})$ and $\eta = G(\mathbf{x}, \mathbf{y})$ equation (3.38) becomes:

$$\int_\Omega G(\mathbf{x},\mathbf{y}) \underbrace{\nabla^2\Phi(\mathbf{y})}_{=-f} - \Phi(\mathbf{y}) \underbrace{\nabla^2 G(\mathbf{x},\mathbf{y})}_{=-\delta(\mathbf{x},\mathbf{y})} d\Omega = \int_\Gamma G(\mathbf{x},\mathbf{y}) \underbrace{\frac{\partial\Phi(\mathbf{y})}{\partial n}}_{=q} - \Phi(\mathbf{y}) \underbrace{\frac{\partial G(\mathbf{x},\mathbf{y})}{\partial n}}_{=F(\mathbf{x},\mathbf{y})} d\Gamma \tag{3.39}$$

Green's 2nd identity is further transformed by applying the Poisson equation (3.34) on $\nabla^2\Phi$, denoting the derivative $\frac{\partial G(\mathbf{x},\mathbf{y})}{\partial n(\mathbf{y})}$ with $F(\mathbf{x}, \mathbf{y})$ and using the kinematic boundary condition $\frac{\partial\Phi}{\partial n} = q$ (Eq. (3.36)).

The term $\nabla^2 G(\mathbf{x}, \mathbf{y})$ is replaced by $-\delta(\mathbf{x}, \mathbf{y})$ using the Ansatz solution Eq. (3.37). This leads to the integral $\int_\Omega \Phi(\mathbf{y})\delta(\mathbf{x}, \mathbf{y})d\Omega$ which is transformed to $\Phi(\mathbf{x})$ using the *sifting* property of the Dirac function.

Moving the remaining integral term to the right side leads to the fundamental solution of the potential problem:

$$\Phi(\mathbf{x}) = \int_\Gamma \left(G(\mathbf{x},\mathbf{y})q(\mathbf{y}) - F(\mathbf{x},\mathbf{y})\Phi(\mathbf{y})\right) d\Gamma + \int_\Omega G(\mathbf{x},\mathbf{y})f(\mathbf{y})d\Omega \tag{3.40}$$

A detailed presentation of the limit value analysis and the use of Cauchy principle value integration to remove the singularity on the boundary element when $\mathbf{x}$ tends to Γ is given in Liu [68]. Equation (3.41) states the result of Liu's mathematical transformations, the conventional boundary integral equation (CBIE):

$$c(\mathbf{x})\Phi(\mathbf{x}) = \int_\Gamma \left(G(\mathbf{x},\mathbf{x})q(\mathbf{y}) - F(\mathbf{x},\mathbf{y})\Phi(\mathbf{y})\right) d\Gamma + \int_\Omega G(\mathbf{x},\mathbf{y})f(\mathbf{y})d\Omega \tag{3.41}$$

The coefficient $c(\mathbf{x}) = 1/2$ is constant for straight line elements which are used in the following computations.

A commonly used Ansatz function for the kernel $G(\mathbf{x}, \mathbf{y})$ and its derivative in normal direction $F(\mathbf{x}, \mathbf{y})$ is:

$$G(\mathbf{x},\mathbf{y}) = \frac{1}{2\pi}\log\left(\frac{1}{r}\right) \tag{3.42}$$

$$F(\mathbf{x},\mathbf{y}) = \frac{\partial G(\mathbf{x},\mathbf{y})}{\partial n(\mathbf{y})} = -\frac{1}{2\pi r}\frac{\partial r}{\partial n} \tag{3.43}$$

with $\mathbf{r}$ pointing from the source point $\mathbf{x}$ to the field point $\mathbf{y}$ and the distance $r = |\mathbf{r}|$.

The discretization of the CBIE (Eq. (3.41)) with constant line elements along boundary Γ can be written as a system of linear equations:

$$\frac{1}{2}\Phi_i = \sum \left(g_{ij}q_j - \hat{f}_{ij}\Phi_j\right) \tag{3.44}$$

where g_{ij} and $f_{ij} = \hat{f}_{ij} + \frac{1}{2}\delta_{ij}$ are numerical integrals of G and F over the line elements $\Delta\Gamma$ with respect to the midpoint x_i on the line element and the field point y_j.

$$g_{ij} = \int_{\Delta\Gamma_j} G_i d\Gamma \tag{3.45}$$

$$\hat{f}_{ij} = \int_{\Delta\Gamma_j} F_i d\Gamma \tag{3.46}$$

Equation (3.44) can be written in a compact form using matrix notation:

$$\frac{1}{2}\mathbf{I} + \mathbf{F\Phi} = \mathbf{Gq} \tag{3.47}$$

$$\Rightarrow \mathbf{A\lambda} = \mathbf{b} \tag{3.48}$$

If the CBIE contains mixed Dirichlet and Neumann boundary conditions the columns and rows of the matrices in Eq. (3.47) have to be sorted, so that the known parameter are grouped in the right hand side vector $\mathbf{b}$, the unknown variables in vector $\mathbf{\Phi}$ and the dense coefficient matrix $\mathbf{A}$. The resulting linear system can be solved with a standard linear algebra solver. The discretized formulation of the line integrals for constant elements and a procedure for the assembly of the linear system are also provided in Liu's book [68].

The solution of Eq. (3.48) results in a velocity potential on every boundary element. To compute the flow field within the domain the potential for an arbitrary grid of field points $\mathbf{y}$ is determined by evaluating $\Phi(\mathbf{y})$ (Eq. (3.41)) for all boundary elements.

The above described BEM procedure was implemented in python and used to compute the flow field around 2D hull sections. To avoid the treatment of a free surface, the hull was modeled as a double body. Figures 3.17 to 3.20 show the flow fields around a single bilge keel plate, the main section of the DTC hull without a bilge keel and a detailed view of the main section with an attached bilge keel plate. Figure 3.17 and 3.19 show the velocity magnitude while the flow in 3.18 and 3.20 is represented by potential- and stream lines.

In principle, once the velocity potential on the body surface is known, the Bernoulli equation

$$p = -\rho\left(\frac{\partial\Phi}{\partial t} + \frac{1}{2}|\nabla\Phi|^2 + f_g z\right) \tag{3.49}$$

could be used to determine the pressure on a line element. Here, f_g is the gravitational constant, z the vertical distance and ρ the fluid density. But due to the D'Alembert's paradox [19] the integral of the forces over the body cancel each other out.

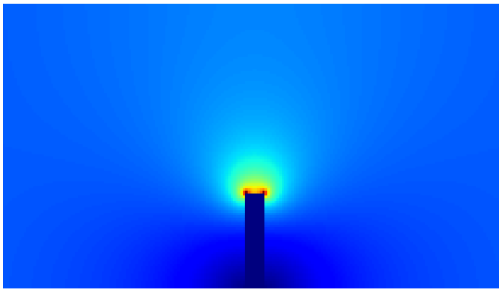

Figure 3.17.: Velocity magnitude around a bilge keel

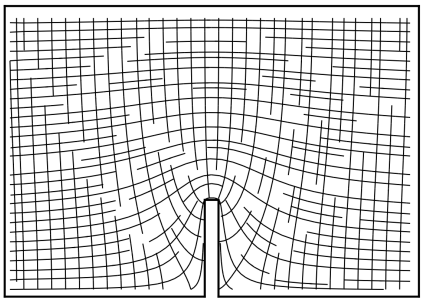

Figure 3.18.: Potential- and streamlines around a bilge keel

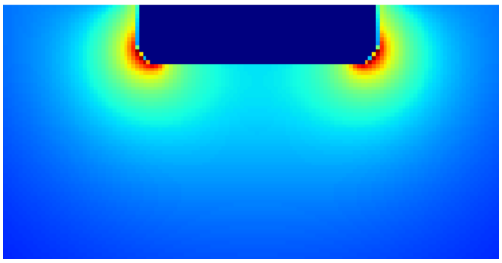

Figure 3.19.: Velocity magnitude around a rolling hull section

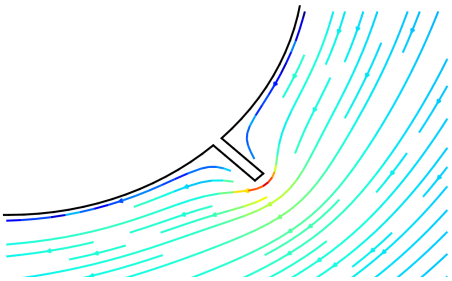

Figure 3.20.: Streamlines around bilge keel

An equation for the hydrodynamic inertia or added mass can be derived from the momentum equation. The momentum L can be defined in form of a double integral of density ρ and acceleration $\mathbf{a}$ over volume Ω and time $t \in 0 \dots T$:

$$L = \int_0^T \int_\Omega \rho \mathbf{a}(t) d\Omega dt = \int_\Omega \rho \mathbf{u} d\Omega = m\,\mathbf{u} \tag{3.50}$$

Replacing the velocity $\mathbf{u}$ by the gradient of the velocity potential $\nabla\Phi$ and applying the divergence theorem transforms the volume integral into a surface integral over the body surface Γ:

$$L = \int_\Omega \rho \nabla\Phi d\Omega = \int_\Gamma \rho\Phi \cdot \mathbf{n} d\Gamma \tag{3.51}$$

By applying the kinematic boundary condition $\frac{\partial\Phi}{\partial n} = \mathbf{u} \cdot \mathbf{n}$ (Eq. (3.36)) and using a unit vector $\mathbf{e}_u$ for the velocity (the added mass scales linearly with the velocity),

the equation for the added mass can be reformulated to the expression:

$$L = \rho \int_{\Gamma} \Phi \frac{\partial \Phi}{\partial n} d\Gamma \tag{3.52}$$

which directly leads to the added mass. Finally, through the computation of the sum of the coefficients for each hull section (strip method) the added mass of a ship with zero forward speed can be determined.

4. Viscous Roll Damping

The development of a roll damping prediction method requires a method that includes viscosity. The large number of shape variations prevents the use of model tests, but an alternative option is to use a numerical field method to simulate a ship's roll damping behavior in a viscous fluid. The computational procedure and the assessment of the results require a validated Navier-Stokes (NS) solver for the simulation of a turbulent multiphase flow in interaction with a moving ship hull.

The following chapter is structured in three parts: First, a description of the used numerical methods, followed by several validation cases of increasing complexity and in the last part the case setup and solution procedure used for the systematic shape variation are presented.

4.1. Navier-Stokes Solver

For the simulation of the viscous flow around a ship hull the Navier-Stokes equations (2.3) and (2.4) are numerically approximated. The chapter begins with a brief introduction to the finite volume method (FVM), which is a common discretization technique in computational fluid dynamics (CFD).

The subsequent paragraphs describe further methods that are needed for numerical roll motion simulation. The volume of fluid (VOF) method is used to capture the free surface and due to the high Reynolds number of a ship flow a turbulence model (RANS) is used. For selected applications – where more detailed information about the vortex structure is required – the large eddy simulation (LES) turbulence model is used. Furthermore a dynamic FV mesh method has to handle the motion of the ship hull.

For the description of the conservation equations and discretization schemes reference is made to the books by Ferziger and Perić [23] and Versteeg [24]. The numerical solution of the flow problem is computed with the open source CFD software OpenFOAM [70]. To validate OpenFOAM, results from model tests and numerical simulations are compared. Further, results obtained by StarCCM+ [71] and a CFD Code called *Comet* (Comet was developed at the University of Hamburg, Germany and was later merged with CD-Adapco [71]) are used for validation.

4.1.1. Governing equations

The incompressible Navier-Stokes equations (4.1) and (4.2) (see (2.3) and (2.4) in Sec. 2.2) in differential form are:

$$\nabla \cdot \mathbf{u} = 0 \tag{4.1}$$

$$\frac{\partial \mathbf{u}}{\partial t} + (\mathbf{u} \cdot \nabla)\,\mathbf{u} = -\frac{1}{\rho}\nabla p + \nu \Delta \mathbf{u} + \frac{1}{\rho}\mathbf{f} \tag{4.2}$$

The field variables are the scalar pressure p and the velocity vector $\mathbf{u}$ (instead of the bold notation, a vector can be written in *Einstein notation* $\mathbf{u} = u_i$). The volume force $\mathbf{f}$ is used to model gravitation and the density ρ is a constant for incompressible fluid. The divergence operator is written in form of the dot product of the gradient and the vector field $\mathrm{div}(\mathbf{u}) = \nabla \cdot \mathbf{u}$ and for the advection term exist two equivalent notations $(\mathbf{u} \cdot \nabla)\mathbf{u} = \nabla \cdot (\mathbf{u}\mathbf{u})$.

By applying a volume integration over the flow domain V and using the divergence theorem to transform the volume integral into a surface integral, the NS equations are transformed into their integral form. Dividing the flow domain into n polyhedral control volumes V and applying spatial and temporal discretization schemes on the integral terms lead to a system of equations that form the finite volume method.

The computations described in the following sections were all computed with a *Semi-Implicit Method for Pressure Linked Equation* (SIMPLE) or *Pressure Implicit with Splitting Operators* (PISO) scheme. These projection or predictor corrector schemes solve the flow problem by an iterative coupling of velocity and pressure field.

Both schemes are based on the so called pressure-Poisson equation which is derived by applying the continuity equation (4.1) on the the momentum equation (4.2). In the SIMPLE scheme the impulse equation and an initial guess for the flow field is used to compute an intermediate velocity field. This field is then corrected with the solution of the pressure equation, resulting in a new velocity field. These steps are repeated until a certain convergence criterion is reached. To improve the numerical solution of the pressure Poisson equation, often an under-relaxation of the pressure field is applied (Versteeg [24]). The PISO scheme is similar to the SIMPLE scheme and uses one or more additional pressure corrections steps.

4.1.2. Multi-Phase Flow

In OpenFOAM a ship flow with free surface water waves is simulated with the volume of fluid (VOF) method (Jasak [72], Hirt and Nichols [20] and Rusche [73]). The multiphase flow uses an additional scalar variable $\alpha \in [0, 1]$ that represents

the amount of water in a control volume. The dynamic behavior of α is defined by the transport equation (4.3).

$$\frac{\partial \alpha}{\partial t} + \nabla \cdot (\mathbf{u}\alpha) = 0 \tag{4.3}$$

The dynamic viscosity μ and the density ρ are defined as a mix of the properties of the two fluids 1 and 2: μ_1, μ_2 and ρ_1, ρ_2.

$$\mu = \alpha\mu_0 + (1-\alpha)\,\mu_1 \tag{4.4}$$
$$\rho = \alpha\rho_0 + (1-\alpha)\,\rho_1 \tag{4.5}$$

4.1.3. Turbulence Model

The large Reynolds number ($\approx 10^6$ for model scale and $\approx 10^9$ for full scale ships) prevent the computation of the ship flow with direct numerical simulation (DNS) within reasonable time or computational effort. Instead the RANS equations (4.9) and (4.8) are used to compute the turbulent flow. These equations are derived from the NS equations by splitting the field variables for velocity u_i and pressure p into a mean value $\overline{u_i}$ and a fluctuation part u_i':

$$u_i = \overline{u_i} + u_i' \tag{4.6}$$
$$p = \overline{p} + p' \tag{4.7}$$

By inserting the RANS variables into the NS equations, an additional term $\overline{u_i'\,u_j'}$ – the Reynolds stress tensor – is generated. This tensor contains additional unknowns which are determined with empirical equations [23].

$$\overline{u}_j \frac{\partial \overline{u}_i}{\partial x_j} = 0 \tag{4.8}$$

$$\frac{\partial \overline{u}_i}{\partial t} + \frac{\partial}{\partial x_j}\left[\overline{u}_i\overline{u}_j + \overline{u_i'\,u_j'}\right] = -\frac{1}{\rho}\frac{\partial \overline{p}}{\partial x_i} + \nu\frac{\partial}{\partial x_j}\left[\frac{\partial \overline{u}_i}{\partial x_j} + \frac{\partial \overline{u}_j}{\partial x_i}\right] \tag{4.9}$$

The idea of the turbulence model is to resolve large vortex structures within the computational mesh and to represent the high frequent turbulent part with a turbulence model. In ship flow application often the k-ω SST model (Menter [74]) is used. This turbulence model switches adaptively between the k-ϵ model in the far field and the k-ω model inside the turbulent boundary layer.

$$k = \frac{3}{2}(UI)^2 \tag{4.10}$$

$$\omega = \frac{\sqrt{k}}{l} \tag{4.11}$$

$$\epsilon = 0.09^{\frac{3}{4}} \frac{k^{\frac{3}{2}}}{l} \tag{4.12}$$

In order to compute the turbulent ship flow with the kωSST model the initial and boundary conditions for the turbulent kinematic energy k, the turbulent frequency ω and the turbulent dissipation rate ϵ have to be estimated. For this purpose the empirical equations (4.10) to (4.12) can be used [75]. U is the mean flow velocity and the turbulence intensity I is guessed for the initial flow field and at the inlet. In case of a ship flow were the fluid is at rest except near the hull, a turbulence intensity lower than $1\% \rightarrow I < 0.01$ can be assumed. That means that the velocity fluctuation in the fluid is less than one percent of the ship speed.

Further, the turbulent length scale l has to be estimated. The length defines the scale of the vortices generated by the turbulent flow. The value is estimated to be $1 \ldots 10\% \rightarrow l \approx 0.01 \ldots 0.1$ of the width of the projected area of the ship hull in flow direction (eg. the beam of the ship) (Pope [21], Versteeg [24]).

For flows with $Re \approx 10^9$ the velocity profile in the boundary layer and the position of the separation point cannot be resolved with common grid sizes. For flow problems with such high Reynolds numbers boundary wall functions are used that model the turbulent velocity profile with a empirical equation (Pope [21]).

The large eddy simulation (LES) turbulence model provides an alternative method to compute turbulent flows. The LES turbulence model in general can be compared to the RANS model. Both are based on a modification of the NS equation that separates the large and small scale of the turbulent motion and replaces the small scale part with additional model terms.

To derive the LES method, a low pass filter is applied to NS equations that removes the small scale high frequent turbulence. The remaining large scale motions are directly resolved while the small scale turbulent motion are computed with, for example, the first and most common Smagorinsky sub model.

4.1.4. Mesh Generation and Deformation

The mesh is generated with OpenFOAM tools. In a first step a Cartesian background mesh is generated with `blockMesh` and if needed further refinement steps are applied. Next `snappyHexMesh` is used to intersect the hull surface with the background mesh, the cells inside the hull are then removed and the cells near

the surface are aligned with the hull. In the last step the prism layer on the hull surface and further refinements are generated. All images of meshes in this and the next chapter were generated with `python` scripts that apply the above described steps automatically, depending on hull size and further control parameter.

To simulate a moving ship one of the following methods can be used:

- A rigid mesh motion is relatively easy to realize. In this method the whole mesh is moved according to the ship motion. The drawback of this approach is that the boundary conditions in the far field become more complex and that the refinement zones for the free surface have to be much larger in case of large roll angles.

- The *overset* method uses two meshes, a background mesh that spans the whole domain and a small mesh around the ship hull. Only the small mesh is moved and the flow fields are interpolated between the two mesh regions (the preservation of the continuity condition is hard to achieve). This method is very promising but unfortunately not freely available for OpenFOAM.

- For the mesh *morphing* method the cells near the hull are translated and distorted according to the hull motion. The principle of this approach can best be seen in Fig. 4.25. This method performs very well, but special care must be taken to ensure that the shape of cells near the hull surface do not become too distorted. This method is computationally costly, because the whole flow field has to be interpolated from the mesh at one time step to the mesh in the next time step.

- The *sliding interface* method also uses two mesh regions like the overset method. The difference is that both meshes do not overlap but are aligned to another and share a boundary interface. This method only requires the flow fields to be interpolated across this interface (see Fig. 5.7). A drawback of this approach is that not all direction of motions can be realized. A pure roll motion is easily realized but for example a combined roll and heave motion is much more complex to implement.

All of the roll decay simulations in this work were computed with the mesh morphing method. This test method requires multiple degrees of freedom only possible with this dynamic mesh method; and the larger computational cost was justified because of the small number of required simulations.

For the forced motion tests the sliding interface method was utilized since the ship was restricted to a pure roll motion and the large number of simulation cases required a fast computation routine.

4.1.5. Features of the Navier-Stokes Solver OpenFOAM

OpenFOAM is a open source CFD software developed among others by Henry Weller, Hrvoje Jasak and Henrik Rusche (Jasak [72], Jasak et al. [76] and Rusche [73]). OpenFOAM provides an implementation of FVM in C++ and provides a large number of discretization schemes and solution algorithms. A characteristic feature of OpenFOAM is that equations can be implemented using mathematical operators and the OpenFOAM compiler interprets the equation into executable code.

./sources/UEqn.H

```
3     tmp<fvVectorMatrix> UEqn
4     (
5         fvm::div(phi, U)
6       + turbulence->divDevReff(U)
7       ==
8         fvOptions(U)
9     );
10    UEqn().relax();
11    fvOptions.constrain(UEqn());
12    solve(UEqn() == -fvc::grad(p));
```

Figure 4.1.: OpenFOAM source code

./sources/dynamicMeshDict

```
17 #include "../../initialConditions"
18 dynamicFvMesh   solidBodyMotionFvMesh;
19
20 motionSolverLibs ( "libfvMotionSolvers.so" );
21
22 solidBodyMotionFvMeshCoeffs
23 {
24         cellZone        ROTOR;
25     solidBodyMotionFunction oscillatingRotatingMotion;
26     oscillatingRotatingMotionCoeffs
27     {
28         CofG            (0 0 $raz);
29         omega           $omegaAngFreq;          // rad/s
30         amplitude       ($phiMax 0 0);   // 45 degrees max tilt
31     }
```

Figure 4.2.: OpenFOAM dictionary dynamicMeshDict

The code lines in Fig. 4.1 show the principle implementation of a flow solver scheme in OpenFOAM. The example shows the first steps of the SIMPLE scheme.

In line 3 the discretized matrix equation `UEqn` depending on the velocity field U is constructed. Line 10 applies a relaxation operation on the velocity field and in the following line 11 the boundary conditions are applied. The command in line 12 solves the impulse equation with the use of the pressure corrector field. Every case file is a text file – a so called *dictionary* – containing keywords and the according values. An example for the configuration file `dynamicMeshDict` is shown in 4.2. The file contains the controls for the dynamic mesh motion. It defines which mesh libraries are to be used, which part of the mesh can rotate and what variables define the roll motion.

Figure 4.3 shows the file structure of a OpenFOAM simulation case. A typical case consists of three directories: a `0`-directory containing files with the initial and boundary conditions, a `constant`-directory containing the mesh and files with flow constants and a `system`-directory with configuration files for the numerical solver.

The files containing the initial and boundary conditions have a similar structure with the difference that they contain long lists with the numerical values on cell faces or points of mesh. Another central part of the case is the computational mesh. The folder `polyMesh` contains separate files with the definition of the mesh points, faces, cells and neighbor cells. The boundaries are defined in the file `boundary` that contains lists of the cell faces that compose a boundary patch.

Once the mesh is generated and the discretization schemes, solution control and boundary conditions are set up, the simulation case can be solved. OpenFOAM provides a list of solvers for different flow problems. These solver differ in their capability to handle steady or transient problems, with or without a free surface, the turbulence modeling and the type of mesh.

To gather the time series of the force and moment on the ship hull a OpenFOAM run time library is used. This *function object* computes every time step the sum of the fluid forces over the hull surface and writes the results to a text file. The roll moment is computed in a similar way with respect to a body fixed coordinate system and write to the same file.

In order to take the different density of water and air into account the program code of the function object was modified. By using the α fraction to distinguish between air and water only the fluid forced on the wetted hull surface can be computed. In addition, the function object was extended with a routine that calculates the calm water hydrostatic restoring moment using Pascal's law $p = \rho g h$ and the normal pressure force $\mathbf{f} = p\mathbf{n}A$. The variables in this context are the pressure p, gravitation constant g, water depth h, fluid density ρ, normal vector on area element $\mathbf{n}$ and size of area element A.

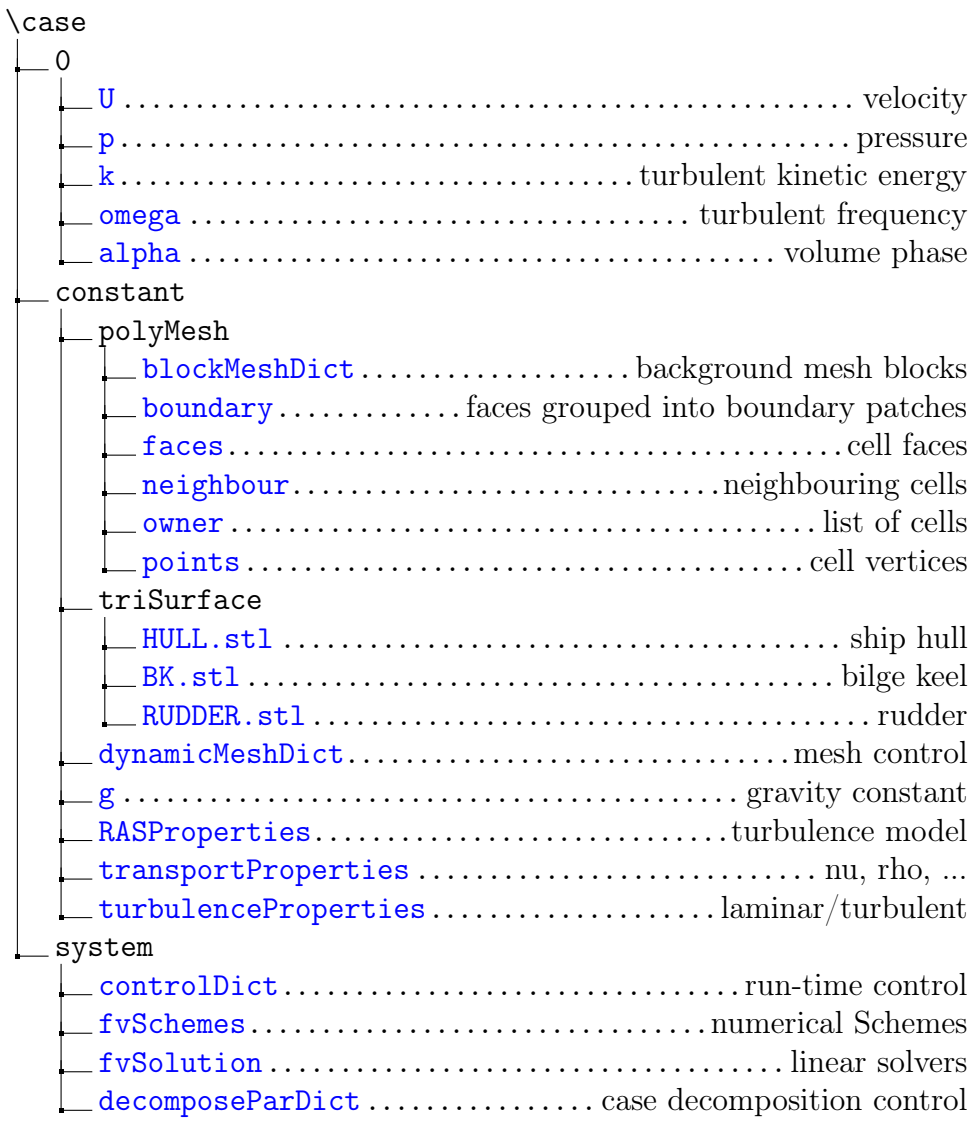

Figure 4.3.: Directory and file structure of an OpenFOAM case

4.2. Validation

In order to use OpenFOAM for the computation of a large number of complex roll damping cases, the NS solver has to be validated and the case setup tested. The usability of OpenFOAM to compute viscous roll damping is verified by several test cases with increasing complexity. They verified, either by comparison to empirical methods or measured results from model tests.

4.2.1. Drag and Lift of a Wing Section

To establish OpenFOAM for the computation of turbulent boundary layer flow a simple 2D test case is used. The NACA wing profile is a geometry that has been thoroughly investigated and documentation of the experimental results are freely available. The test setup of an inclined wing profile and the measured drag and lift coefficients are taken from Abbott and v. Doenhoff [77].

The profile used in the following section is a NACA 0012 wing profile. Table 4.1 lists the test conditions provided by the experimental data. These conditions were used to configure a matching CFD case with OpenFOAM. In order to keep

Table 4.1.: Case parameter for NACA wing section

wing profile		NACA 0012	
angle of attack	β	[0,4,8]	$[^\circ]$
chord length	c	1	$[m]$
density	ρ	998.8	$[kg/m^3]$
dyn. viscosity	ν	$1.09 \cdot 10^{-6}$	$[m2/s]$
Reynolds number	Re	$9 \cdot 10^6$	$[-]$
velocity	u	9.81	$[m/s]$
turb. kin. energy	k	$1.44 \cdot 10^{-4}$	$[m^2/s^2]$
turb. frequency	ω	12	$[s^{-1}]$
turb. dissipation rate	ϵ	$2.85 \cdot 10^{-4}$	$[m^2\, s^{-3}]$

the computational effort within limits, the wing profile is assumed to be two dimensional and therefore a 2D mesh can be used. The short computation time of a 2D case has the advantage that a lot of solution parameter can be tested. On the other hand 3D effects like turbulence cannot be resolved correctly. In 2D simulations a *blocking* effect has to be taken into account. This effect is described in more detail in Sec. 4.2.3.

Before the FV mesh can be generated, a STL file of the wing section has to be generated. For this purpose the mathematical equation a NACA profile defined in

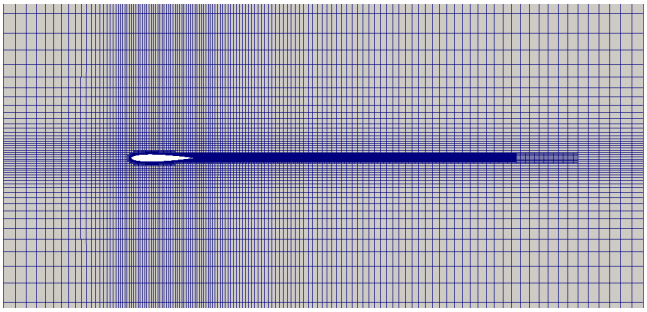

Figure 4.4.: FV mesh for NACA0012, $\beta = 0°$

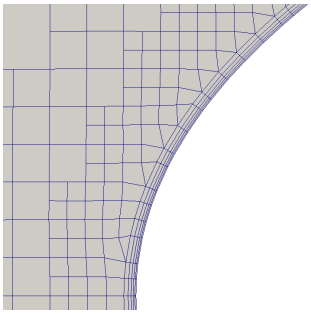

Figure 4.5.: Prism cells

Abbott [77] was implemented in a `python` script that generates a STL file depending on the four-digits NACA definition. Figure 4.4 and 4.5 show a view of the mesh generated with `blockMesh` and `snappyHexMesh`. The mesh extends beyond what the detailed views show. The domain size in the wake of the wing section is sixteen times the chord length l in the other direction the distance to the outer boundaries is eight times l. The background mesh and the refinement steps result in about 200 cells along the pressure or suction side. The size of the prismatic boundary layers shown in Fig. 4.5 were arranged in such a way that the dimensionless wall distance is $y^+ \approx 10 \ldots 20$. The experimental results in [77] are presented in form of the lift coefficient c_L and the drag coefficient c_D. These values can be compared the recorded forces from the CFD computation by using Eq. (4.13) and (4.14).

$$c_L = \frac{2F_L}{\rho u^2 A} \qquad (4.13) \qquad\qquad c_D = \frac{2F_D}{\rho u^2 A} \qquad (4.14)$$

The coefficients depend on the lift force F_L, the drag force F_D, the velocity u in the far field, the fluid density ρ and the reference area A, which is chord length times profile depth.

Table 4.2.: Deviation of the computed drag coefficient compared to the experimental results for the NACA0012 wing section

	steady		transient	
singlephase	`simpleFoam`	$C_D \approx +1\%$	`pimpleFoam`	$C_D \approx +4\%$
multiphase	`LTSInterFoam`	$C_D \approx -2\% \, (\pm 5\%)$	`interFoam`	$C_D \approx +4\%$

Table 4.2 lists the results of the viscous flow simulation of four OpenFOAM solver for an angle of attack of 4°. The table allows to compare the deviation of the CFD results from the experimental results depending on the solver type (steady or transient, single- or multiphase). In all simulations the kωSST two equation turbulence model and turbulent wall functions were used.

The results of the lift coefficient C_L (not shown in the table) are for all solver and all angles of attack smaller than 1% (as long no separation occurs). The drag coefficient C_D on the other hand depends on the solution procedure and the discretization method. The short computation time for this case allowed to test solver configurations with varying values for the turbulence parameter k and ω, Courant number, cell size and discretization method. Table 4.2 shows the best approximations of C_D that could be achieved with each solver. For all solver the deviation is positive and smaller than 4%, except the new solver `LTSInterFoam` which underestimates the drag by 2% when considering the mean value of the C_D time series. However the recorded force did not converge but started oscillating about $\pm 5\%$ about its mean. The results from the `LTSInterFoam` solver are questionable and should be interpreted with caution.

4.2.2. Viscous Hull Resistance

SVA-Potsdam test basin conducted resistance and propulsion tests with a model of the DTC ship in the scale $\lambda = 1 : 59.407$. The test conditions and RANS parameter (see Sec. 4.1.3) are listed in Tab. 4.3 and the results of resistance experience are shown in Tab. 4.4. All data is based on the SVA-Potsdam test report Nietzschmann [78] and el Moctar et al. [10].

The variables in Tab. 4.4 are ship speed U, Froude number Fr, total resistance R_T, total resistance coefficient C_T, Reynold number Re, frictional resistance coefficient C_F and residual resistance coefficient C_R. In order to validate OpenFOAM, the experimental data is compared with a CFD case closely modeled after the experimental test setup. The meshing procedure is in principle the same as in the prior section. The tools `blockMesh` and `snappyHexMesh` are controlled with a `python` script to generate a FV mesh with the required refinement zones and prism layer cells. In addition the domain region near the free surface has to be refined in order to capture the bow and stern waves generated by the hull.

The mesh in Fig. 4.6 shows another meshing feature needed for the computation of ship flows. The water waves emitted from hull propagate trough the domain and will be reflected on the boundary walls back to the ship. To dampen these waves before they are reflected, the cell size towards the domain boundaries are increased. This meshing procedure is called *cell grading*. The domain size is set in relation to the ship length. The inflow (red patch) is one ship length apart from the bow, the side patches have two times the distance and the back patch downstream

Table 4.3.: Test parameter for resistance test with DTC model ship and CFD RANS parameter

hull	DTC with rudder and without propeller	
scale factor	λ	$1 : 59.407$ $[-]$
draft	D	0.24407 $[m]$
wetted surface	S	6.315 $[m^2]$
water line	L_{WL}	6.177 $[m]$
density	ρ	998.8 $[kg/m^3]$
kinematic viscosity	ν	$1.09 \cdot 10^{-6}$ $[m^2/s]$
velocity	u	$1.335 \ldots 1.668$ $[m/s]$
turb. kin. energy	k	$1 \cdot 10^{-3}$ $[m^2/s^2]$
turb. frequency	ω	10 $[s^{-1}]$

of the stern is three times the ship length apart. The ship resistance was computed with two different setups: For the first variant the mesh for a double body hull is shown in Fig. 4.6. For this case type only the under water domain in mesh and on the top green surface patch symmetry boundary conditions were defined. This setup can be solved with a single phase solver and requires far less cells than a full mesh. The drawback is that wave effects cannot be captured. For the second method the domain above the green patch is also meshed and a multiphase solver is used, which allows to include water wave effects.

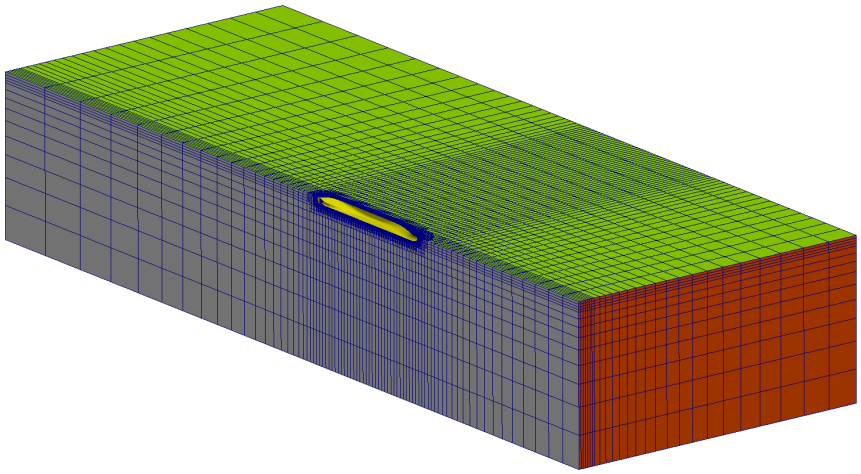

Figure 4.6.: Finite volume mesh for double body simulation

Table 4.4.: Test results of the DTC resistance measurements (model basin SVA Potsdam)

U $\left[\frac{m}{s}\right]$	Fr $[-]$	R_T $[N]$	C_T $[10^{-3}]$	Re $[10^6]$	C_F $[10^{-3}]$	C_R $[10^{-3}]$
1.335	0.172	20.34	3.619	7.6	3.1505	0.4686
1.401	0.180	22.06	3.561	7.9	3.1234	0.4376
1.469	0.189	24.14	3.549	8.3	3.0977	0.4517
1.535	0.197	26.46	3.562	8.7	3.0736	0.4879
1.602	0.206	28.99	3.581	9.1	3.0507	0.5307
1.668	0.214	31.83	3.626	9.5	3.0291	0.5967

Only a longitudinal speed is considered, which allows to use a symmetry condition on the center plane (gray patch in Fig. 4.6) reducing the number of required control volumes (cells) by half. Figure 4.7 shows the mesh with its refinement zones near the main section of the hull. The use of a wall function allows to capture the turbulent boundary layer with only five layers of relatively large prism cells. The final double body mesh has about $650k$ cells resulting in a dimensionless wall distance of $y^+ \approx 17 \ldots 22$.

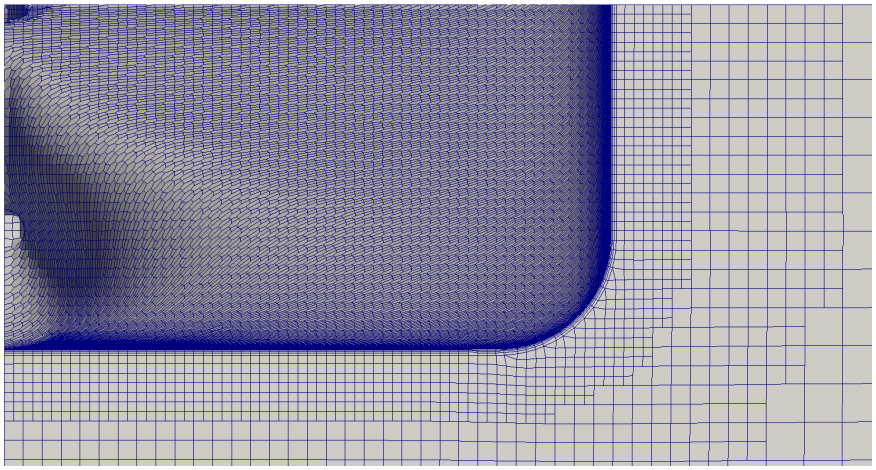

Figure 4.7.: Refinement zones and prism layer cells around DTC double body

The double body case was computed with the `simpleFoam` solver, kωSST turbulence model and wall function on the mesh shown in Fig. 4.6. A comparison of the friction forces obtained from the CFD simulation and the ITTC empirical formula showed good agreement.

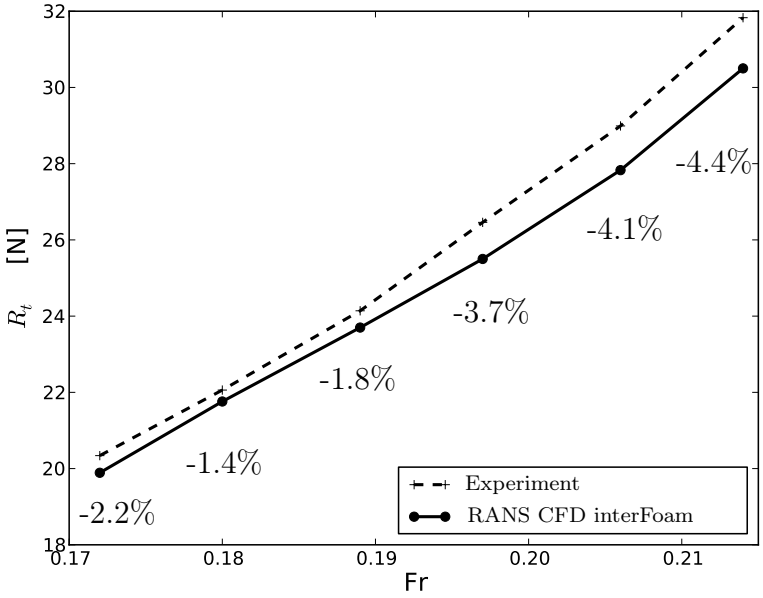

Figure 4.8.: Total resistance of the DTC hull; computed with free surface

$$c_f = \frac{0.075}{\left(\log_{10}\left(\mathrm{Re}\right) - 2\right)^2} \qquad (4.15)$$

$$c_f = \frac{R_f}{\frac{1}{2}\rho u^2 S} \qquad (4.16)$$

In order to compare the friction forces between a test model and a full scale ship the friction coefficient c_f can be used. There are two methods to compute c_f: If only the Reynolds number of the flow is known, the empirical equation (4.15) of the ITTC'57 correlation line [79] can be used. In the other case, if the viscous forces are known (from experiment or simulation), equation (4.16) can be used.

The results of the computations with `interFoam` are shown in Fig. 4.8. The plot shows the total friction resistance over the Froude number for the CFD and experimental results. In addition to the numerical values of the hull friction Fig. 4.9 shows the wave pattern generated by the ship hull at model scale and design speed.

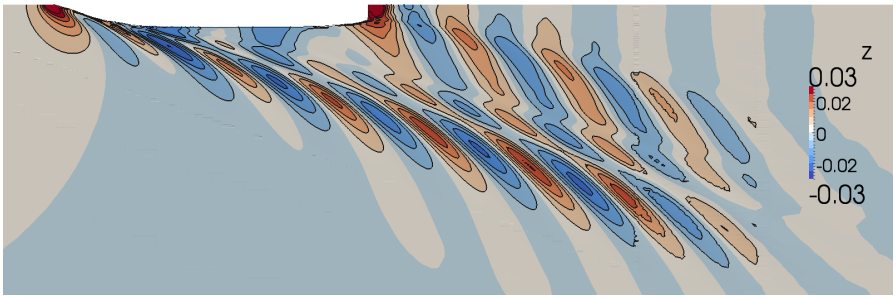

Figure 4.9.: Wave pattern around the DTC model ship at design speed

4.2.3. Inertia and Drag Coefficient of a Bilge Keel

After computing the viscous flow in a domain with fixed boundaries, the motion of the hull surface hast to be considered. In a first step the flow around a boundary surface that moves along a prescribed path is computed, before in the next section the coupled simulation of a free rolling ship is simulated.

The case study in this section is based on an article by Sarpkaya and O'Keefe [1] and was published in Piehl and el Moctar [3]. The authors conducted experiments with a bilge keel in an oscillation flow. In this, so called *forced motion* test a wall (bilge keel) moves along a prescribed path and the force acting on the wall surface can be used to determine the inertia and damping coefficients. The experimental results were used by Querard et al. [80] and Kinnas et al. [81] to validate their numerical methods.

The setup of the validation case in this section is based on the roll damping computations presented in Piehl et al. [7] and Piehl and el Moctar [6] and extends the investigation by comparing numerical and experimental results and the use of more advanced turbulence model (LES). For the prediction of the roll damping coefficient of bilge keels, simple formulas based on physical principles and tests may be used. To the last category belongs the well-known *Ikeda method* [41], [46] and[45]. Ikeda further developed the approach of Tanaka ([37],[38],[39] and [40]) to divide the roll damping coefficient into a sum of simple coefficients, each attributing to a different flow effect.

From his model experiments in [41] Ikeda derived an empirical equation for the drag coefficient of a bilge keel C_d:

$$C_d = 22.5 \frac{b_{\mathrm{BK}}}{\pi r_{\mathrm{BK}} \phi_A} + 2.4 \tag{4.17}$$

b_{BK} is the characteristic length of the bilge keel. r_{BK} is the distance to the center of rotation and ϕ_A is the amplitude of the roll motion.

$$F(t) = \rho C_m V \dot{u}(t) + \frac{1}{2}\rho C_d A u(t)|u(t)| \tag{4.18}$$

The Morison equation (4.18) models the forces on a body due to transient flow conditions. Eq. (4.18) states a general notation and Eq. (4.19) uses a formulation depending on a harmonic velocity oscillation $\cos\Theta$, .

In Eq. (4.19), the transient force $F(t)$ depends on the fluid density ρ, the flow velocity $u(t)$, the volume of the immersed body V, the projected area A in normal direction to the flow and the two inertia and drag coefficients C_m and C_d (Morison et al. [82]). The heuristic Morison equation forms the theoretical basis for another flow quantity, the Keulegan-Carpenter number K (4.22), which is a measure for the frequency dependence of the forces on a body (Keulegan and Carpenter [83], the authors use the term *period parameter* instead of K).

The same drag coefficient C_d as in Eq. (4.17) is used in Eq. (4.19) to compute the forces on a body in an oscillating flow.

$$\frac{2F}{\rho h w U_m^2} = -C_d \left|\cos\Theta\right| \cos\Theta + C_m \frac{\pi^2}{K} \tag{4.19}$$

In the similar equation (4.19), the force F consists of the sum of drag and inertia forces which depend on the fluid density ρ, the projected bilge keel area normal to the flow direction (the height h multiplied by the width w), the velocity U_m, the dimensionless time Θ in radian ($\Theta = 2\pi$ is one full cycle), the Keulegan-Carpenter number K and the two coefficients drag C_d and inertia C_m. Sarpkaya and O'Keefe [1] used the Morison equation (4.19) to derive an expression for the Fourier-averaged drag (4.20) and inertia coefficients (4.21).

$$C_d = -\frac{3}{4}\int_0^{2\pi} \frac{F_m \cos\Theta}{\rho h w U_m^2} d\Theta \tag{4.20}$$

$$C_m = \frac{2K}{\pi^3}\int_0^{2\pi} \frac{F_m \sin\Theta}{\rho h w U_m^2} d\Theta \tag{4.21}$$

The K-number (Keulegan and Carpenter 1958 [83]) used in Eq. (4.20) and (4.21) is a dimensionless flow quantity that sets the drag forces on a body into relation with the inertia forces. K (Eq. (4.22)) can be used in a similar manner like the Reynolds number Re or the Froude number Fr, but in order to compare oscillatory flows.

$$K = \frac{U_m T}{h} = \frac{2\pi A}{h} \tag{4.22}$$

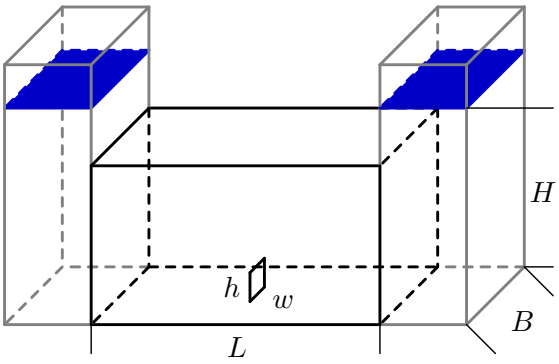

Figure 4.10.: Test tank geometry

The time period T is used to account for the oscillatory nature of the motion. The flow velocity U_m and the characteristic length h have the same meaning as in the definition of Re.

Sarpkaya and O'Keefe [1] used different experimental setup to measure the forces on a bilge keel than Keulegan and Carpenter 1958 [83]. Instead of prescribing roll motions of the ship model (Ikeda [41]), a test tank with a wall mounted bilge keel and oscillating flow conditions were used. The aim of the experiments was to study the influence of the K-number on the drag coefficient. In addition to the measured forces and the derived coefficients the authors give a detailed analysis of the vortex pattern around the bilge keel. The well documented experiments and the relative simple test setup make this test case suitable for validation purposes.

The original test setup ([1]) only allowed to measure the bilge keel damping for pure roll motions. In order to also investigate the influence of the ship speed, the boundary conditions were modified to included different inflow velocities.

Figure 4.10 shows the general configuration of Sarpkaya and O'Keefe [1] test setup. In the U-shaped tunnel with a rectangular cross section an oscillatory flow was generated by alternating air pressure on the water column in the left and right leg (gray lines). Three different plates mounted to the bottom wall and equipped with a force sensor were used. The dimensions of the inner part (black lines) of the test tank were given with the width $B = 0.94m$, the height $H = 1.420m$ and the length $L = 10.67m$. The three different bilge keel shapes were: a plate $h = 102mm$ high, spanning the whole width $w = B$, a square plate with $h = w = 102mm$ and smaller square plate with $h = w = 76mm$. The flow conditions were varied over a range of $K = 0.1 \ldots 100$, with a fixed Stokes parameter $\beta = \frac{Re}{K} = 1845$ for both $102mm$-plates and $\beta = 1035$ for the $76mm$-plate. The amplitude A of the oscillatory flow was $A = \frac{Kh}{2\pi}$, the time period was $T = \frac{h^2}{\nu\beta}$ and ν the viscosity of water. Using these two equations the time period was kept constant $T = 5.639s$ at

$h = 102mm$ and $T = 5.581s$ at $h = 76mm$ for all K-numbers, only the amplitude was varied.

In order to reduce the computational effort the domain was simplified to a brick-shaped geometry (only the black lines in Fig. 4.10). Although this approach neglects the influence of the flow around the upper tank corners it is a reasonable approach since these corners are over 50 times the bilge keel height apart from the bilge keel.

Figure 4.11 shows the mesh around the bilge keel. The control volumes near the plate are hexahedrons with an aspect ratio of one. Towards the outer boundaries the cell size was increased. The domain has a symmetry plane in the middle between the front and back wall, which only requires half of the domain to be meshed.

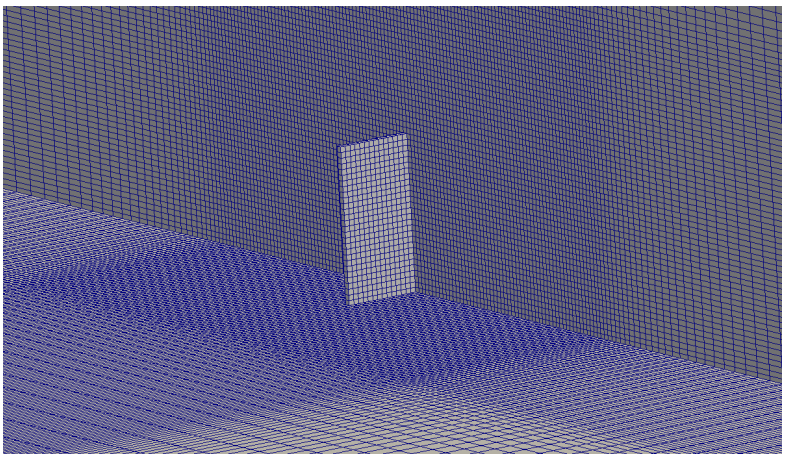

Figure 4.11.: Finite volume mesh

For the front and top walls a slip boundary condition was applied, the left and right wall were given periodic boundary conditions and for the bottom wall and the bilge keel had non-slip boundary condition with a wall function in the cases which used the RANS turbulence model. For the test with the rectangular plate ($h = B$) the setup was reduced to a two-dimensional setup with only $270 \cdot 10^3$ cells. In order to investigate the dependency of the drag and inertia coefficient on the K-number, K was systematically increased $K = [0.5, 1, 2, 5, 10, 20, 50]$. This K-range matches the values of K encountered in real ship-flow conditions, eg. a large container ship with a beam of $51m$, $14m$ draft and a bilge keel height of $0.5m$, that rolls with an amplitude of $5°$ has a K coefficient of about $K \approx 30$. The simulation cases were computed with the transient single-phase solver `pimpleDyMFoam`. This solver uses a PISO algorithm scheme with adaptive time stepping (time step limit

Courant number < 0.25). The oscillatory flow conditions were generated with an oscillating volume force acting on the whole fluid domain.

All simulations were performed with the RANS kωSST turbulence model with wall functions for the turbulent boundary layer. The three dimensional setup with the $102mm$ bilge keel were additional simulations using a LES turbulence model, a RANS kkL ω low Reynolds model and RANS k-ω SST model with wall functions conducted. The 3D mesh for the RANS computations consisted of $1.0 \ldots 1.5 \cdot 10^6$ cells while the LES-mesh had $2.8 \cdot 10^6$ cells (near the bilge keel, the cell size was within the recommend size for LES).

The low-Reynolds turbulence model was used in order to resolve the turbulent boundary layer and the transition from laminar to turbulent boundary layer. These simulations had to be discarded because the computational demand became too high. The small prism layer cells increased the mesh size and required too small time steps. However, up to the time the low-Re simulations were stopped, the time series of the bilge keel forces were close to the values of the RANS simulations with a wall function.

To investigate the influence of the forward speed on the drag and inertia coefficients, additional 3D computations were performed. The meshes for these cases are created without a symmetry plane and have a longer outflow region toward the back wall. At the front wall an inlet velocity in the range of $U_{in} =$ [0.0, 0.001, 0.002, 0.005, 0.01, 0.02, 0.05, 0.1, 0.2] m/s was applied. These parameter variations were repeated for $K = 1$ and $K = 10$.

Every simulation started impulsively and ran for 10 motion cycles. Figure 4.12 shows the position and the speed of the bilge keel and the time-dependent force over one period. The force was averaged over the last three motion cycles. Prior to the calculation of the drag and inertia coefficients the time series was re-sampled with a uniform time step size. The integral terms in Eq. (4.20) and (4.21) represent a convolution integral of the force with the velocity and the acceleration.

Figure 4.13 and 4.14 show the numerical and experimental results.The principle behavior of the drag coefficient is characterized by a decrease of the value toward higher K-numbers. The inertia coefficients show an inverse behavior, the value increases with increasing K. In general the drag C_d and inertia C_m coefficients agree well.

Another distinct feature in both figures are the overall higher values of the coefficients for the rectangular plate. This behavior can be explained with a blockage effect occurring in 2D or quasi-2D simulations and experiments, which leads to higher forces.The falling or rising slope of both plots show a slight bump near $K = 8$. This feature may indicate a resonance effect or could be attributed to a change in the topology of the vortex pattern around the bilge keel.

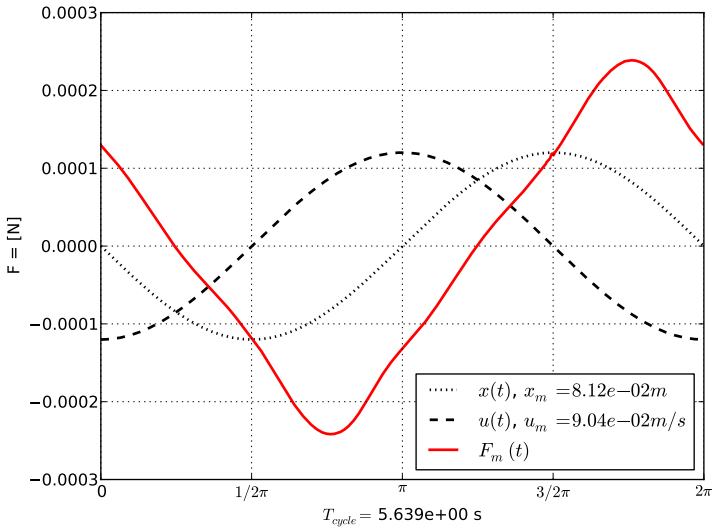

Figure 4.12.: Time series of the position, velocity and force of the 76mm bilge keel at K=5

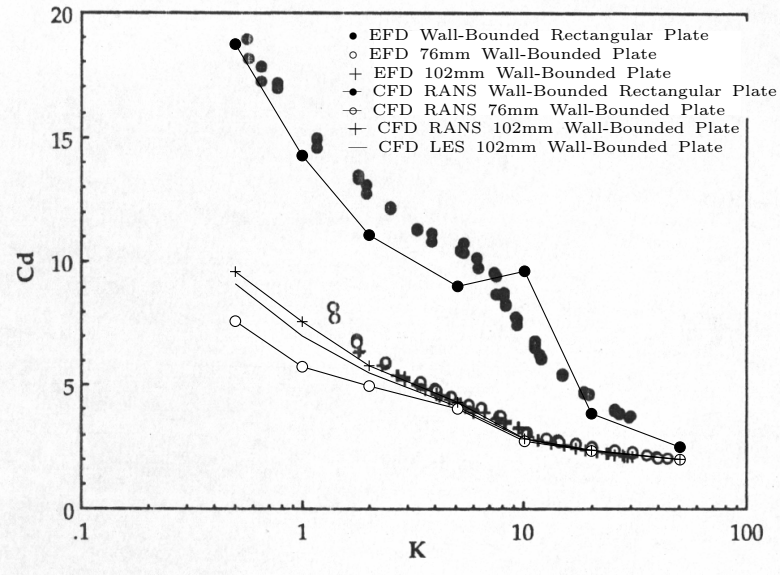

Figure 4.13.: Drag coefficient over K-number; EFD and CFD results for rectangular plate, 76mm plate and 102mm plate; Sarpkaya and O'Keefe [1]

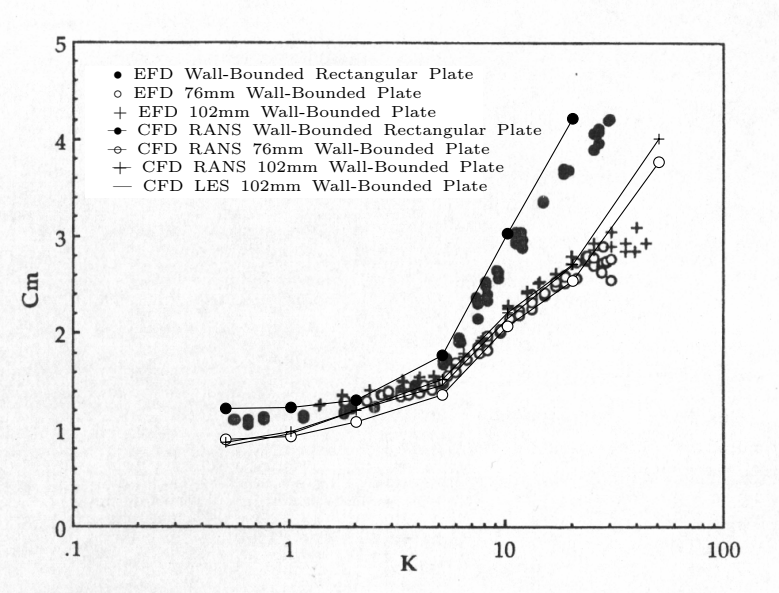

Figure 4.14.: Inertia coefficient over K-number; EFD and CDD results for rectangular plate, 76mm plate and 102mm plate; Sarpkaya and O'Keefe [1]

A significant deviation of the CFD results from the measurements can be seen in Fig. 4.13. The slope of the computed drag coefficient for the rectangular plate is larger compared to the measured one. This may be due to the 2D effects. The results from both 76mm and 102mm square plates compared to each other confirm the observation of Sarpkaya and O'Keefe, that the coefficients do not depend on the size of the plate and that the force has a linear dependency on the bilge keel area. The plots include the results of the computations with the LES turbulence model. The values of the coefficients – which were obtained by integration over a full cycle – differ only slightly from the computations with the RANS kωSST. An analysis of the force time series revealed that the forces in the LES simulation show a strong fluctuation within a cycle, as well as from cycle to cycle.

This effect becomes more evident when comparing the vorticity strength of RANS and LES simulations. In Fig. 4.15 the vorticity structure around the oscillating square plate is shown. The figure shows the RANS (top) and LES (bottom) flow state, using the iso-surface (yellow) of the same vorticity magnitude at the same moment in an oscillation cycle. As expected the computed LES vortex pattern is much more complex and has a finer structure. Reviewing the transient behavior also shows that the vortices are longer-lived.

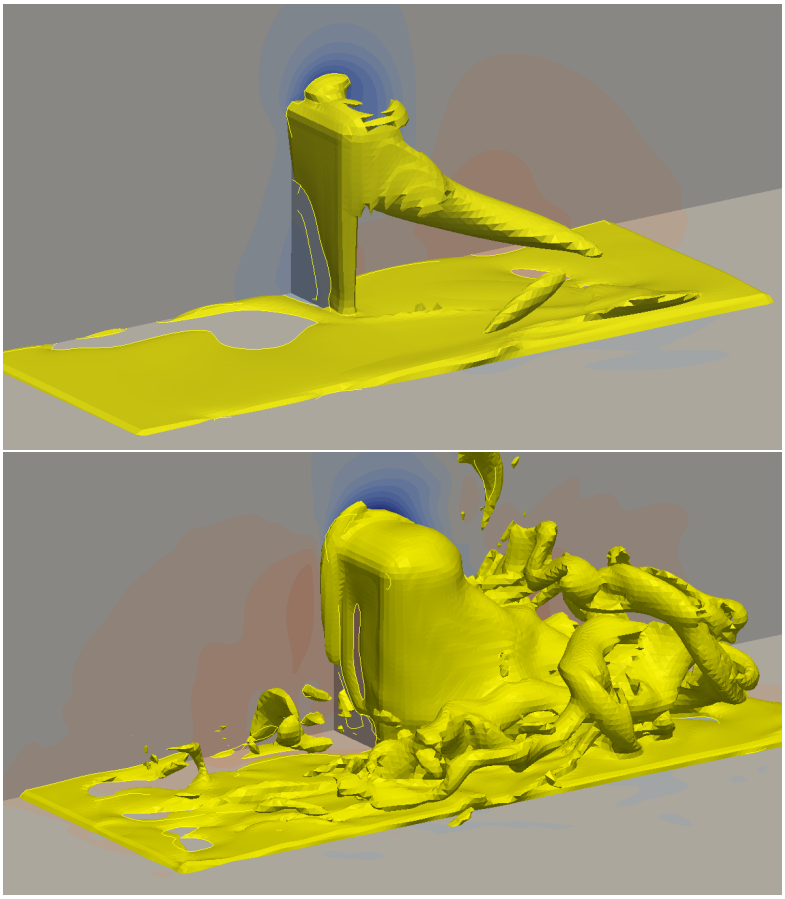

Figure 4.15.: Iso-vorticity surface at K=5; Top RANS; bottom LES

It is Interesting, that the LES solver produces such fine turbulence structure on a mesh with only slightly smaller cells. Another interesting feature is the fact that both methods produce nearly the same results for the drag and inertia coefficients.

Figure 4.16 shows the pressure distribution on the left and right side of the rectangular plate (2D). The figure shows the high pressure in front of the bilge keel at the moment of the maximal acceleration. The low pressure area on the left side is smaller but more evenly distributed along the height of the bilge keel. Low pressure cores of the vortices that are shed from the tip can be seen at the top of the bilge keel. In each half cycle a counter rotating vortex is separated from the tip and moves upwards.

Sarpkaya and O'Keefe also discussed the dependency of the vortex pattern on the K-number. Figure 4.17 and 4.18 show the velocity field near the rectangular plate at different positions in the motion cycle for $K = 1$ and $K = 5$. The cases

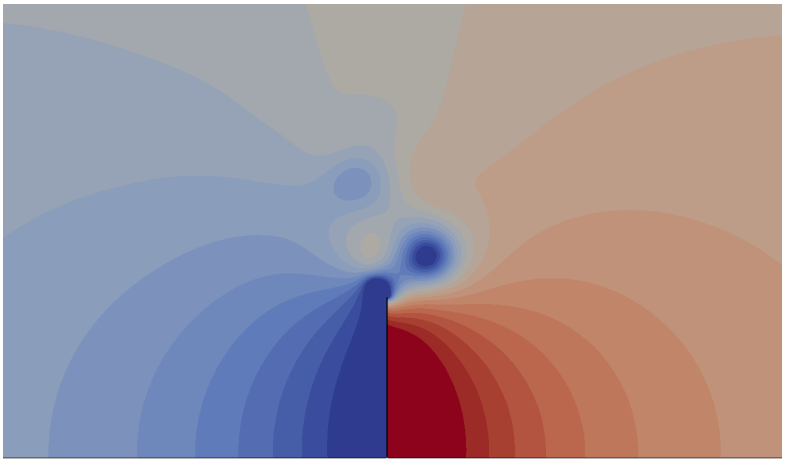

Figure 4.16.: Pressure field computed with RANS-CFD; rectangular plate with K=1; moving to the right

were computed with the RANS turbulence model. Compared to the figures shown in Sarpkaya and O'Keefe [1], the vortices show in general the same motion path. However they dissipate much faster, move more slowly and vortex pairs interact less with each other. Another effect that can be observed in the results of the 3D RANS simulation is that the vortex sheet, that is shed from the tip of the bilge keel, is stable for a long time, while the vortex sheet in the LES simulation breaks up into smaller vortices.

In addition to the simulation of the drag and inertia coefficients of a moving bilge keel in calm water, the influence of forward speed was investigated. Figure 4.19 and 4.20 show the drag and inertia coefficients over the inflow velocity for $K = 1$ and $K = 10$. The simulations were conducted for the larger 102mm square plate and the results showed the expected trend.

In spite of the larger computational domain the coefficients for the inflow velocity U_{in} stayed the same. An increase of the forward speed show a distinct increase of C_d and a decrease of C_m for a K-number over a certain threshold. This behavior is in accordance with the increasing roll damping coefficient of the bilge keel component in the Ikeda method due to forward velocity. For the determination of the drag and inertia coefficients both RANS and LES turbulence model are suitable. As expected the LES model represents the vortex behavior much better. The results of RANS and LES are expected to differ more significantly if the flow conditions become more severe.

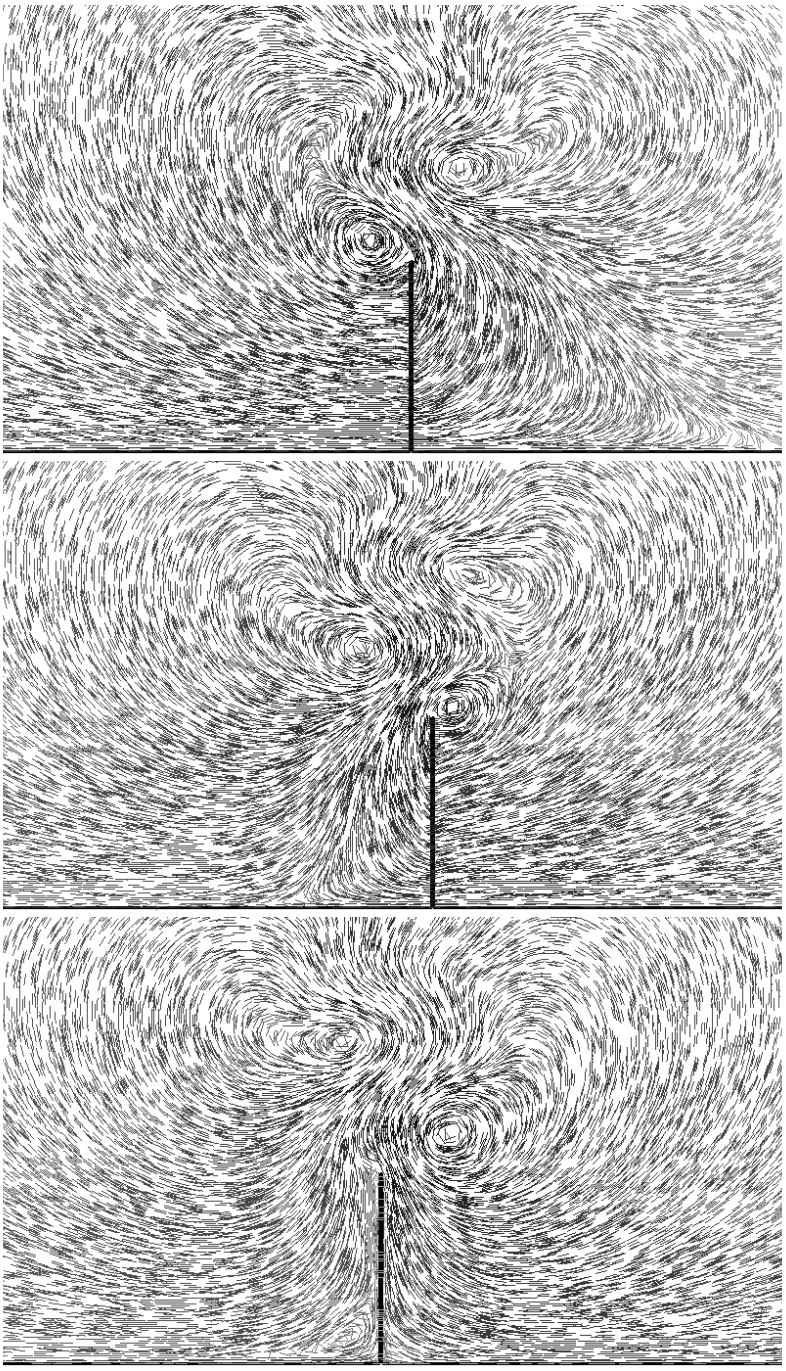

Figure 4.17.: Computed 2D RANS flow field with vortex pattern; rectangular plate at K=1; from top to bottom $\Theta = 0\pi$, $\Theta = 1/4\pi$, $\Theta = 3/2\pi$

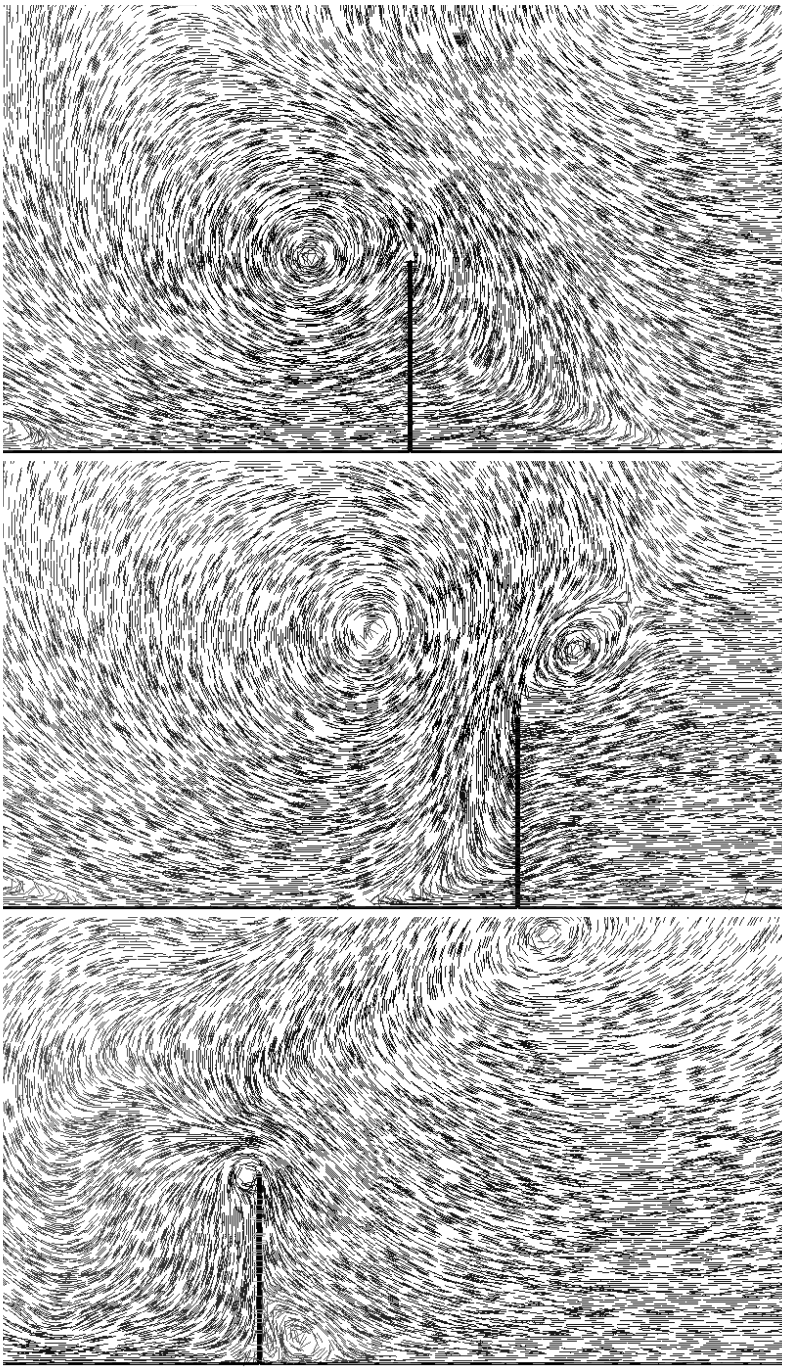

Figure 4.18.: Computed 2D RANS flow field with vortex pattern; rectangular plate at K=5; from top to bottom $\Theta = 0\pi$, $\Theta = 1/4\pi$, $\Theta = 3/2\pi$

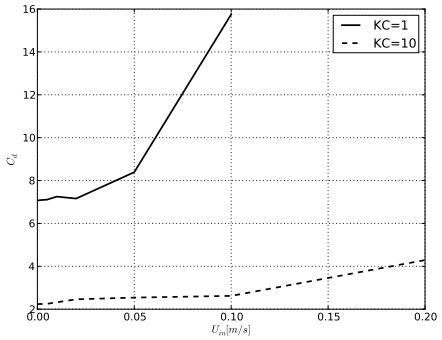

Figure 4.19.: Drag coefficient over forward velocity; square plate 102mm

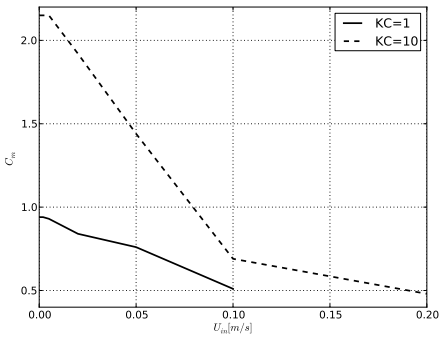

Figure 4.20.: Inertia coefficient over forward velocity; square plate 102mm

The results obtained by LES and RANS may also differ for long or multiple bilge keels in forward flow condition. In that case the different vortex diffusivity may influence the bilge keel interaction with vortices transported downstream.

The results of the CFD simulations clearly support what Sarpkaya and O'Keefe suggested in their article. The unsymmetrical vortex pattern (memory effect) originate from the initial phase at the beginning of the experiment or the numerical simulation. Oscillation motion of bilge keels with a small amplitude shed every half cycle a counter rotating vortex from the tip of the plate. These vortices attach to each other and move away from the bilge keel. At larger amplitudes the shedded vortices stay near the bilge keel and the bottom wall. For both high frequency and low amplitude motions the bilge keel may generate a large vortex on the left or right of the tip which is fed each cycle by a small vortex shed from the bilge keel.

4.2.4. Roll Decay Test (1 DOF)

To investigate the ability of OpenFOAM to compute coupled fluid-rigid body interaction the roll decay test was chosen. In the following two section the results of two different roll decay models test are used to validate OpenFOAM. In this section, the one degree of freedom roll decay test of *Gothenburg Workshop 2010* presented by Irvine [43] is analyzed and compared with to OpenFOAM. In the next, a similar study is conducted with the six degree of freedom model test of the Hamburg Ship Model Basin (HSVA) [65].

The *Gothenburg* roll decay test case was computed with the in-house OpenFOAM extensions `shipMesh` (mesh generation) and `sixDofFoamGL` (solver) provided by el Moctar et al. [84] and Oberhagemann and el Moctar [85]. The test

condition used for the case setup are listed in Tab. 4.5 and a description of the test procedure and the results were obtained from Irvine [43].

Table 4.5.: Case data Gothenburg roll decay test

hull	DTMB5415 with bilge keel		
scale	λ	$1:46.6$	$[-]$
length	L_{PP}	3.048	$[m]$
draft	T	0.214	$[m]$
beam	B	0.386	$[m]$
displacement	∇	0.083588	$[m^3]$
center of gravity	KG	0.163	$[m]$
wetted surface	S_{wet}	1.371	$[m^2]$
radius of inertia	$[k_{\mathrm{xx}}, k_{\mathrm{yy}}, k_{\mathrm{zz}}]$	[1.915, 48.532, 48.532]	$[m]$
velocity	u	0.7546	$[m/s]$
Froude number	Fr	0.138	$[-]$
roll amplitude	ϕ_A	10	$[^\circ]$
fluid density	ρ	998.8	$[kg/m^3]$
dyn. viscosity	ν	$1.09 \cdot 10^{-6}$	$[m2/s]$
turb. kin. energy	k	$5.4 \cdot 10^{-3}$	$[m^2/s^2]$
turb. frequency	ω	10	$[s^{-1}]$

Figure 4.21 shows the side view of the the well-known Arleigh Burke class naval vessel (hull shape type DTMB5415). Except for the bilge keel, the hull has no further appendages. Aside from the moderate initial roll angle $\phi_A = 10^\circ$ the most noteworthy feature of the test setup is that all other degrees of freedom – except the roll axis – are fixed. The position of the roll axis is on the center plane at the height of the center of gravity.

Figure 4.21.: Hull shape of the Arleigh Burke class naval vessel

The mesh around the DTMB5415 hull was generated in a similar way as shown in Fig. 4.25. The mesh was refined in such a way that the cells in the region of the free surface suffer the least distortion from the mesh morphing routine.

The numerical simulation follows the same procedure as the roll decay model tests: The hull is inclined to the initial roll angle and accelerated to test velocity. At the beginning of the measurement the ship is released and starts an oscillating roll motion. The two roll angle time series shown in Fig. 4.22 allow a comparison between the experimental fluid dynamics (EFD) and the numerical results (CFD). The plot shows a good agreement of the roll period and only a slight shift of the phase angle. The roll angle maxima also achieve a good match the test results. The decaying roll angle amplitude shows the expected logarithmic trend with a constant damping coefficient.

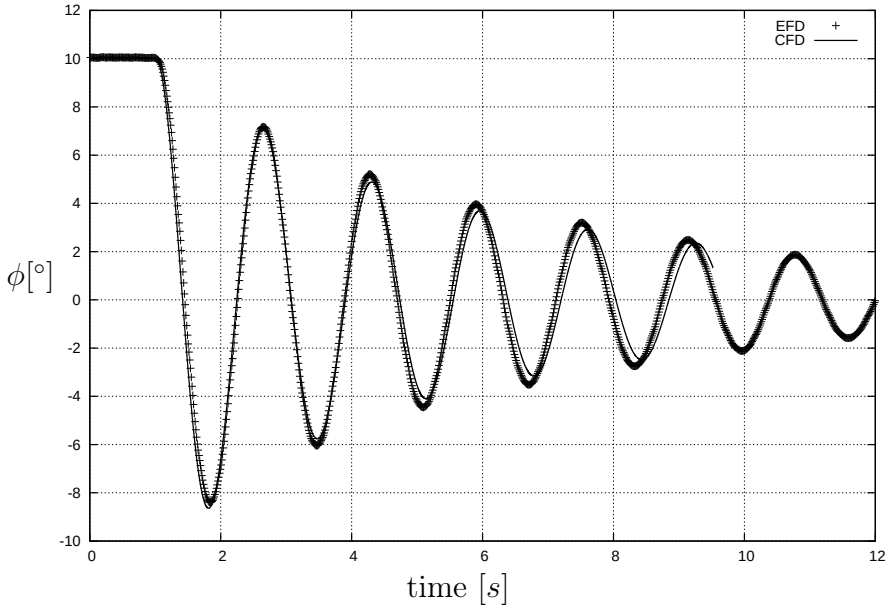

Figure 4.22.: Gothenburg roll decay test, comparison between model test and OpenFOAM-GL

The matching plots in Fig. 4.22 show the ability of OpenFOAM to compute the roll decay motion of a ship hull. It should be noted that the solver required a very small time step size and that a force relaxation of the fluid - rigid body coupling had to be applied in order to keep the solution stable. A further numerical instability arose in the computation of the alpha field when high flow velocities occurred near sharp edges.

4.2.5. Roll Decay Test (6 DOF)

The Hamburg Ship Model Basin (HSVA) conducted roll damping tests with a $\lambda = 59.407$ scale model of the Duisburg Test Case (DTC) hull. The experiments

documented in the test report ([65]) included roll decay tests as well as forced moment tests. The simulation of the free roll decay tests were first conducted with the `sixDofInterFoamGL` solver and repeated later with the standard OpenFOAM solver `interDyMFoam` (version 2.1.1) (see Piehl and el Moctar [5]).

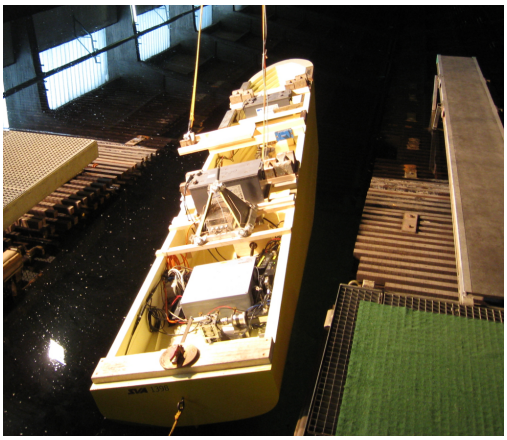

Figure 4.23.: DTC ship model at the model test basin HSVA

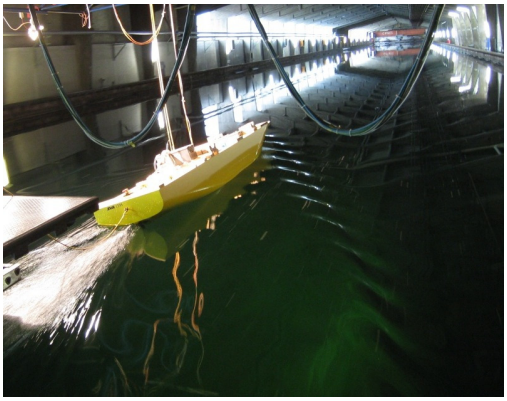

Figure 4.24.: Inclined ship hull at $U = 1.47\,\mathrm{m/s}$

Figure 4.23 and 4.24 show the model scale ship in the test tank prior and during the roll decay tests. The hull is equipped with an optical 3D measurement system and electric drives for propulsion and steering. The steering is controlled via autopilot which allows the ship to move along a straight course even when rolling with large amplitudes. In both figures the model ship can be seen inclined to port side by a weight on a cantilever beam. The test procedures are the same as in the previous section: the ship is accelerated to the test velocity and when the weight is removed the hull starts to roll.

The roll decay test was conducted for two load conditions which correlate to the full scale drafts of $D = 12m$ and $D = 14m$. Table 4.6 lists the hull parameter and load condition for both drafts. The roll decay tests were conducted twice for each load case and three different ship speeds $U = 0.0, 0.8, 1.47\,\mathrm{m/s}$. Figure 3.5 in the section about time series analysis (Sec. 3.2) shows the measured results of the time-dependent roll angle for $T = 12m$ and $U = 1.47m/s$.

The mesh shown in Fig. 4.25 was generated with `shipMesher`, the hull is equipped with bilge keel and rudder (fixed forward position), but without a propeller. A distinctive feature of the `sixDofInterFoamGL` solver is the use of a blending function for the mesh motion. This function allows a rolling of the ship hull without deforming the cells near the hull surface, thereby preventing a deterioration of the stability due to distorted prism layer cells.

Table 4.6.: Roll decay tests for DTC model ship

		$D = 12m$	$D = 14m$	
length between perpendiculars	L_{PP}	5.970	5.970	$[m]$
draft	D	0.2018	0.2354	$[m]$
displacement	∇	0.6496	0.7887	$[m^3]$
block coefficient	C_B	0.6288	0.6544	$[-]$
metacentric height over base line	KM	0.4363	0.4213	$[m]$
metacentric height	GM_T	0.0768	0.0230	$[m]$
longitudinal center of gravity	LCB	2.9707	2.939	$[m]$
center of gravity over base line	KG	0.3595	0.3983	$[m]$
mean roll axis	RA	0.352	0.378	$[m]$
moment of inertia	i_{xx}	0.326	0.340	$[m]$

Table 4.7.: Roll period in seconds and the deviation (%) from the experimental results; draft T=12m and T=14m

$U = [\frac{m}{s}]$	$T = 12m$		$T = 14m$	
0.0	2.6s	(1.7%)	4.64s	(6.8%)
0.8	2.53s	(4.2%)	4.70s	(2.3%)
1.47	2.5s	(−2.2%)	4.33s	(2.4%)

The results listed in Tab. 4.7 were computed by applying the time series analysis method described in Sec. 3.2 (see Fig. 3.5 and Fig. 3.9 for the roll decay time series) and show the roll period of the simulated time series and the deviation from the experimental results. While for the roll period the results have a good agreement, the linear roll damping coefficients deviate up to ±50%. The analysis of higher order damping model showed similar deviations. Compared to the Gothenburg results in the previous section, these large deviation can be attributed to several factors: In contrast to the roll decay test with only one degree of freedom, the current experiment allowed free motion in all directions. During the roll decay test at the highest ship speed a strong yawing motion could be observed. This effect – induced from large rudder motion – caused the large damping coefficient in the experimental results. The simulation on the other hand had a fixed rudder which resulted in a significant smaller roll damping (this effect is also described in

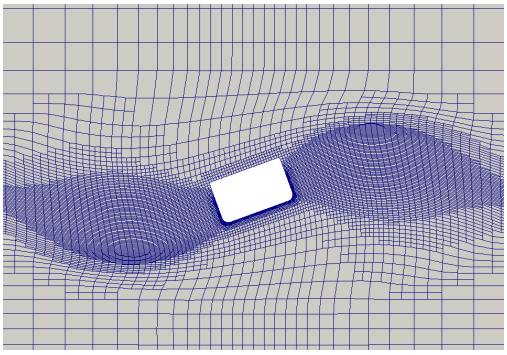

Figure 4.25.: Mesh around inclined DTC cross section; mesh motion with blending function

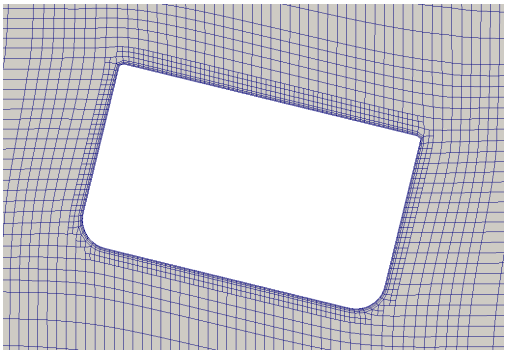

Figure 4.26.: Mesh detail around cross section; mesh motion with grid elasticity

el Moctar et al. [10]). With the publication of OpenFOAM 2.1.1 the roll decay simulations were repeated with the standard multiphase solver `interDyMFoam`. This solver works in a similar way, but uses a different mesh deformation method. Here the grid points of the mesh are not moved according to a blending function, but by solving the Laplace equation for a elastic mesh and a displacement of the grid points on the hull boundary (Fig. 4.26). In addition to the standard solver, the mesh was also generated with `blockMesh` and `snappyHexMesh`, controlled by a specially tailored python program.

In order to record the roll angle of the ship motion (position and velocity in three dimensions) in a format usable in the time series analysis, the OpenFOAM solver had to be modified. In the standard version of the motion solver the rotation of the rigid body is only present in form of a rotation matrix. To export the motion state in the correct format the solver was extended with a method that transforms a rotation matrix into Euler angles. The fluid - rigid body interaction algorithm in `interDyMFoam` uses a so called *weak* or *staggered* coupling. This method computes the fluid flow and rigid body motion only once during a time step. This explicit method may generate strong pressure oscillation on the interface between fluid and rigid body, causing the simulation to crash. This effect can be mitigated by using a smaller time step size.

In order to stabilize to roll decay motion a different approach was chosen: The `interDyMFoam` solver was modified with a multi-level force under-relaxation scheme which successfully suppresses the pressure oscillations. A more detailed description of the problem and the implemented solver modifications can be found in Piehl and el Moctar [5].

4.3. Forced Roll Motion

The *forced motion* test is – aside from *roll decay* and *restrained forced moments* (see [35]) – a third test method that can be used to determine the roll damping coefficients of a ship hull. This type of test has the advantage that the input variable (roll angle) and the constant test parameter (roll period, roll amplitude, roll axis) can be controlled precisely and that the reaction moment can be measured in a fairly straightforward manner.

Simulating a forced roll motion has another advantage over simulations accounting for the free roll decay: Only the unsteady RANS and VOF equations are solved. Since the motion of the hull is predefined, neither a fluid-body interaction routine nor a rigid body motion equation has to be implemented into the solving process.

4.3.1. 2D Test Cases

The simulation of a roll damping test requires several model assumptions. The first and major constraint is the use of a two-dimensional mesh. This means that turbulent effects and vortex transport are at least questionable. Furthermore the 2D setup does not allow a forward ship speed, hence all simulations are done with zero ship speed.

The base shape of the hull is a quadratic box, with its bearing located in the center of the box, that in turn is fixed at the height of the initially undisturbed free surface. The hull has a design edge length of 20 m and is simulated at a model scale of $\lambda = 20$. During the test procedure, the hull oscillates around a fixed roll axis and the reaction moment generated by fluid forces is sampled. The ship hull is assumed to be a rigid body, moving according to a prescribed motion. The motion is defined by its position and velocity.

Since all three degrees of freedom, except for the rotation are fixed, the equation of motion is reduced to one dimension. The forced roll motion can be defined by a simple sinusoidal function (4.23), that solely depends on the maximal roll angle $\phi_A = 10\,^\circ$ and the angular frequency $\omega = 2\pi/T_{\text{roll}}$ with $T_{\text{roll}} = 5\,\text{s}$:

$$\phi(t) = \phi_A \sin(\omega t) \frac{1}{1 + e^{-\kappa(t-t_0)}} \tag{4.23}$$

$$\dot{\phi}(t) = \phi_A \left[\frac{\omega \cos(\omega t)}{1 + e^{-\kappa(t-t_0)}} + \frac{-\kappa \sin(\omega t) \left(e^{-\kappa(t-t_0)}\right)}{\left(1 + e^{-\kappa(t-t_0)}\right)^2} \right] \tag{4.24}$$

For stability reasons during the initial simulation phase, a sigmoid function is used to successively blend the sinus function to its full extent (Eq. (4.23)). The blending time and rate can be configured by a rise time t_0 and slope κ. To fully define the

motion state $(\phi, \dot{\phi})$, a function for the roll angle velocity $\dot{\phi}$ is also needed (Eq. (4.24)). The resulting time series of both equations (4.23) and (4.24) is shown in figure 4.31.

By varying the hull shape systematically, the influence of the hull shape on the damping behavior can be investigated. In a first step, the dimensions of the geometry are defined. Depending on these measures, the vertices are generated accordingly and are connected either by straight lines or bezier splines. To obtain a surface rather than a line, these 2D line segments are finally extruded into the third dimension and tessellated with triangles.

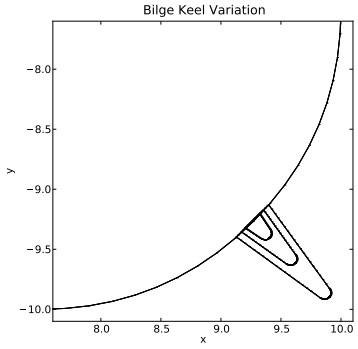

Figure 4.27.: Variation of the bilge keel height

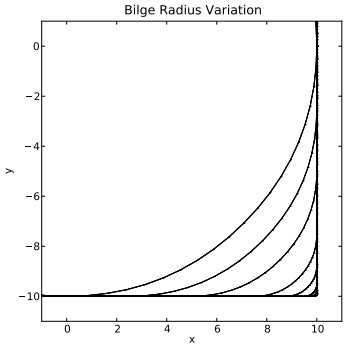

Figure 4.28.: Variation of the bilge radius

The outlines of the lower right bilge radii for all variations are shown in Fig. 4.28. The bilge radius was variated from $r_b = 10\,\mathrm{m}$ (perfect circle) down to $r_b = 0\,\mathrm{m}$ (quadratic box). In a second sequence, a bilge keel was introduced and attached to the hull with a constant bilge radius of $r_b = 2.5\,\mathrm{m}$. The length of the bilge keel l_b was variated in nine steps between 0.1 m and 0.9 m. Fig. 4.27 shows the hull with three different bilge keel lengths.

The computational domain has transverse length of 8B, a vertical height of 6B, a thickness of 1 m and consists of roughly 150 000 cells. The majority of the cells is located around the hull as well as around the free surface area and the bilge keels (see Fig. 4.29 and Fig. 4.30).

The used solver is derived from the OpenFOAM solver `interDyMFoam`, that solves the unsteady RANS equations for a two phase flow on a deforming mesh. The motion of the hull is prescribed by Eq. (4.23) and implemented as a rigid body motion. In order to realize the motion of the hull, a mesh morphing algorithm is employed. To ensure a sufficiently high cell quality near the hull, even at large displacements, a blending function is used. In principle, this function is a radial basis function and defines if and how the nodes are moved. Near the hull, all nodes are moved according to the motion of the hull. At the outer boundaries, all

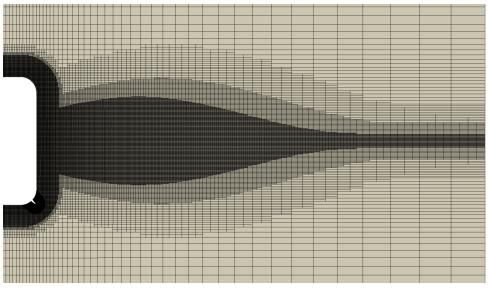

Figure 4.29.: Mesh refinement for resolving free surface with a deforming mesh

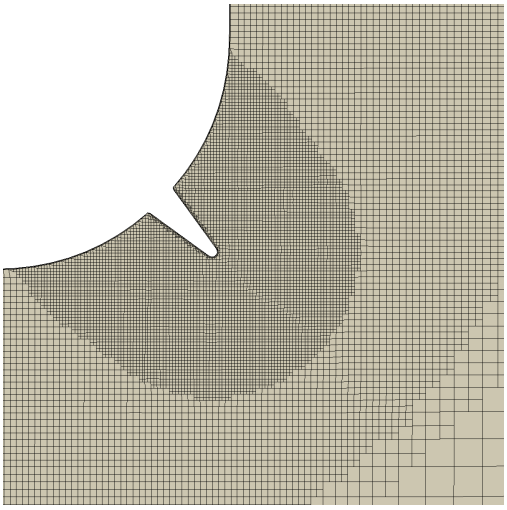

Figure 4.30.: Mesh refinement zone around bilge keel

points are fixed in space and in between these regions, the nodes are displaced to compensate the hull motion. During the simulation, the motion of the rigid body (roll angle Eq. (4.23) and angular velocity Eq. (4.24)) induces a reaction moment of the surrounding fluid.

Figure 4.31 shows the time series for roll angle, roll velocity and roll moment. The increasing amplitude during the first seconds of simulation is the result of the sigmoid blending function. For the analysis of the damping coefficients, the first two roll periods are omitted, in order to only include the roll periods where a harmonic state is reached. For the determination of the inertia and roll damping coefficient the time series analysis procedure described in section 3.3 was used.

Figure 4.32 and 4.33 show the linear inertia and damping coefficients δ_0, resulting from the time series analysis. The coefficients are plotted over the parameter of the shape variations of the bilge radius and the bilge keel length. The results show the expected damping behavior and confirm that smaller bilge radii and longer bilge keels generate larger damping coefficients (note that in Fig. 4.33, the plot range for the bilge radius is reversed). The coefficient calculated for the rolling hull with the perfect circular shape show nearly zero inertial effects as one would expect. It can be observed, that increasing the bilge keel length results in a strongly non-linear increase of the damping coefficient.

Two additional effects can be observed: First, an increase of the bilge keel length is more effective than the variation of the bilge radius. And second, the bilge keel must have a certain length to become effective. Otherwise a shadowing effect of the bilge radius suppresses the damping effect of the bilge keel. Another influence

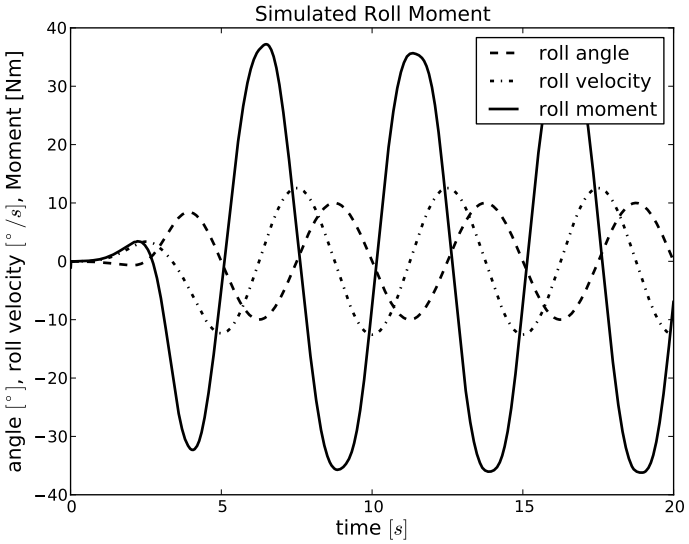

Figure 4.31.: Roll angle, roll velocity and resulting moment with ramp function

might be the thickness of the boundary layer, that is larger than the bilge keel height.

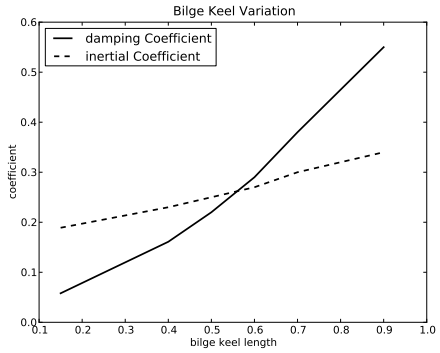

Figure 4.32.: Damping and inertia over bilge keel height

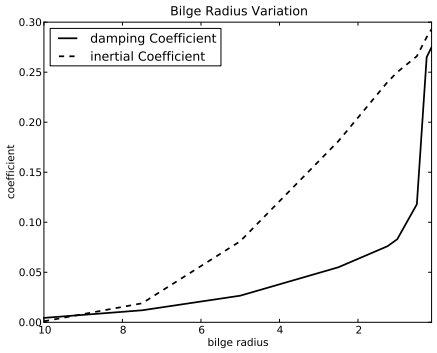

Figure 4.33.: Damping and inertia over bilge radius

In order to investigate the reason for the different damping coefficients B, a plot of the reaction moment over the simulation time is shown in figure 4.34. The data is obtained from simulations of all bilge keels, attached to a hull with a bilge radius of 2.5 m. It can be concluded, that the higher damping coefficients are not due to a higher maximal moment but from a similar moment that lasts for a longer time (see Fig. 4.34).

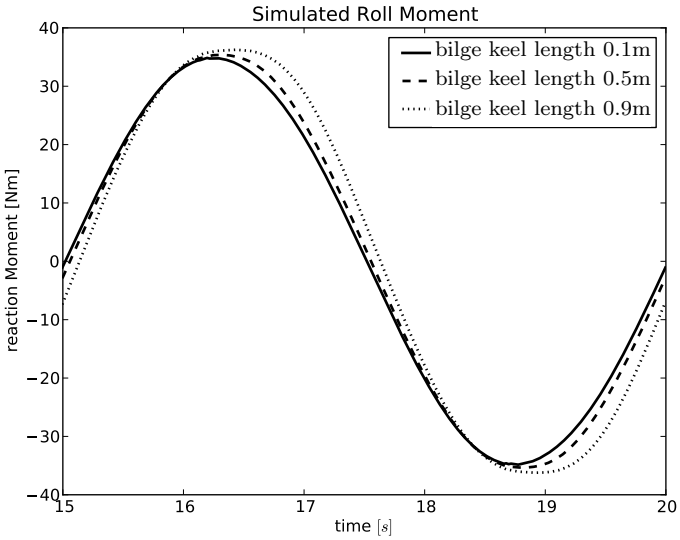

Figure 4.34.: Roll moment for various bilge keel lengths

Figure 4.35 shows the difference between the *simulated* time series M_{sim} from the CFD results and a *synthesized* time series M_{syn} computed with the Eq. (3.25) and the coefficients derived from the time series analysis. The difference between the synthesized and simulated roll moment $M_{\text{syn}} - M_{\text{sim}} = M_{\text{err}}$ has the shape of a 2nd harmonic mode which can be correlated to a ϕ^3 term commonly used in nonlinear roll damping equations (see Sec. 3.3.2). In comparison to the RANS simulation, the linear damping equation (3.25) leads to an overestimation of the maximum damping moment and a small underestimation of the damping moment's broadness. The simulations showed that the effect of a smaller bilge keel radius is not as significant as a longer bilge keel is. A longer bilge keel does not increase the maximum reaction moment, but creates a prolonged moment plateau.

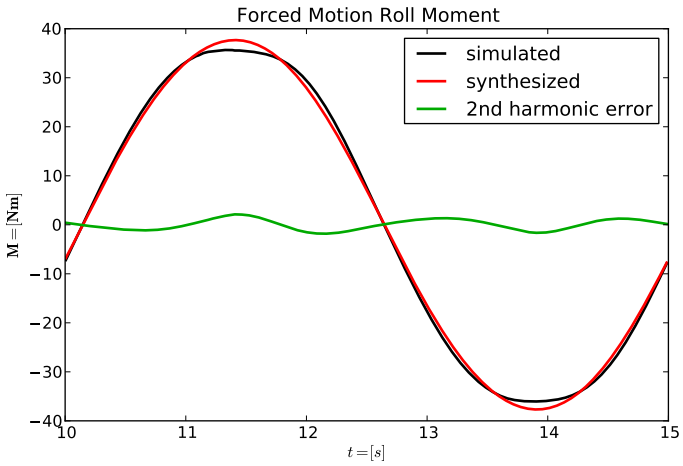

Figure 4.35.: 2nd harmonic mode indicates higher order damping term

L-shape Bilge Keel and High Resolution Grid

In addition to the hull shapes defined for the systematic parameter variation, some simulations were repeated with a L-shaped stiffening at the bilge keel tip (Holland profile). The geometry of these bilge keels was generated with the same way as before (Sec. A.5) but with the sharp edges instead of the smoothed bilge keel used in the case study on vortex separation from bilge keels in Sec. 4.3.2. Figure 4.36 shows the velocity vector of the flow around the bilge keel at different times in the roll cycle. The sharp edges of the bilge keel lead to a similar pattern of the vortex shedding as for the simple straight tip shapes (see Fig. 4.49 and Fig. 4.50). The time history of the pressure force is also similar for both tip shapes.

Figures 4.37 and 4.38 show the velocity magnitude and vorticity strength around a hull cross section, which were computed using the LES turbulence model. Each of the images show the hull at the same time, when $\phi(t) = 0$. Normally the LES model should not be used for 2D simulations, because the turbulence formulation requires a third dimension to model the vortex direction correctly. Also, the 2D vortex behavior differs from their motion in 3D, because vortex stretching and the twisting of two vortices does not occur. Furthermore, the diffusion of a vortex is weaker in 2D. Still, the LES model and the high resolution of the mesh allows to visualize the periodically recurring vortex pattern (see the locations of the vortices in the sequence of roll cycles in Fig. 4.38) much better than RANS (at a higher computational cost).

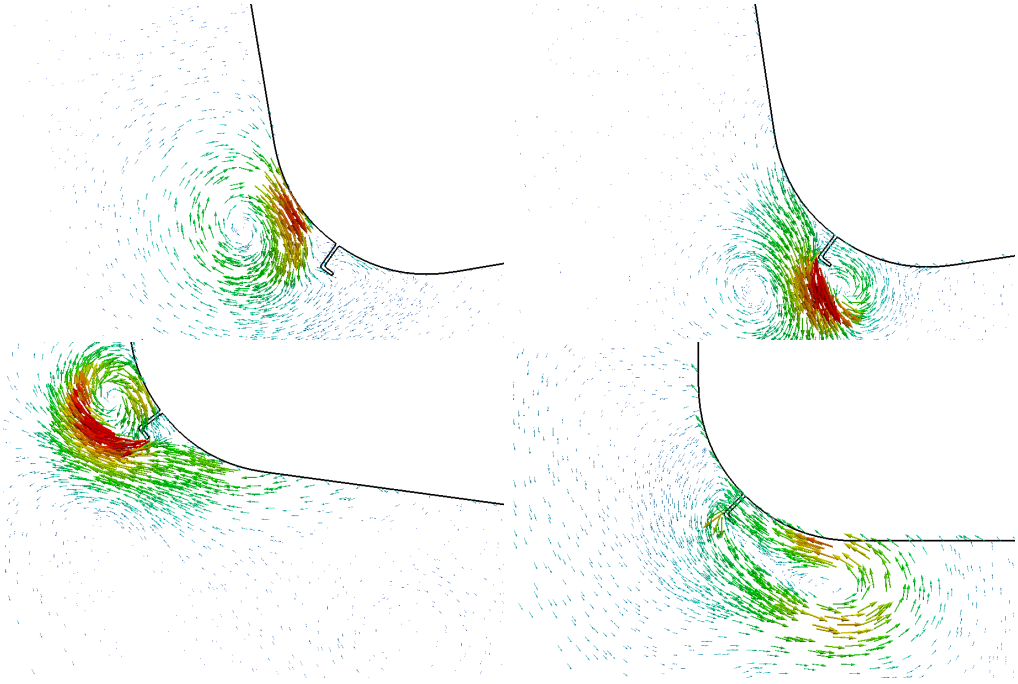

Figure 4.36.: Vortex shedding at the L-shaped bilge keel; RANS simulation

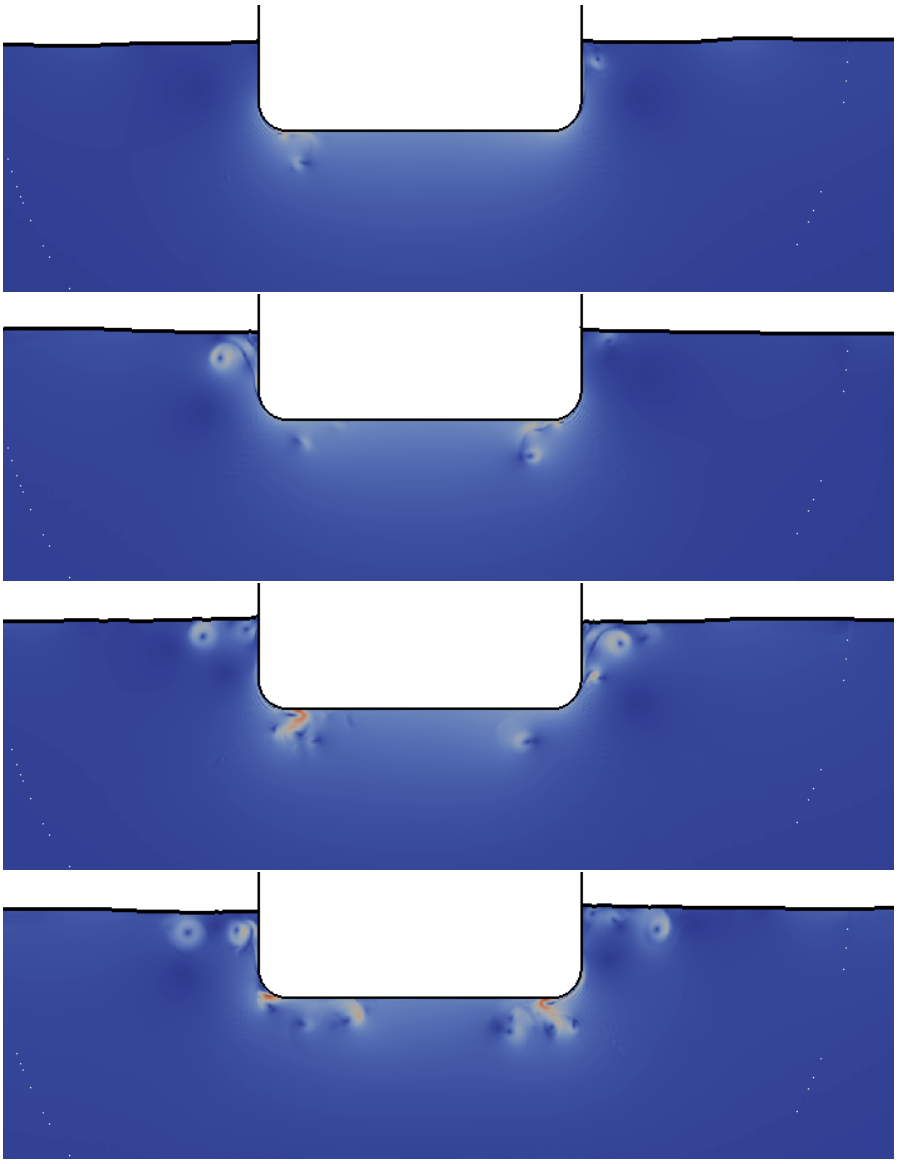

Figure 4.37.: Vortex shedding at the main section without bilge keel; velocity magnitude at the beginning of the roll cycle 2,3,4,5; LES simulation

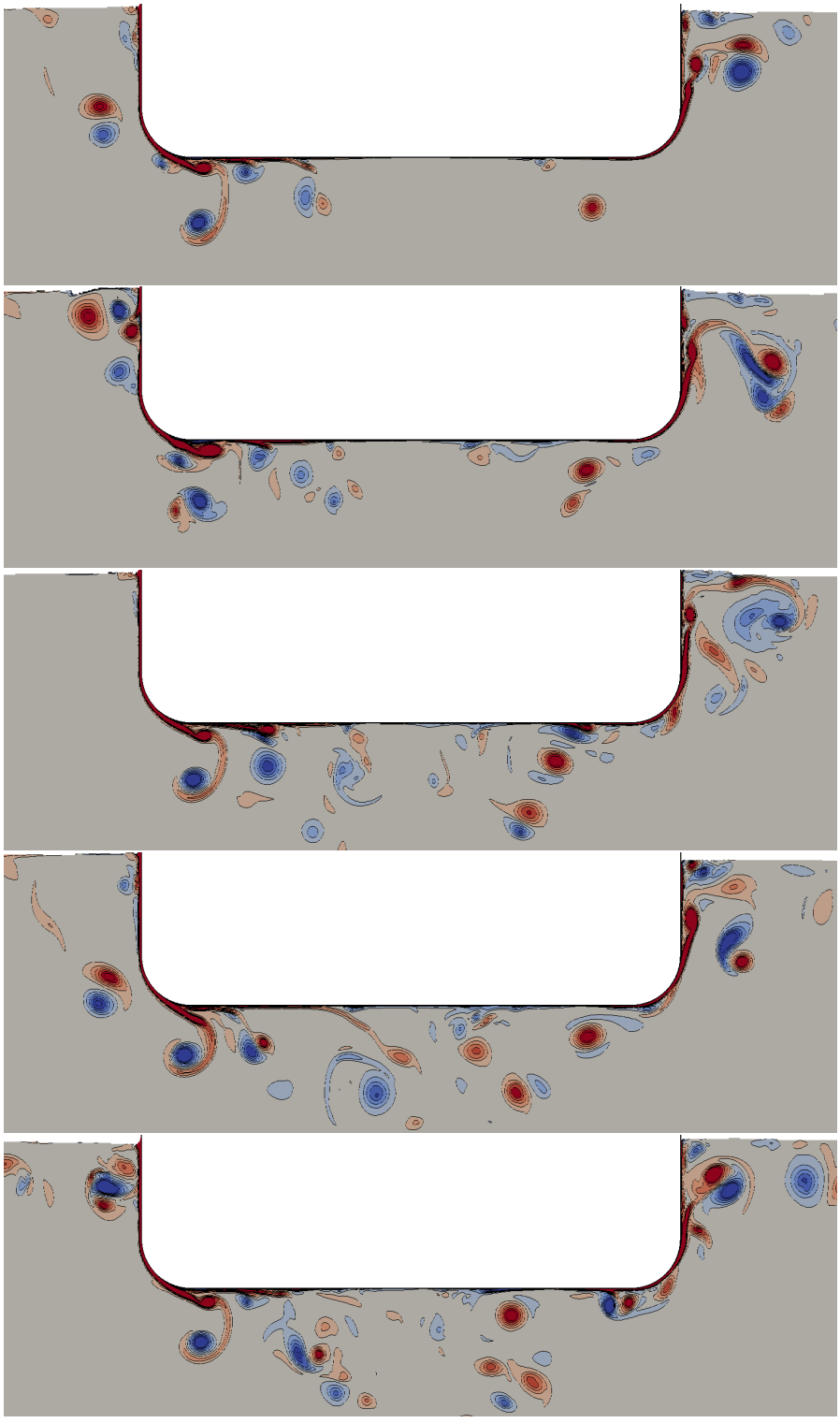

Figure 4.38.: Vortex shedding at the main section without bilge keel; vorticity magnitude at the beginning of the roll cycle 2,3,4,5,6; LES simulation

4.3.2. 3D Test Cases

The setup for a forced motion test in 3D is essentially the same as for the 2D case in the previous section. The difference is that an inflow velocity may be added and the computational effort (number of cells) is much higher. The following section presents three case studies that were conducted to analyze the influence of the bilge keel tip shape, develop the computational setup for double body simulations and investigate the LES turbulence model in comparison with the RANS method.

Variation of the Bilge Keel Geometry

To predict the roll damping effect of bilge keels, systematic tests over a range of different geometries and flow conditions were conducted (see Piehl and el Moctar [6]. Numerical simulations of large ship hulls with relatively small bilge keels often suffer from problems arising from different geometric magnitudes. In order to capture the geometric features of the bilge keel with the FV mesh, a very small cell size has to be used, which results in a very small time step size (in order to comply with the Courant number). Another problem is that the numerical solver (`interDyMFoam`) tends to become unstable for meshes with a very large size difference between the size of the largest and smallest cell.

The common roll damping test procedures *roll decay*, *forced roll moments* and *forced motion* were presented Sec. 2.3 in tests. They all have a similar test setup (see Fig. 4.23 and roll decay test setup in Sec. 4.2.5). During a roll damping test the hull oscillates about its axis of rotation and the interaction between bilge keel and fluid generates a damping force acting against the direction of motion.

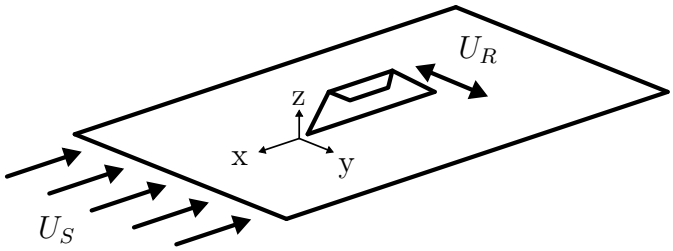

Figure 4.39.: Simplified bilge keel test setup

In order to reduce the complexity of the flow problem several simplifications had to be made. By assuming that the flow effects around the bilge keel do not interact with the water surface, the solution of a multiphase flow with a free surface becomes unnecessary. Another significant simplification was made by transforming the rotational motion into a pure translation. This was achieved by neglecting

the curvature of the hull and transforming rotational motion into an equivalent translational motion as indicated in Fig. 4.39.

These model assumptions allowed to use the test setup shown in Fig. 4.39. The sketch shows a flat plate (a section of the hull surface) with a L-shaped bilge keel (L-BK) protruding from the surface. The bilge keel has a height of $z = 0.4m$, a length of $x = 5.6m$, the tip has a width in y-direction of $y = 0.1m$ and the leading and the trailing edges are chamfered. Aside from the L-shaped bilge keel an I-shaped bilge keel (I-BK) was constructed, which has the same measurements as the L-shaped BK but without the tip.

In this test setup (Fig. 4.39), the ship speed was emulated by a steady inflow condition U_S from the left and the roll motion by an oscillating motion of the bilge keel in perpendicular direction to the inflow. The amplitude of the oscillation was set in a way that the path length of the translation is equal to the length of the circular motion of the bilge keel on a rolling ship.

The boundary conditions of the numerical simulation are set in reference to the local reference frame of the bilge keel. This fact allowed to model the motion of the bilge keel with an oscillating flow instead of moving the bilge keel and the whole computational domain or deforming the mesh to account for the roll motion. In this simplified setup the hull surface and the bilge keel are fixed and the flow scenario was simulated by a constant inflow resembling the ship velocity and an oscillating cross flow which represents the roll motion.

The bilge keel geometry was defined by a triangulated surface, that was generated with a parametric script using python and the open source CAD library OpenCascade [86]. The use of a parametric geometry definition allowed to control the shape and dimension of the bilge keel by a small set of parameters and to automatically generate a variation of bilge keel shapes over a defined range of parameters.

The finite volume mesh was generated with the OpenFOAM meshing tools `blockMesh` and `snappyHexMesh` [70]. The mesh size and its refinement regions were controlled by configuration files and the quality of the generated mesh was checked visually with paraview and by computing cell quality values such as aspect ratio, orthogonality and cell volume. A coarse mesh containing cells with a large size aspect ratio or a too large size gradient would dampen the vorticities in the flow. To avoid this, the computational domain was discretized with homogeneous orthogonal cells with an ideal size aspect ratio of one. The alignment of the mesh cells to the shape of the bilge keel was generated with the so called *snapping* method of `snappyHexMesh`. In order to improve the resolution of the near wall shear flow, several layers of prism cells were extruded from the surface of the hull and the bilge keel (see Fig. 4.40). Additionally, in order to correctly

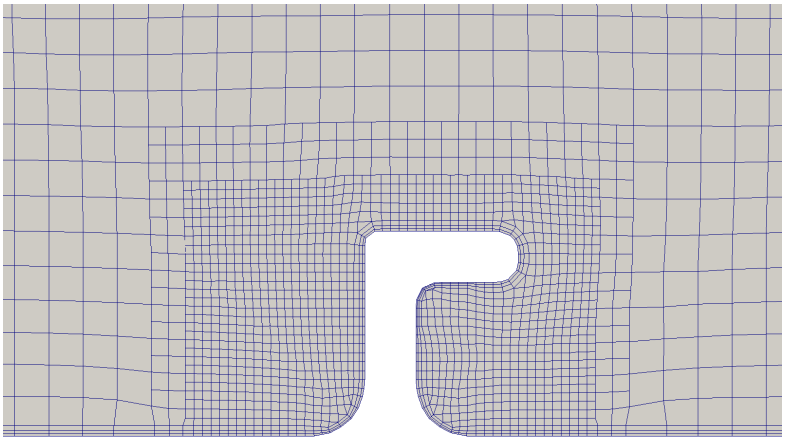

Figure 4.40.: Orthogonal finite volume cells with refinement region and prism layer around bilge keel cross section

resolve the geometric features the region near the bilge keel was resolved with a higher refinement level. The used mesh size varied between $0.8 \ldots 3.2 \cdot 10^6$ cells.

At the beginning of the simulation the flow field and the domain boundaries are initialized with the ship velocity in parallel alignment to the bilge keel. If an oscillating cross flow is used during the simulation, an oscillating velocity component perpendicular to the ship velocity is added to the boundaries. The oscillating boundary conditions were realized with the OpenFOAM library extension GroovyBC [87]. The numerical flow problem was solved with the OpenFOAM solver `pimpleFoam` which employs a combination of the PISO and the SIMPLE algorithm. An adaptive time step control is applied which limits the Courant number to a maximal value of 0.5. The standard OpenFOAM kωSST turbulence model was used in combination with a turbulent wall function on the hull and bilge keel surface.

The simulations were initialized with an impulsive inflow U_S. The cross flow was controlled with a time-dependent sinus function. The turbulent field variables were computed with the equations $k = 3/2\,(U\,I)^2$, $\omega = k^{1/2}/l$ and $\nu_t = k^{1/2}l$ [21], [24] and the estimated values for the turbulent length scale $l = 0.005m$, a mean flow velocity $U = 1.0m/s$ and a turbulent intensity of $I = 5\%$. The derived variables $k = 3.75 \cdot 10^{-3}[m^2/s^2]$, $\omega = 12[s^{-1}]$ and $\nu_t = 3 \cdot 10^{-4}[m^2/s]$ were set uniform to the flow field at start time and constant on the boundaries. It has to be mentioned, that during the simulation these values rapidly decay with increasing distance to the inflow patch.

Table 4.8.: Test case setup

Variation	BK shape	inflow U_S	cross flow U_R
01	L-BK	const.	osci.
02	L-BK	const.	zero
03	no-BK	const.	osci.
04	no-BK	const.	zero
05	I-BK	const.	osci.
06	I-BK	const.	zero
07	L-BK	zero	osci.
08	I-BK	zero	osci.

In order to conduct a systematical comparison of two different bilge keel geometries a moderate velocity scenario was defined. The velocity was kept low to keep the computational domain small enough for a fast calculation of multiple test cases. On the other hand the velocity was chosen high enough to ensure a fully turbulent flow condition.

The computed test variations combine different simulation parameter: bilge keel shapes (L-BK, I-BK am no-BK), constant and zero forward speed U_S and oscillating, constant and zero cross-flow U_R. Table 4.8 lists these case variations and the used simulation parameter. The test cases with a zero cross flow allowed an investigation of the influence of the bilge keel shapes on the forward resistance force. In order to relate the findings to the more common roll damping tests with zero ship speed, additional tests with zero forward speed were conducted. Furthermore two simulations without a bilge keel were added to the list of test cases in order to compare the results with flat plate measurements.

For the unusual test setup and complex flow conditions no validation measurements were available. To estimate the accuracy of the numerical simulations the skin friction of the steady flow along the plain surface was compared to the ITTC 57 friction line. The length of the hull surface is $L \approx 20.0\,m$, the steady inflow is $U_S = 2.0\frac{m}{s}$ and the kinematic viscosity was set to $\nu = 1.0 \cdot 10^{-5}$, this results in a flow a Reynolds number of $Re = 4.0 \cdot 10^6$. The cross flow was defined by the velocity $U_R = 1.0\frac{m}{s}\sin(\omega\, t)$ and the angular frequency $\omega = \frac{2\pi}{5.0}\frac{1}{s}$.

$$C_{f,\mathrm{ITTC57}} = \frac{0.075}{\left(\log_{10} Re - 2.0\right)^2} \tag{4.25}$$

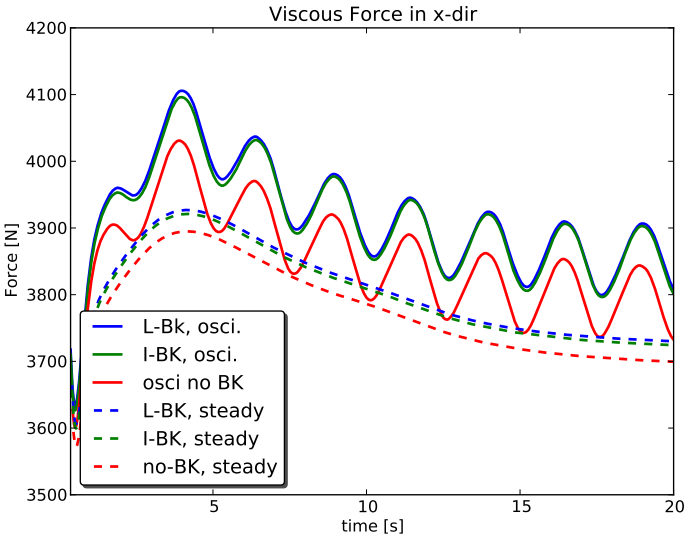

Figure 4.41.: Tangential forces in x-direction for all six cases

Equation (4.25) defines the friction coefficient C_f according to the ITTC57 as a function of the Reynolds number Re [56]. For the above approximated Reynolds number, this equation led to a friction coefficient of $C_{f,\mathrm{ITTC57}} = 0.0035$.

For a rough estimate of the quality of the mesh and the numerical solution procedure, the skin friction coefficient resulting from the simulation was compared to the ITTC57. Equation (4.26) states the skin friction coefficient depending on the recorded friction force F_f, the fluid density ρ, the velocity U_{ship} and the wetted area of the wall surface S_{wet} [19].

$$C_f = \frac{F_f}{\frac{1}{2}\rho U^2 S_{\mathrm{wet}}} \tag{4.26}$$

This equation yields a skin friction coefficient of $C_f = 0.0033$ for a computed steady force of $F_v = 3686\,N$, a velocity of $U_{\mathrm{ship}} = 2.0\frac{m}{s}$ and an area of $S_{\mathrm{wet}} = 550\,m^2$. That is a deviation of about 6% from the estimated ITTC57 value.

The time series of the tangential force in Fig. 4.41 shows that for a steady inflow condition the flat surface has the lowest resistance while for the other two cases with the I-shaped and the L-shape bilge keels the resistance increases due to the larger area that is in contact with the fluid. The time series of the resistance force show another feature for the cases with the oscillating cross flow. While the force oscillates as expected with twice the frequency of the oscillation period, the resistance is always higher than its steady inflow counterpart, even at the zero crossings of the cross flow where both simulation cases have the same flow rate.

Another very simple approach to check the quality of the simulation setup was to simulate a steady flow in y-direction and compare the drag force with the empirical equation for the drag force of a simple rectangular plate with the same flow conditions. The drag force is defined by $F_{drag} = 0.5\rho c_d A u^2$ where the drag coefficient is assumed to be $c_d = 2.0$, $\rho = 1000 kg/m^3$, $u = 1.0 m/s$ and the projection area of the bilge keel onto the normal plane of the flow direction is $A = 5.2 \cdot 0.4\, m^2$ [19]. This results in a drag force of $F_{drag} = 2080N$ which is in good agreement with the simulated drag force for both bilge keel shapes of $F_{sim} = 1940N$ (the drag force at a steady state were nearly the same for both shapes).

Figure 4.42 shows a snapshot of the vorticity in the wake of the bilge keel. The figure shows an iso-surface of the magnitude of the vorticity. The bilge keel is located in the front of the image and the mean velocity point towards the back of the image.

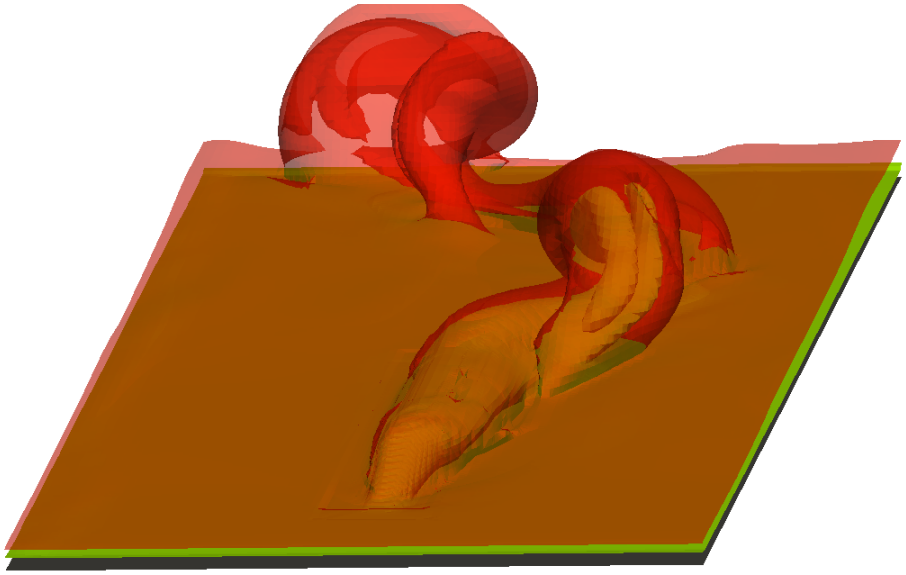

Figure 4.42.: Iso-surface of the trailing vorticity in the wake of the bilge keel

The increasing volume of the iso surface indicates the growing diffusion of the vorticity with increasing distance to the bilge keel. Additionally it can be observed in time lapse of the flow that the vortex sheets separated from the edge roll up to a vortex tube which is transported away from the bilge keel with the mean flow velocity. Due to the changing cross flow the vortex tube soon breaks up into smaller intertwining vortices.

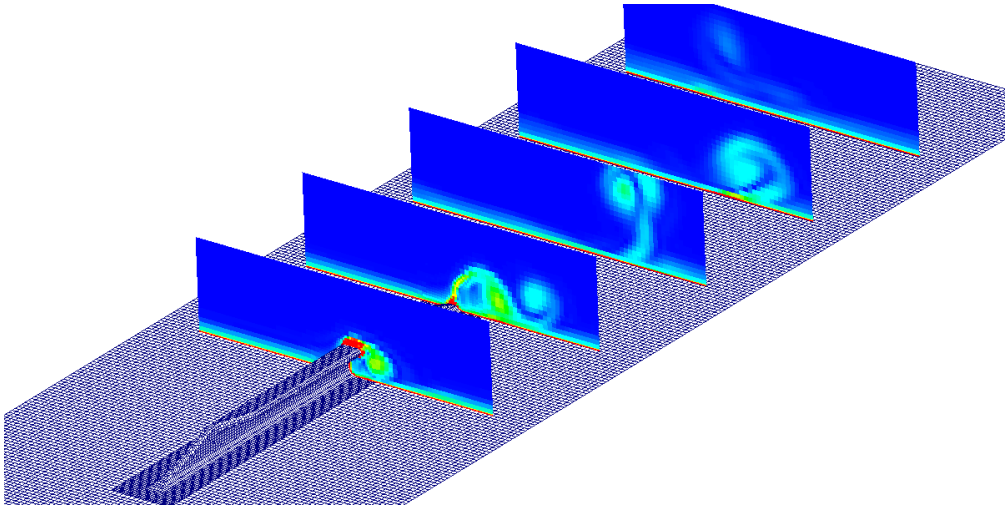

Figure 4.43.: Surface mesh of the hull and the bilge keel; volume slices through the wake, colored by the vorticity magnitude

In Fig. 4.43 another image of the vortex evolution is visualized by several volume slices perpendicular to the inflow. The slices – colored by vorticity magnitude – indicate the vortex sheet roll up. Both figures, 4.42 and 4.43 also give an impression of the boundary layer thickness compared to the bilge keel height.

One objective of this case study was to quantify the interaction of the vortices with the hull. The influence of the hull onto the vorticities can be observed by their motion near the hull surface. On the other hand the friction generated by the rotational velocity of the vorticities can be measured by the component of the tangential force that points in direction of the oscillation motion.

The time series results of the tangential force due to the oscillation (see Fig. **??**) indicated no significant difference between both bilge designs or even between the plain hull surface and the bilge keels. The viscous interaction between vortices and hull surface appears to be negligible.

The normal force on the bilge keel correlates to the inertia (or added mass) which was generated by its motion through the fluid. While the viscous force in the above paragraph acted in tangential direction of the hull surface, the normal force on the surface of the bilge keel was generated by the acceleration of the fluid and point in normal direction of the bilge keel surface. Figure 4.45 shows the time series of the normal forces in y-direction. The forces for the case without a bilge keel are zero because every face element of the hull surface is oriented in tangential direction to the flow.

As expected the forces on the both bilge keel shapes oscillate with the same frequency as the cross flow. In addition to the structural stiffening of the bilge

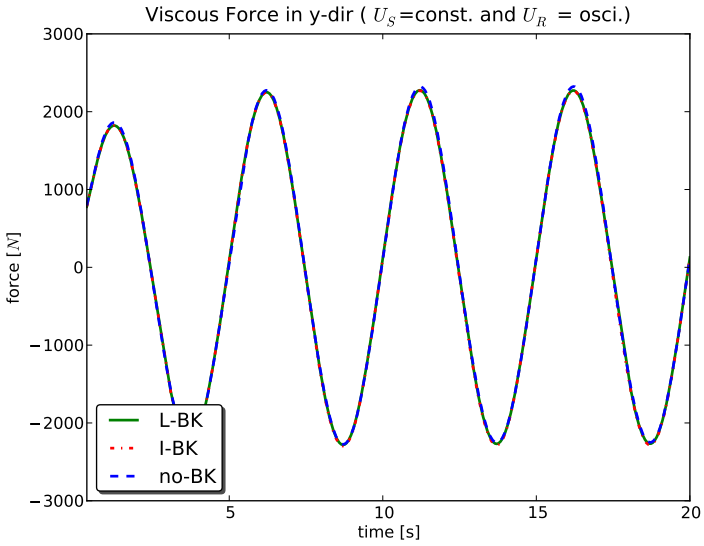

Figure 4.44.: Tangential force on the hull surface in direction of the oscillation motion

keel tip, the idea of the L-shaped bilge keel design was to amplify the roll damping during the inclining phase of the roll motion and to lessen the damping during the declining phase. The aim is to emphasize the uprighting motion and to damp the roll excitation. From the pressure forces it could be observed that the time series for the L-shaped bilge keel was indeed unsymmetrical. A higher force is needed to move the bilge keel in direction of its tip than in the opposite direction.

An unexpected effect was observed in the time series for the L- and I-shaped bilge keels: For the L-shape, the reaction force is smaller than the force on the I-shaped bilge keel, although they have the same projected area. Figure 4.45 shows this effect, which is independent of the speed; it can also be observed in Fig. 4.49 and 4.50, by comparing the vortex motion and the vorticity magnitude of the flow near both bilge keel shapes. If the cross flow points in the same direction as the tip of the L-shape the force function has about the same amplitude but a shorter peak time, while in the opposite direction the shape of the force maximum is similar but the force on the L-shaped bilge keel is overall smaller.

In order to investigate the influence of the ship speed, additional simulations with a zero inflow velocity – which correlates to a rolling ship without forward speed – were conducted. In figure 4.46 and 4.47 a comparison between zero and constant inflow velocity is shown. In Fig. 4.46 the pressure force acting on the

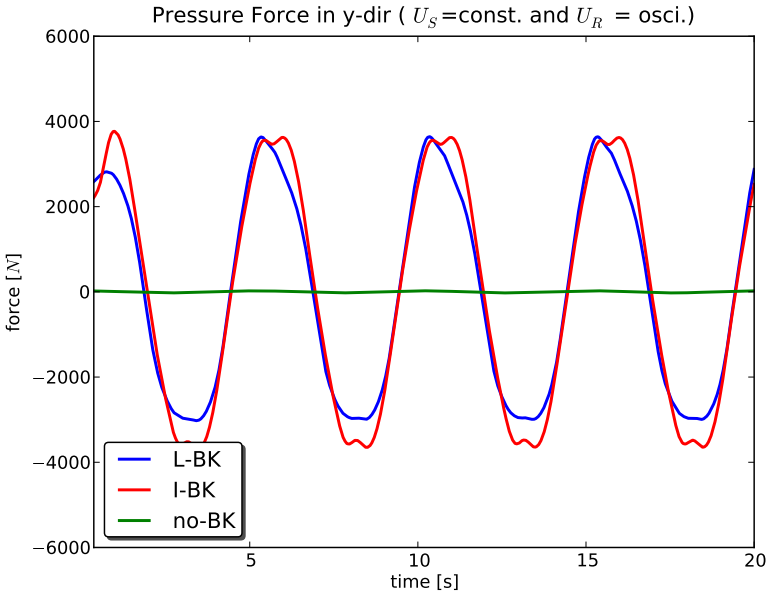

Figure 4.45.: Time series of the normal force acting on the bilge keel due to the oscillating cross flow

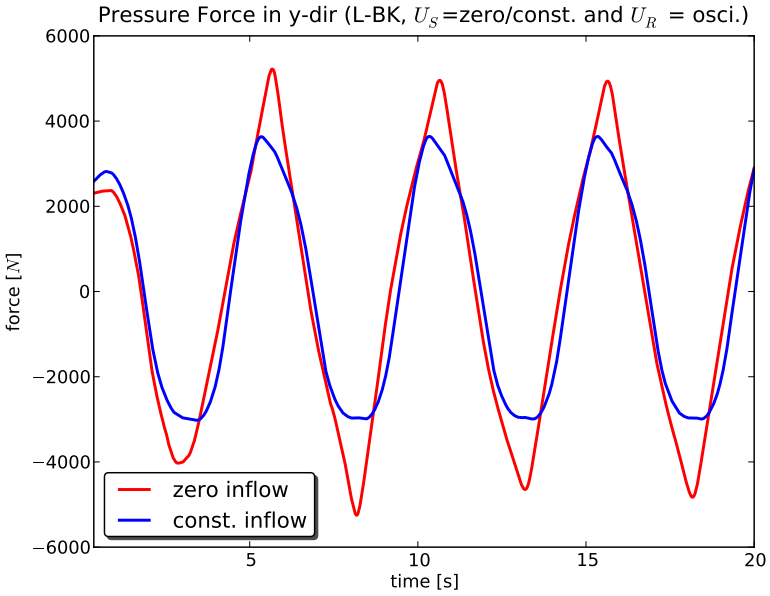

Figure 4.46.: Pressure force in y-dir. on a L-BK with and without forward velocity

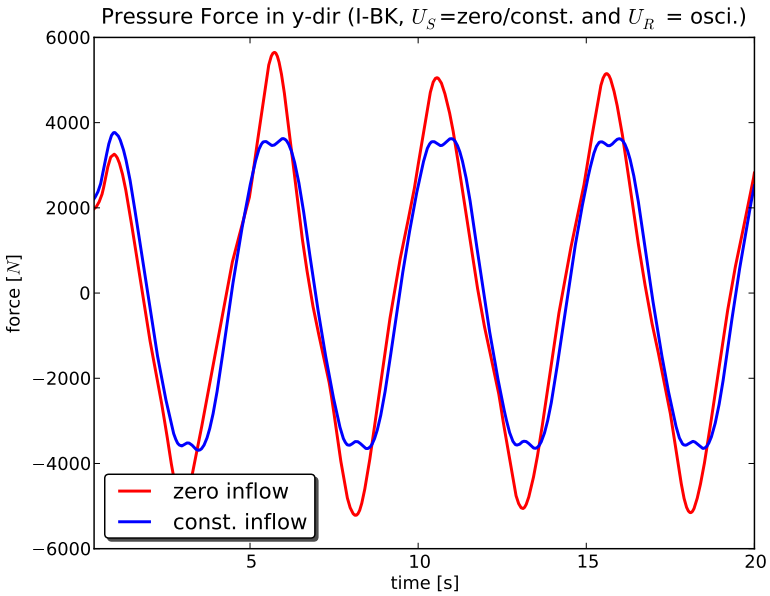

Figure 4.47.: Pressure force in y-dir. on an I-BK with and without forward velocity

bilge keel in y-direction is shown for the L-shaped bilge keel and Fig. 4.47 shows the same results, but for the I-shaped bilge keel.

The most significant difference is the higher force peak for the zero velocity case. This effect can be explained with the resulting angle of attack of the flow and the blunter shape of the bilge keel in the y-direction. Another explanation is that the vortex sheet separated from the edge of the bilge keel stays longer stable because of the exact perpendicular flow direction. For the case of the inclined inflow the vortex sheet detaches earlier, preventing an increase of the force.

Another feature of the zero speed case was that the unsymmetrical behavior of the L-shaped bilge keel disappears if the mean flow field has no x-component because of the zero inflow condition. The effect originates from the constant projection area of the bilge keel onto the normal plane of the flow direction. This effect also explains the similar amplitude of the force for both bilge keel shapes: they have same projection area in the normal-y-plane.

Additionally to the interpretation of the force time series the mechanical power needed for the oscillatory motion of the bilge keel can be investigated. With the relation $P(t) = \mathbf{F}(t) \cdot \mathbf{v}(t)$ the power exerted from the bilge keel can be computed. Figure 4.48 shows the time series of the force, the power and the kinematic state of the bilge keel during one motion period. The power time series oscillates with the double frequency of the excitation. Values above zero indicate that energy has

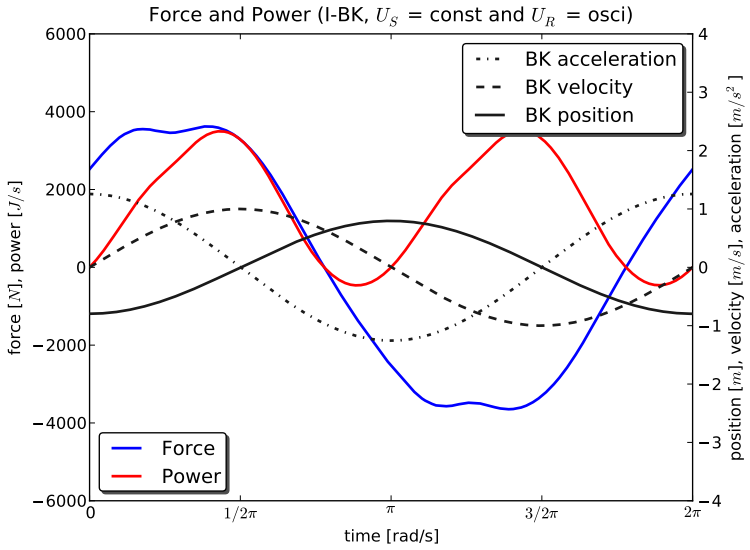

Figure 4.48.: Normal force in y-direction and mechanical power of a I-shaped bilge keel with oscillatory motion

to be put into the system while negative values for the power indicate that the bilge keel is pushed by the fluid along its direction of motion. The area below the power time series is the energy necessary to move the bilge against the resistance of the fluid. In order to optimize the efficiency of a bilge keel this value has to be maximized, while forward resistance has to be minimized.

The images in Fig. 4.49 and 4.50 show the vorticity magnitude in a cross section through the bilge keel. The slice has the same position as the first cutting plane shown in Fig. 4.43. Each figure shows four images at the same moment of time. In the first image the cross flow comes from the left. In the second image the cross flow has reached its peak velocity, the third image shows the moment where a new vortex sheet starts to detach from the edge of the bilge keel and the previous vortex is transported onto the other side of the bilge keel. The last image shows the core of the detached vortex which is transported downstream. The difference between the images in both figures is that even though they are colored with the same scale, the vortices shed from the I-shape bilge keel have a higher intensity.

The results of the six test cases show that the simulation setup is functional and that different bilge keel designs can be tested and their efficiency can be qualitatively and quantitatively compared. The setup of the simulation cases, the solution control and the post-processing routines developed for this study represent a set of computational tools that allow the investigation of the properties of new

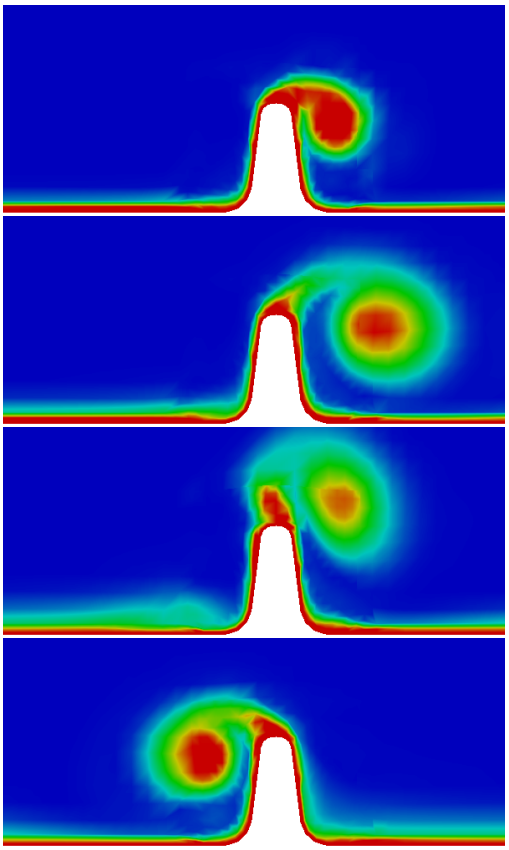

Figure 4.49.: Vortex strength in a section plane at the I-shaped bilge keel

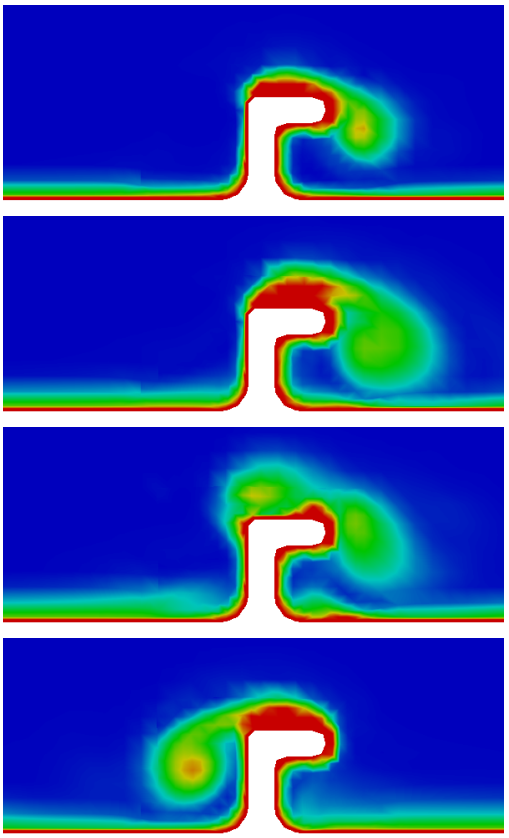

Figure 4.50.: Vortex strength in a section plane at the L-shaped bilge keel

bilge keel designs in a defined framework. The motion energy and the forward resistance represent two scalar measures of the bilge keel, which can be used – together with shape parameter and flow properties – as control variables for the development of *optimized* bilge keels.

The actual results of the simulated test cases show a mixed picture. It was confirmed that the functionality of the bilge keel is mostly pressure dominated. The approach to study the interaction between vortex and hull surface has failed due to the lack of significant differences between the friction forces of the three shape variants.

The idea of the L-shaped bilge keel design is to tune the roll damping effect to an asymmetric behavior by easing the uprighting motion and enhancing the resistance against roll inclination. This desired effect could be proven for bilge keel attached to one side of the ship. One has to keep in mind that on the other side of the ship an L-shaped bilge keel is pointing in the opposite direction thereby compensating the asymmetry. In order to increase the overall damping effect, the inclining resistance of the L-shaped bilge keel has to be enhanced without reducing the resistance during the uprighting motion of a ship hull. The L-shaped bilge keels fails this condition because of a roll resistance which is lower than that of the simple I-shaped bilge keel.

A simulation setup which takes the free surface and its distance to bilge keel into account would be better suited to investigate the desired asymmetric rolling behavior. The result, that the L-shaped bilge keels are less effective than simple plates, is surprising, but physically plausible if the lesser reaction force can be explained by a smoother cross flow over the flat tip of the bilge keel (see Fig. 4.45, Fig. 4.49 and 4.50).

Double Body Simulation

The simulation setup of the linear motion of a bilge keel presented in Sec. 4.2.3 was extended to conduct 3D double body roll simulations of a full ship hull. For this purpose the underwater part of the hull was meshed within a computational domain in the shape of a half cylinder. The mesh is similar to the lower part of the cylindrical inner mesh shown in Fig. 5.11 in Sec. 5.2.2.

The flow condition of a rolling double body was generated by the same in- and outflow conditions that were used in every other 3D case, a slip condition in the far field on the cylinder wall, periodic boundary conditions on the symmetry plane (coinciding with the water level) and an oscillatory rotating body force around the roll axis (coinciding with the cylinder axis). Figures 4.51 and 4.52 each show a series of images of the dynamic pressure on the ship hull at five time points during the first half of a roll cycle.

Figure 4.51 shows the dynamic pressure around the segmented bilge keel of the DTC hull rolling without forward speed and figure 4.52 shows the results for the same case setup, but with 1/6th of the design speed. The pattern of the dynamic pressure correlates with the motion of the vortices shedded form the bilge keel tips. The blue low pressure regions that have separated from the bilge keels are generated by the low pressure cores of the vortices. The figures show the bilge keels in a view from the top, while for example figure 4.49 shows the same flow effect from a side view along the bilge keel. The pressure distribution in the second figure 4.52 indicates how the vortices are transported in downstream direction of the flow.

The same behavior of the vortices was also found in Fig. 4.42 and 4.43 of the case study in the previous section. The angle between bilge keel camber line and the blue low pressure line depends on the direction of the forward speed and the current angular roll velocity. The vortex pattern as well as the time series results of these simulations showed little interaction between the vortex systems of two neighboring bilge keels.

LES Simulations

The LES turbulence model used for the linear oscillating bilge keel in Sec. 4.2.3 was also used to conducted double body simulations of a rolling ship hull with bilge keels. Initially, the simulations were planned to run on a mesh encompassing the whole ship hull, but to meet the cell size requirements of the LES turbulence model, the size of the domain had to be reduced The computational domain of the double body case setup (used in the previous section) was reduced to only cover one bilge keel segment near the main section. This allowed an investigation of the 3D effect of a bilge keel, but without the influence of a forward velocity or the free water surface.

The 3D view of the iso-surface of a specific vorticity strength in Fig. 4.53 and the 2D snapshots of the vortex magnitude in Fig. 4.54 originate from the same simulation case. The mesh for this simulation consists of $12 \cdot 10^6$ cells and it took about three weeks to compute four roll cycles on 32 cores. The fine, complex pattern that can be observed in both figures match the vortex behavior of the linear bilge keel motion shown in Fig. 4.15 of the case study in Sec. 4.2.3.

The forces on the bilge keel and hull show the same kind of behavior between RANS and LES simulation. The mean forces are very similar, but the LES results show a stronger, irregular fluctuation. That means that as long as only the surface forces are of interest and the influence of the detached vortices is small, the computational *cheaper* RANS simulations have a sufficient accuracy. Compared with the 2D simulations described in Sec. 4.3.1 the results again show the principle difference of the vortex motion between 2D and 3D flows.

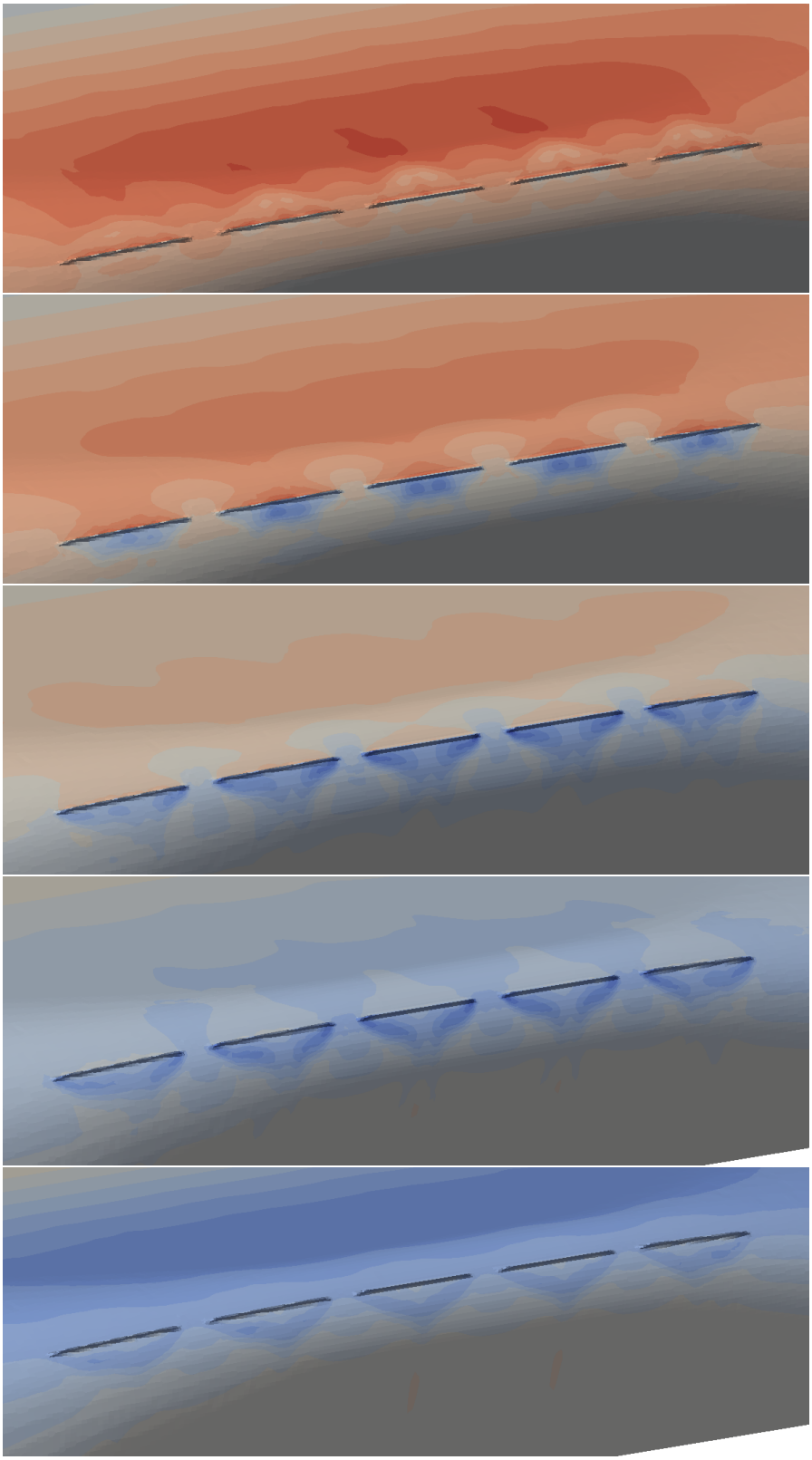

Figure 4.51.: Surface pressure distribution near bilge keels; five time points within $\Theta = 0 \ldots \pi$; zero forward speed; 3D RANS simulation

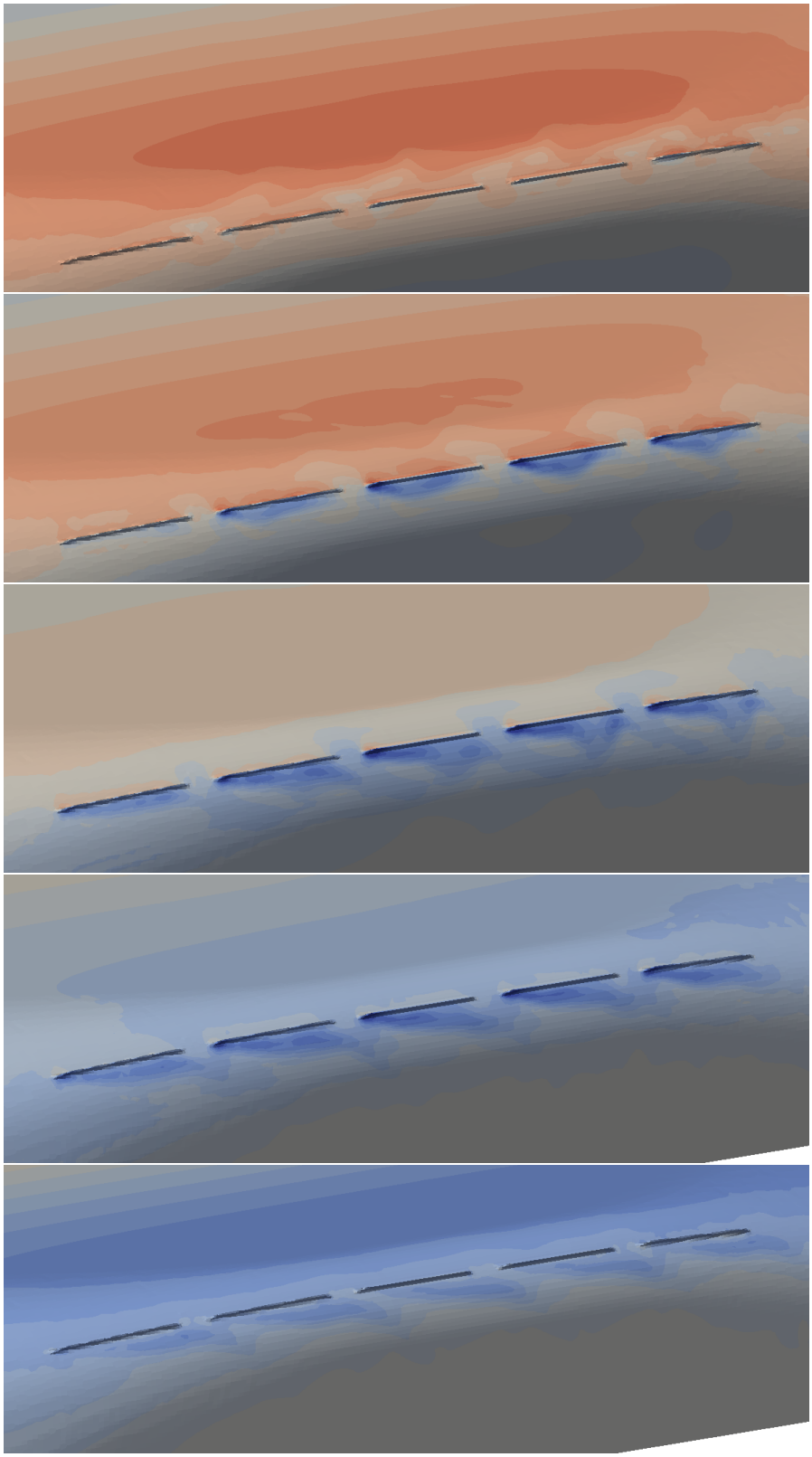

Figure 4.52.: Surface pressure distribution near bilge keels; five time points within $\Theta = 0 \ldots \pi$; with 1/6 forward speed; 3D RANS simulation

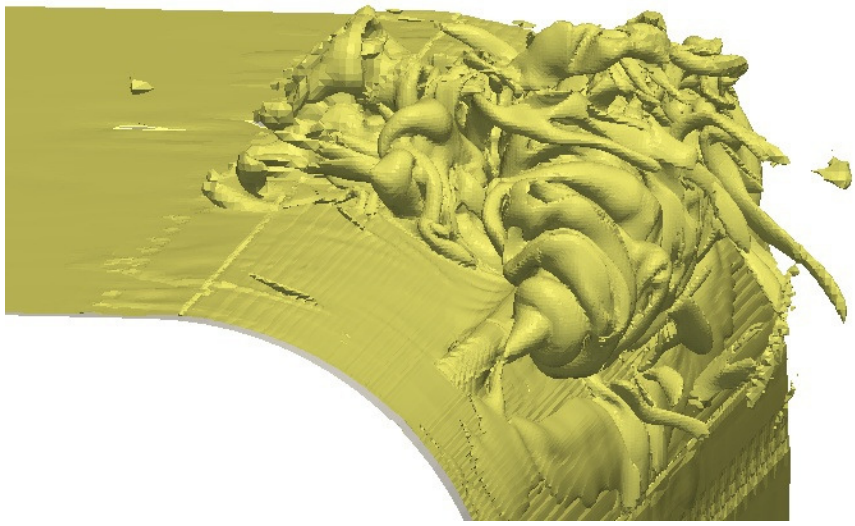

Figure 4.53.: Iso vorticity around hull section with bilge keel; 3D LES simulation

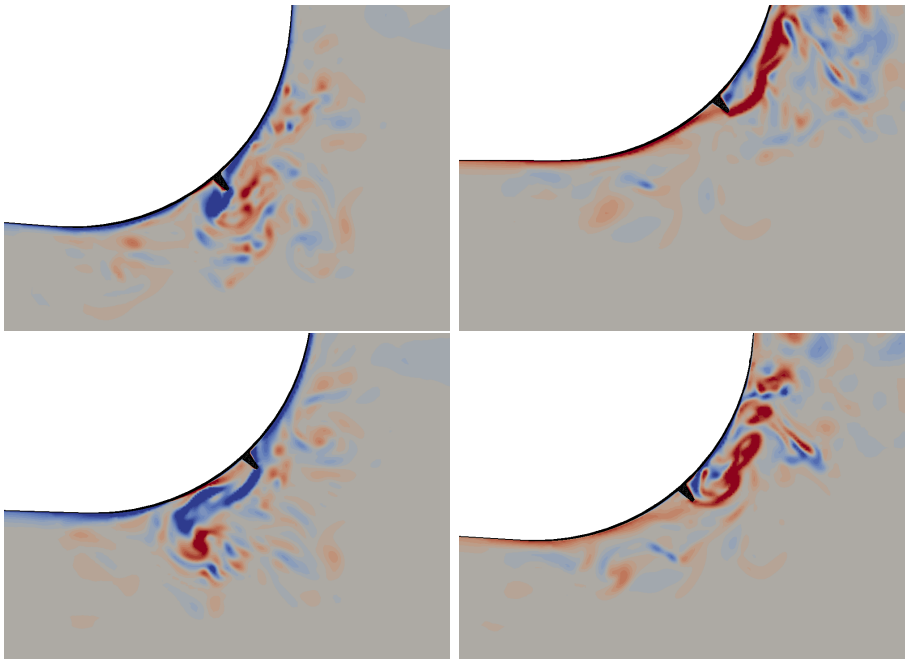

Figure 4.54.: Vorticity magnitude in the cross section of a bilge keel; 3D LES simulation

5. Regression Analysis

The objective of the regression analysis is to find a mathematical model that relates the shape of a ship hull to its roll damping properties. In order to conduct this analysis a set of input parameter and the according results are required. In the context of the development of a roll damping prediction method, the input is a list of parameter that define the shape of the hull and the results are the roll damping coefficients obtained for each parameter variation.

The following section presents a description of the investigated ship parameter, the systematic computation of the roll damping coefficient for each parameter variation, the application of a regression analysis method and the resulting mathematical model of the roll damping coefficient.

The final state of the implemented computational framework allowed to conduct the roll damping investigation of a specific set of parameter automatically. After selecting the parameter set from the database the following procedure runs without requiring further input: The procedure selects the according hull shape, creates – if required – the bilge keel geometry file, creates a mesh, generates the OpenFOAM case files, initializes and solves the flow simulation in parallel on a cluster system, retrieves the results, conducts the time series analysis and writes the roll damping coefficients back to the database.

5.1. Variation Parameter

Modern container ships differ widely from the hull shapes used for the development of the Ikeda method. Today's container ships are larger and have a more pronounced bow flare.

Figure 5.1 shows an example of a typical modern container ship. The figure shows the hull of the DTC ship with attached rudder, propeller and, only slightly visible, the segmented bilge keel along the bilge. The 51 m wide ship has the typical feature of its class: the large bow flare.

The investigated parameter can be divided into two groups: geometric parameter like ship size, shapes, appendages and kinematic parameter like ship speed, draft (in a strict sense, the draft is a shape parameter, but it also influences the motion behavior), position of the roll axis, roll period and roll amplitude. A description of these parameter is listed in the following paragraphs.

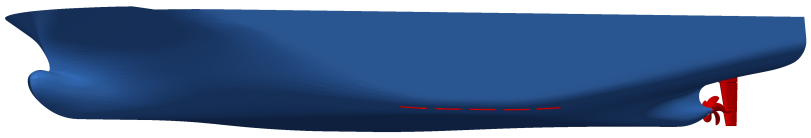

Figure 5.1.: Hull shape of the Duisburg test case with rudder, propeller and segmented bilge keel

5.1.1. Geometric Variation Parameter

Ship Size Figure 5.2 presents the lines plan of the based shape of the three container ships that were used in the systematic roll damping simulations. The first one, is the DTC, a 14.000 TEU post-panamax with a length between perpendiculars of 366 m and a design draft of 14 m. The second ship is a panamax container ship with the length $L_{pp} = 268$ m and a design draft of 12 m. The third ship is a container feeder of 110 m length and a draft of 7.8 m. In table 5.1 the ship parameter for the base shape of all three ships are listed.

The hull geometry methods developed in section 3.4 were used to generate the ship lines shown in Fig. 5.2. The figure shows the base forms of the three investigated ship types PostPanaMax (DTC), PanaMax and container feeder, they were all scaled with the same factor, to show their relative sizes differences.

Shape Variation For each of the above ship sizes three shape parameter that are expected to have the largest influence on the roll damping were investigated. Based on the initial hull the bow and stern deadrise, the bilge radius and the draft-to-beam ratio were variated independently. This approach resulted in six new hull shapes adding up to $3 \times (6 + 1) = 21$ hull shapes overall.

A variation of the deadrise in the bow and stern section is expected to influence the roll damping by changing the amount of vortex shedding on the bilge. Especially in the region of the bulbous bow the roll damping effect of the vortex separation has a large influence. The deadrise of the bow and stern is on the other hand an important parameter for the stability of the ship and has to be changed carefully.

The second variation parameter is the bilge radius. Figure 5.3 shows the variation of the bilge radius at the main section. For the third shape variation parameter the draft-to-beam ratio was changed. In figure 5.4 the three different ratios

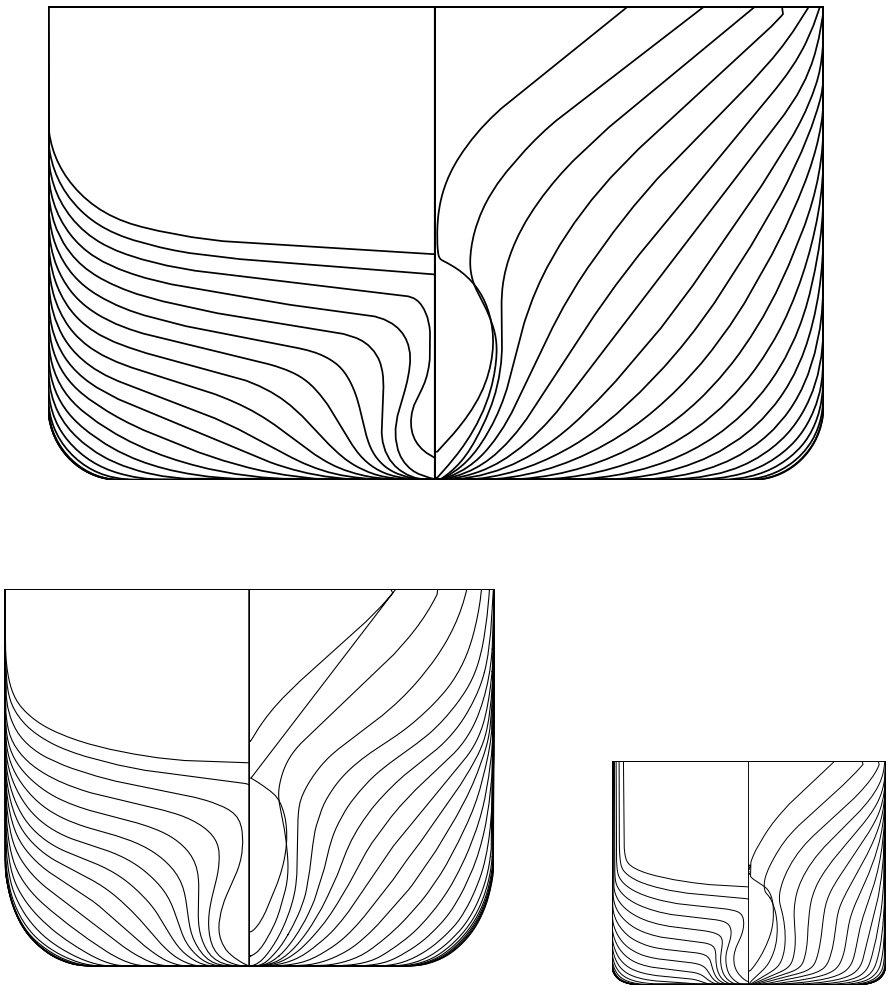

Figure 5.2.: Ship lines and size comparison of the three ships; DTC (top), Panamax (left) and Feeder (right)

(including the base shape) are shown. The draft was varied depending on the beam while keeping the displacement constant! The amount of shape change was estimated with the simplified Ikeda method (see appendix A.4).

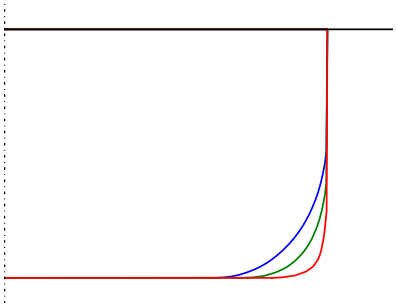

Figure 5.3.: Variation of the bilge radius at the main section; green indicates the base shape

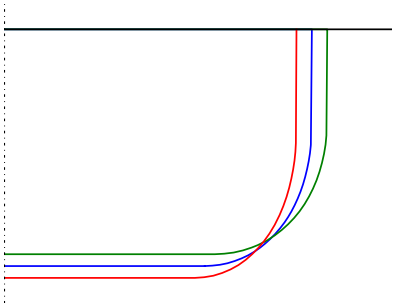

Figure 5.4.: Variation of the beam-to-draft ratio at the main section; blue indicates the base shape

Appendages Figure 5.5 shows the twisted rudder with a costa bulb that was designed within the project. The five-winged propeller shown in the figure was not used during the numerical investigation. Its important influence had to be neglected because of the much more complex numerical setup it would have required to include a rotating propeller.

All hull shapes were tested with and without rudder and bilge keel. While the same rudder could be used for all shape variations, a new bilge keel CAD file had to be created for all 21 hull shapes. To automate this process a python program (see appendix A.5) was developed that can be used to generated parametric bilge keels automatically aligned to an arbitrary hull shape.

5.1.2. Kinematic Variation Parameter

To investigate the dependency of the roll damping from the *kinematic* parameter: ship speed, roll period, roll amplitude, roll axis and draft, an interval with discrete values was chosen for each. The range for these intervals were selected based on a priori defined load conditions and empirical rules.

Ship Speed The speed of the ship has a large influence on the roll damping. To investigate roll damping for zero or slow velocities as well as the design speed the test interval of the whole range was covered in $\frac{1}{6}$ steps.

Table 5.1.: Main data of the three container ships: DTC, PanaMax and Feeder

base shape S001		DTC	PanaMax	Feeder	
draft	T	14.00	12.00	7.10	$[m]$
wetted surface	S_{wet}	21488.67	11534.28	3213.18	$[m^2]$
displacement	∇	165829.18	68584.04	10897.39	$[m^3]$
length btw. perpendiculars	L_{pp}	355.00	268.20	110.00	$[m]$
beam	B	51.00	32.20	18.00	$[m^2]$
water line length	L_{wl}	363.27	270.92	116.64	$[m]$
water line area	S_{wl}	14991.87	7124.54	1772.98	$[m^2]$
main frame area	S_{hs}	704.48	369.88	126.77	$[m^2]$
block coefficient	c_B	0.654	0.662	0.775	$[-]$
main frame coefficient	c_M	0.987	0.957	0.992	$[-]$
prismatic coefficient	c_P	0.663	0.691	0.781	$[-]$
water line coefficient	c_W	0.828	0.825	0.895	$[-]$

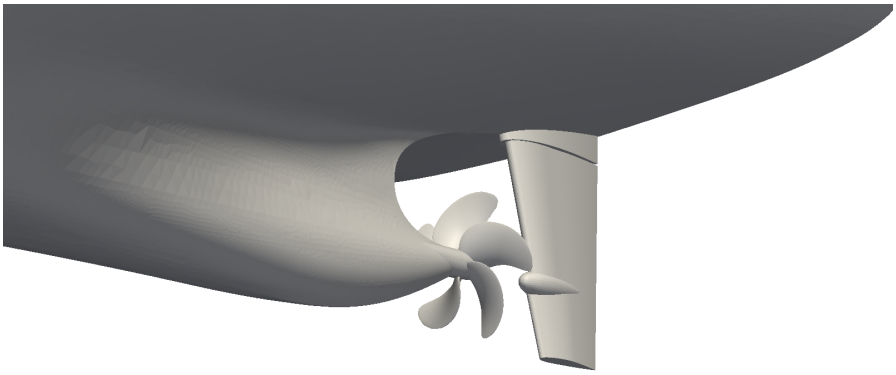

Figure 5.5.: Rudder and propeller at the stern of the DTC hull

Roll Period By viewing the roll motion of the ship in terms of a dynamic system, the natural roll period is, together with the roll damping and the roll amplitude, the most important property. The roll period depends mainly on the loading condition and the hull shape.

Roll Amplitude The restoring moment and the roll damping for large roll angles ($> 10°$) show a nonlinear behavior. Since large roll angle amplitudes may often occur on large container ships and present an increased safety risk their influence on the roll damping has also to be considered.

Roll Axis Depending on the loading condition, the position of the center of gravity, the metacentric height and ultimately the height of the mean position of the roll axis above water level (raz) are changed. The restoring moment and thereby the roll behavior of the ship depends on this parameter.

Draft The influence of the draft was tested for three typical loading conditions: ballast, part and full load. The main part of the numerical simulations was focused on the last two cases.

5.1.3. Test Matrix

The numerical values for all kinematic parameter are summarized in table 5.2. In addition to these main variation parameter further ship coefficients were included in the roll damping analysis. Mainly the beam B, the bilge radius R_B, the length between perpendiculars L_{pp}, the displacement ∇, the wetted surface area S_{wet}, the block coefficient c_B and the main frame coefficient c_M.

Table 5.2.: Test intervals for kinematic parameter

parameter		DTC	Panamax	Feeder	
speed	U	$\left[\frac{0}{6}, \ldots, \frac{6}{6}\right] \cdot 25$	$\left[\frac{0}{6}, \ldots, \frac{6}{6}\right] \cdot 23$	$\left[\frac{0}{6}, \ldots, \frac{6}{6}\right] \cdot 17$	[kn]
draft	T	[9, 12, 14]	[7.2, 9.8, 12]	[4.5, 5.8, 7.1]	$[m]$
roll axis	raz	[0.0, 2.2, 4.4]	[0.0, 0.6, 1.3]	$[-0.4, 0.0, 0.4]$	$[m]$
roll period	T_{roll}	[12.5, ..., 40.0]	[12.5, ..., 40.0]	[10.0, ..., 20.0]	$[s]$
roll amplitude	ϕ_A		[5, 10, 15, 20, 25]		$[°]$

For the accuracy of the analysis, it has to be taken into account that some of the parameter are not constant, but depend on the current roll angle. Even in calm

water condition the wetted surface area S_{wet} and the restoring moment $M_{\phi,\text{stat}}$ change with ϕ. The main influence on the roll damping behavior can be controlled with the variation parameter listed in Tab. 5.2 and the shape parameter ship size, shape variation (base shape plus three times two shape variations) and the appendages (none, with bilge keel, with rudder, with both).

These eight parameters 5.1 were combined in a set P_α (α is a multi-index) that was used as an unique identifier for each test configuration and every entry in the hydrodynamic data base. Each parameter set in the database is linked to the according experimental or numerical obtained time series, derived damping coefficients and additional ship coefficients.

$$P_\alpha = [U_{\text{ship}}, T_{\text{roll}}, \phi_A, \text{raz}, B_{\text{ship}}, T, R, \text{BK}, \text{rudder}] \tag{5.1}$$

The database was implemented with the use of so called python *dictionaries* which allow the structured storage of the heterogeneous data (strings, floats, integer, boolean and lists of the these types). The access to the information was controlled by python routines that allowed to iterate over the whole data base or to select specific subsets (eg. selecting only cases with bilge keels and a maximal roll angle smaller then 10 degrees). The database has the additional functionality to write and read data from hdf5- or xls-files.

Reduction of the Number of Roll Damping Cases

The combination of all parameter would have resulted in over 130 000 test cases. With respect to the computation power of the HPC cluster available at the Institute of Ship Technology, Ocean Engineering and Transport Systems at the university of Duisburg-Essen and the time frame of this study this number had to be substantially reduced.

To do so the test matrix was *thinned* in a way to significantly reduce the number of simulations, while trying to keep the quality of the regression analysis as high as possible.

Figure 5.6 shows the approach that was used to reduce the number of simulations. The left most graphic indicates the full test matrix with a cube. The points each symbolize one parameter set P_α.

The thinning of the test matrix is split into two steps: In the first step the parameter for the shape, draft, roll axis and appendages are not variated but fixed to the base shape, the design draft and the roll axis height to coincide with the water level, thus reducing the number of free parameter combinations greatly. This reduced sub set – annotated *kinematic variation* – is indicated in the center of Fig. 5.6. In this subset only the kinematic parameter U, T_{roll} and ϕ_A are variable. For the base shape of the DTC ship every combination in the sub set were simulated, thereby generating enough points in each parameter interval to

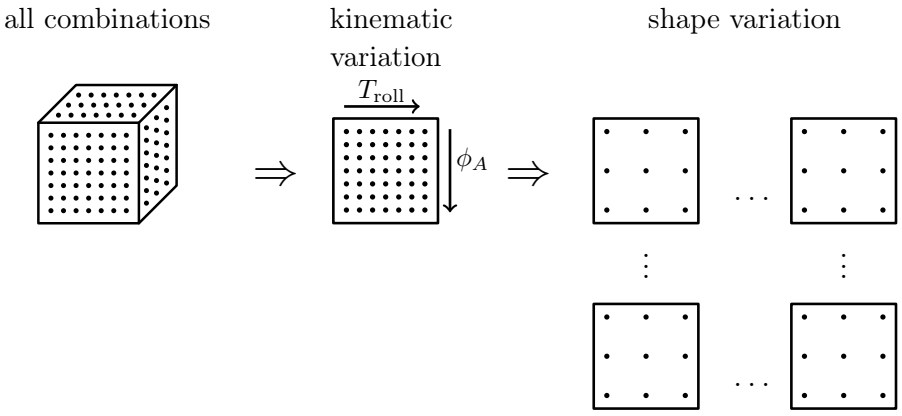

Figure 5.6.: Strategy for the *thinning* of the test matrix

investigate whether the roll damping coefficients have a nonlinear dependency on the parameter.

The second step follows the assumption that the principle effects of the kinematic parameter determined for the base shape can be transferred to the other shape variations. This assumption allows to further reduce the number of parameter combinations for the remaining shapes. These sparsely populated subsets are shown on the right side of Fig. 5.6. They only contain a value for the start, middle and end of the variation intervals. Those sparse sub sets contained few enough test cases to be conducted for every combination of shape parameter.

Although the number of necessary cases was greatly reduced by the above described approach, the assumption that the roll damping influence of two parameter are independent of each other (eg. the bilge radius does not influence the effect of the rudder) allowed to reduce the number of test cases even further.

5.2. Systematic Roll Damping Computation

The setup of the test matrix containing a large number of parameter sets P_α was described in the previous paragraph. In the following section a general description of the computation procedure used to determine the roll damping forces for each parameter set is given.

For the main part of the parameter sets in the test matrix it was possible to conduct 2D computations in addition to the 3D cases. Although the roll damping results of 2D cases have the disadvantages described in Sec. 4.2.3, the short computation time of the 2D cases allowed to investigate more parameter variants. On average a 2D case with $0.2 \cdot 10^6$ cells runs 12 hours on 4 cores while a 3D case

with $1.8 \cdot 10^6$ cells takes 7 days on 12 cores. The differences in the damping behavior between 2D and 3D cases had to be taken into account during the regression analysis.

5.2.1. 2D Forced Roll Motion

As indicated in the introduction to this section the 2D roll damping cases have certain advantages and disadvantages: In 2D, larger forces on the hull may occur because the kinetic energy in the fluid can only dissipate into two spatial directions instead of three. The transport and diffusion of vortices in two dimensions is significantly different 3D. Furthermore the viscous effect of the forward speed and the influence of the rudder and the hull shape in the stern and bow cannot be investigated. The case setup and simulation control follows in general the procedure described in Sec. 4.3.1.

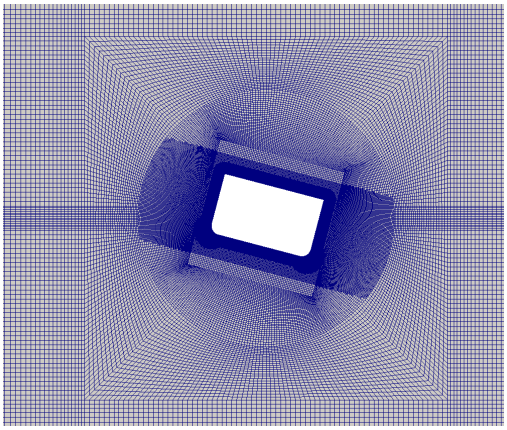

Figure 5.7.: 2D mesh around the main section of the DTC with sliding interface

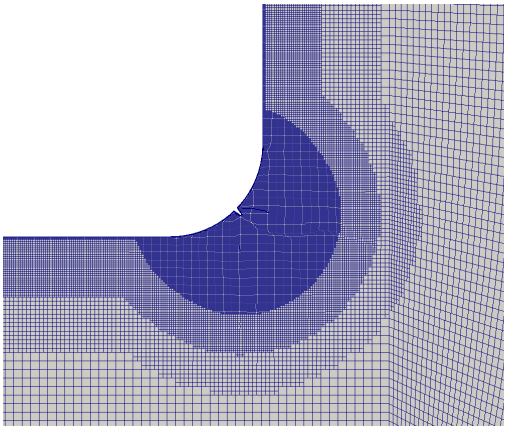

Figure 5.8.: Detailed view of the refinement zones near the bilge keel

The computation of the forced roll motion was computed with the `interDyMFoam` solver in OpenFOAM version 2.1.1. This version of the solver provides the ability to use the *sliding interface* method to move the hull section with a oscillating roll motion. The mesh shown in figure 5.7 consists of two parts, an outer stator mesh and an inner rigid mesh that can be rotated around the roll axis. During the flow simulation the field variables are interpolated across the interface between the stator and the rotor.

The numerical mesh is automatically generated for every shape variation with sliding interface topology, using one of the described python programs. Figure 5.8 shows a detailed view of the refinement zones near the bilge keel.

In the same automated way the mesh was generated, the solver properties and computation control of the simulation case are defined. Because of the automation and the short runtime, almost all shape variations of the DTC (except the variations of the forward speed, the bow and stern shape and the rudder) could be simulated. The conducted parameter variations are listed in the following:

- ▷ 5 hull shapes: base shape and two bilge radius and two draft-to-beam ration variations
- ▷ 2 drafts $D = [12m, 14m]$
- ▷ 2 cases with and without bilge keel
- ▷ 3 roll axis heights $raz = [0.0m, 2.2m, 4.4m]$
- ▷ 5 roll periods $T_{\text{roll}} = [12.5s, 15.1s, 19.0s, 25.8s, 40.0s]$
- ▷ 2 roll amplitudes $\phi_A = [10°, 20°]$,

This amounts to 600 full scale simulation cases with 60 different FV meshes. For each case at least five complete roll cycles were simulated and the time series analysis described in Sec. 3.2 was automatically applied.

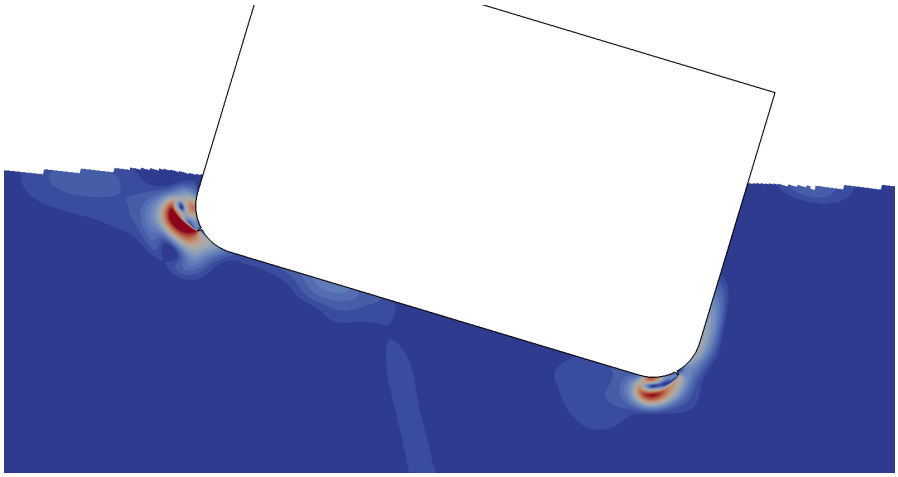

Figure 5.9.: Velocity magnitude; full scale; DTC mid ship cross section; 2D RANS simulation

Figure 5.9 shows an example plot of the velocity magnitude of the flow around the main section of the DTC base shape with attached bilge keels. A second example of the computed results is shown in fig. 5.10. The plot shows the pressure

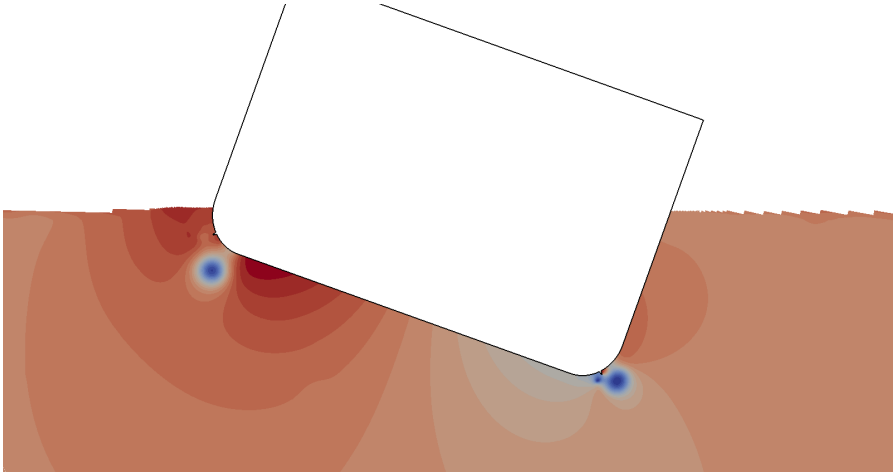

Figure 5.10.: Dynamic pressure; full scale; DTC mid ship cross section; 2D RANS simulation

field around the slimmer draft-to-beam ratio variation. The blue regions in the image are the low pressure cores inside the vortices shedded from the bilge keel tips. See section 3.3.2 for an example roll moment time series and the used time series analysis method.

5.2.2. 3D Forced Roll Motion

The systematic computation of the 3D forced roll motion is set up and conducted in the same manner as the above described 2D cases, differing only in the use of a 3D mesh.

Figure 5.11 shows a 3D mesh with *sliding interface* between the outer stator and the inner rotor. The ship hull inside the cylindrical rotor is positioned in such a way that cylinder axis and roll axis coincide. The mesh refinement is mostly controlled by the cell size and aspect ratio of the background mesh. This approach prevents the occurrence of hanging nodes and the generation of smooth prism cells on the hull surface. The size of the prism cells resulted, together with the wall function, in a y^+ range of 100 - 500.

The OpenFoam solver `interDyMFoam` was also used for the numerical computation. The flow solver was configured to use the kωSST turbulence model and a wall function. The time step size Δt was constant. Simulations were conducted in full scale using a step size of $\Delta t = 0.02$ for cases with a small roll angle amplitude ($10\,^\circ$) and without a bilge keel. For cases with a large roll angle amplitudes ($20\,^\circ$) and a bilge keel attached to the hull, a smaller time step size of $\Delta t = 0.005$ had to be used. The maximal Courant number varied around Co = 0.5. A simulation

with $1.6 - 2.4 \cdot 10^6$ cells on 8-12 cores took about seven days to compute five roll cycles.

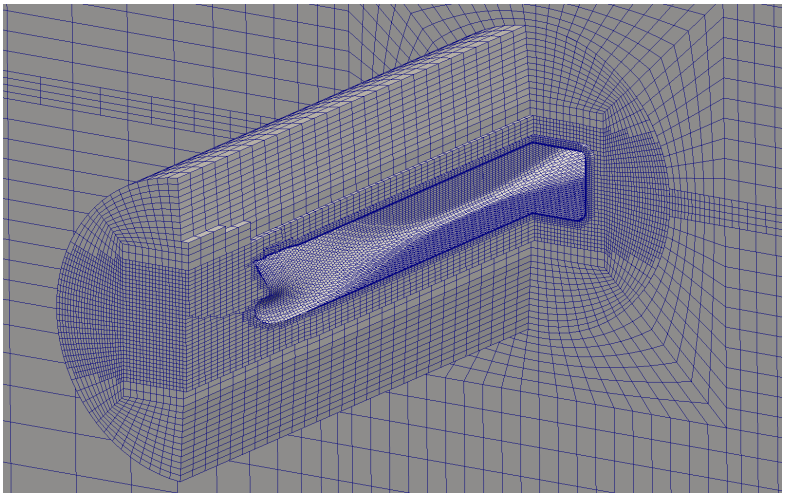

Figure 5.11.: 3D mesh for forced roll motion using the sliding interface method

In addition to the time series of the hull forces, the elevation of the free surface was evaluated. Figure 5.12 shows an example view of the rolling DTC hull, the computational grid at the main section and the wave pattern near the hull. The two images in Fig. 5.13 show a comparison of the waves emitted from the forced roll motion of the DTC hull at $\phi_A = 20\,^\circ$ and $T_{\text{roll}} = 19.0\,\text{s}$. The top image stems from a simulation with zero forward speed, in the bottom image the ship is moving at 25 kn design speed. The two figures allow a comparison of the wave direction and wave height due to rolling and due to forward speed. The maximal wave amplitude of the ship moving at design velocity (Fig. 5.13 bottom) is almost three times higher than the emitted amplitude of the hull at zero speed.

The analysis of the wave pattern helps to explain an effect that was observed in the time series of the hull forces. At zero speed and using large roll angle amplitudes (hence large angular velocities) a peak occur in the roll moment when the ship rolls through its upright position. This peak originates from the hull surface near the transom stern hitting the free surface at flat angle. In simulations with moderate or high forward speed this effect does not occur.

In the start phase of the systematic roll damping study, the two commercial flow solver StarCCM+ and Comet and the open source solver OpenFOAM were used simultaneously in order to evaluate their suitability for viscous roll damping simulations. The availability of a suitable method for mesh motion was also a limiting factor for the CFD solver choice. The sliding interface method could – at that time – not be combined with the free surface method and a mesh morphing

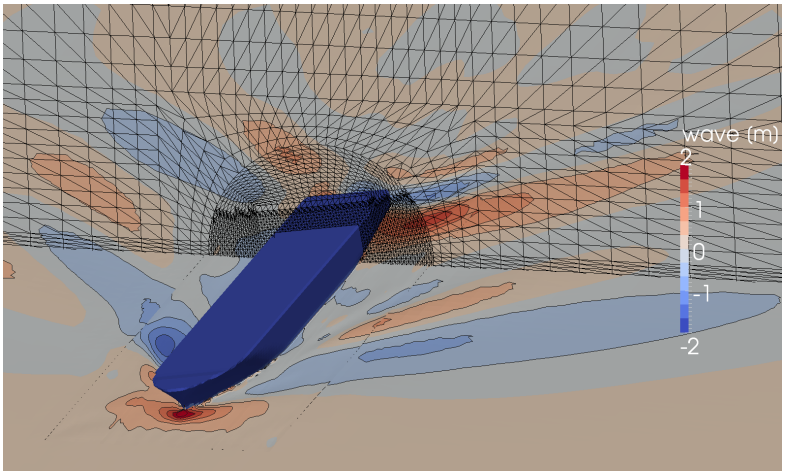

Figure 5.12.: Free surface elevation and mesh motion of rolling DTC hull

Table 5.3.: Comparison of the dimensionless linear roll damping coefficient $\hat{B}_{44}$ between OpenFOAM, StarCCM+ and Comet for the DTC hull at design velocity U=25kn

$\hat{B}_{44}$	OpenFOAM	Starccm+	Comet
dS1D3a1643	0.0094	0.0091	0.0092
dS1D3a1631	0.0100	0.0102	0.0105
dS1D3a1632	0.0108	0.0107	0.0109
dS1D3a1633	0.0115	0.0112	0.0116

method that did not distort the prism layer cells near the hull surface was not freely available.

The numerical methods in StarCCM+ do not significantly differ from OpenFOAM. Both flow solver use the finite volume method with a k-ω SST RANS turbulence, a Volume-of-fluid free surface model and mesh motion with sliding interfaces. The differences were situated in the mesh generation method, the turbulence properties, turbulent wall function, a wave damping method to prevent wave reflection on boundaries and discretization schemes. The schemes in Comet are also very similar to OpenFOAM and StarCCM+, it only differs in the use of the k-ϵ RNG turbulence model and the mesh morphing method. The Comet software does not have its own mesh generation procedure, but is able to use OpenFOAM meshes.

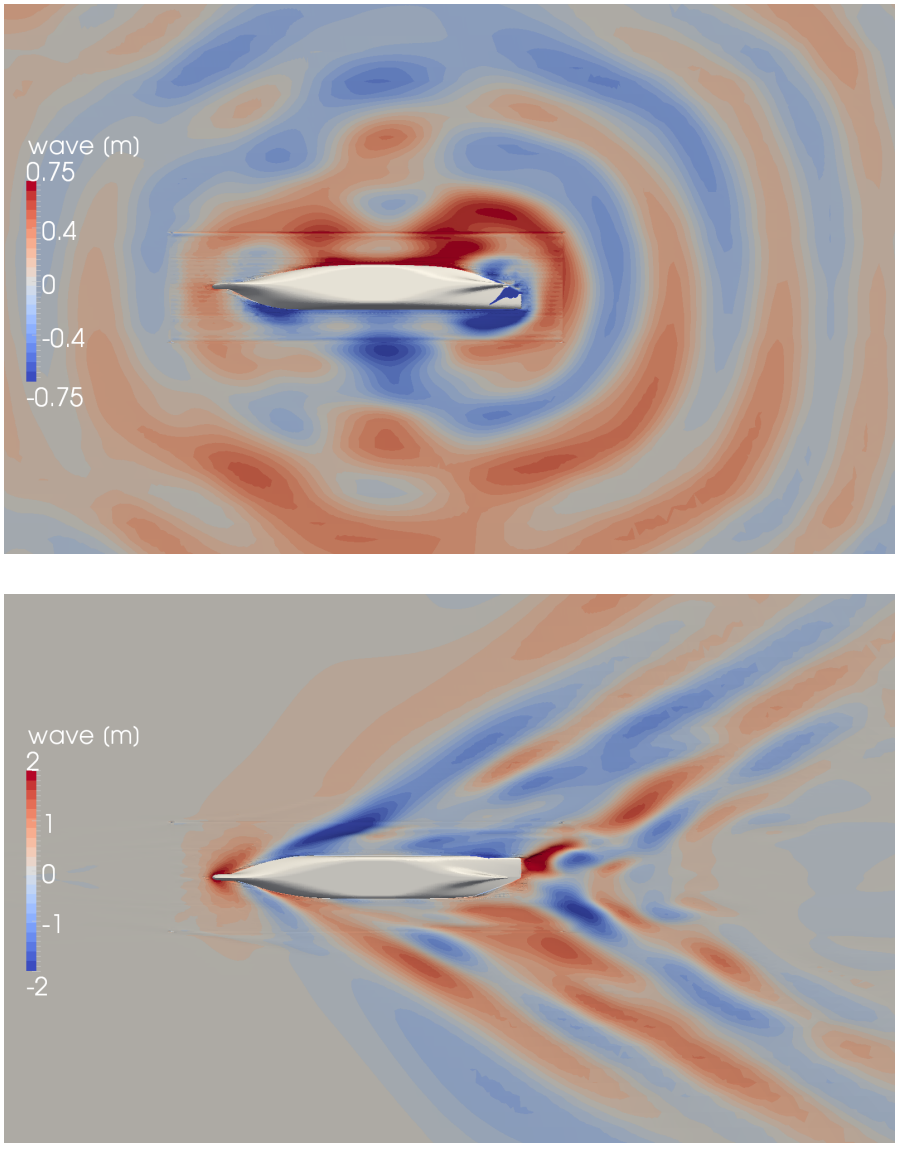

Figure 5.13.: Waves emitted from a rolling DTC hull; top: U=0.0m/s and bottom U=12.86m/s

To assess the comparability of the three flow solver they were each used to compute a number of roll damping cases with the same parameter set P_α. They all used a similar simulation setup and the OpenFOAM and Comet simulations were conducted on the same mesh. Table 5.3 shows the resulting damping coefficients for several test cases. The cryptic name in the left column denotes the alpha-numeric string that was used as an unique identifier for the parameter sets. For example `dS1D3a1643` denotes the DTC hull in its base shape with draft $T = 14m$, without appendages, roll axis hight $raz = 0.0m$, design velocity $U = 25kn$, roll period $T_{\text{roll}} = 25.8s$ and a roll angle amplitude $\phi_A = 20°$. The results in Tab. 5.3 were computed using the maximal design speed and are all relatively high and close together. In the case of zero forward speed the damping coefficients show a stronger variation between the different solver, but still show a good agreement. That is especially noteworthy for the results of the Comet solver, since it uses another turbulence model and the mesh morphing method instead of the sliding interface method.

With the development of the computation framework for the automated simulation and the use of the more stable OpenFOAM-2.1.1 solver version the bulk amount of the remaining simulations were conducted with OpenFOAM. Overall 800 3D roll damping simulations (each run for about 7 days on 8-12 cores) were conducted for variations of ship size, shape, appendages, draft, roll axis, ship velocity, roll period and roll amplitude.

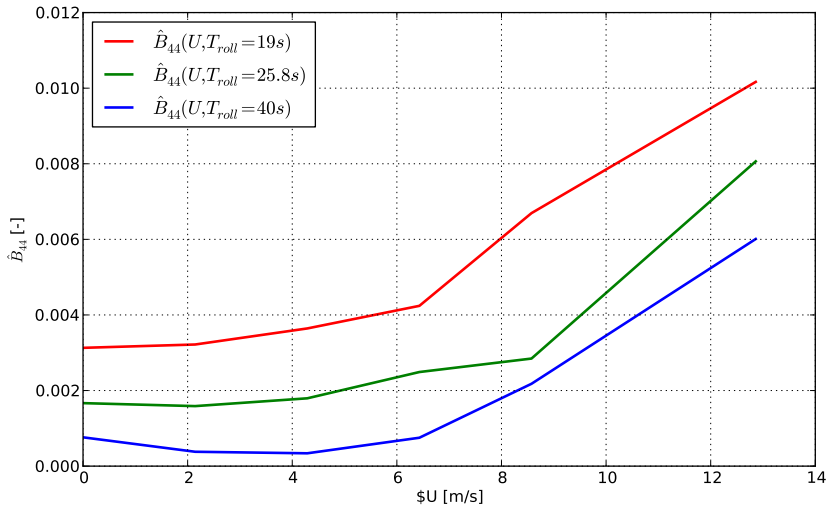

Figure 5.14.: DTC base shape, dimensionless linear damping coefficient $\hat{B}_{44}$ over ship speed U for different roll periods T_{roll}

Figures 5.14 - 5.16 show a summary of the damping coefficients computed with the 3D forced motion simulation case. Although the line plots only allow to investigate the dependency of the damping coefficient from one variation parameter (or two, using multiple lines), they indicated the principle roll damping behavior.

Figure 5.14 shows the increase of the roll damping, depending on the ship velocity. The nonlinear behavior of the plotted lines indicate that the velocity dependency could also be be modeled with a linear plus quadratic term.

Figure 5.15 shows the influence of the roll angle amplitude ϕ_A on the damping coefficient $\hat{B}_{44}$ for zero forward speed. The damping coefficient (plotted for three different roll periods) depends linearly on the roll amplitude with a slightly nonlinear increase towards large roll angles. In the case of the longest roll period $T_{\text{roll}} = 40\text{s}$ the damping coefficient stays almost constant over the whole range of roll amplitudes. The roll damping behavior shown in this figure allows to derive a first guess for the unknown mathematical damping model. The damping contribution of the roll angle amplitude will probably be composed of a linear term plus a weaker quadratic term. The diminishing influence of the roll period may be modeled with an additional hyperbolic term.

Figure 5.16 also shows the damping coefficient $\hat{B}_{44}$ over roll period T_{roll} and roll angle amplitude ϕ_A, but in a different arrangement and for the DTC hull at design velocity. The falling slope of the lines confirms the guessed hyperbolic dependency on the roll period.

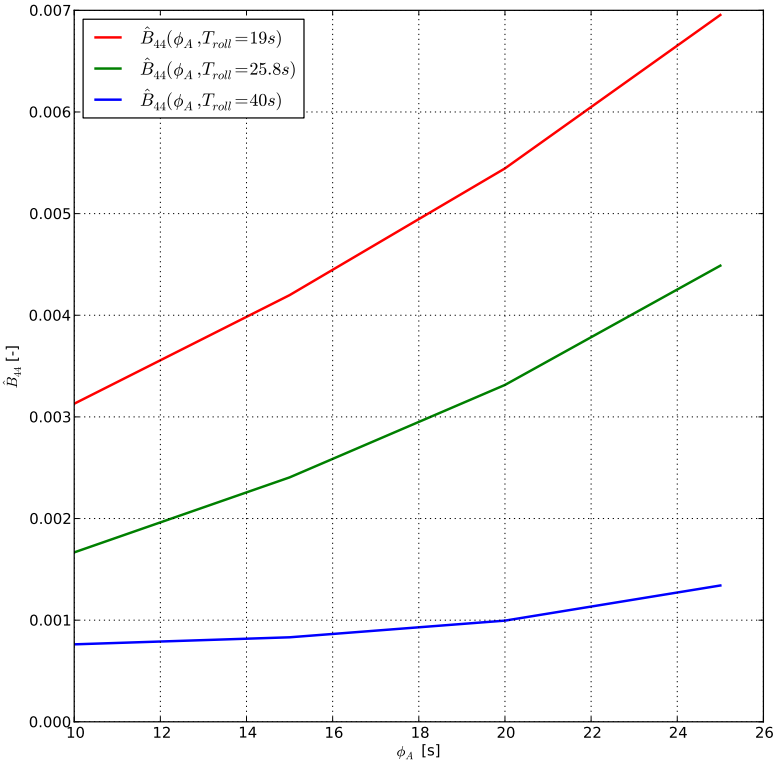

Figure 5.15.: DTC hull at $U = 0.0\frac{m}{s}$; dimensionless linear damping coefficient $\hat{B}_{44}$ over roll angle amplitude ϕ_A for different roll periods T_{roll}

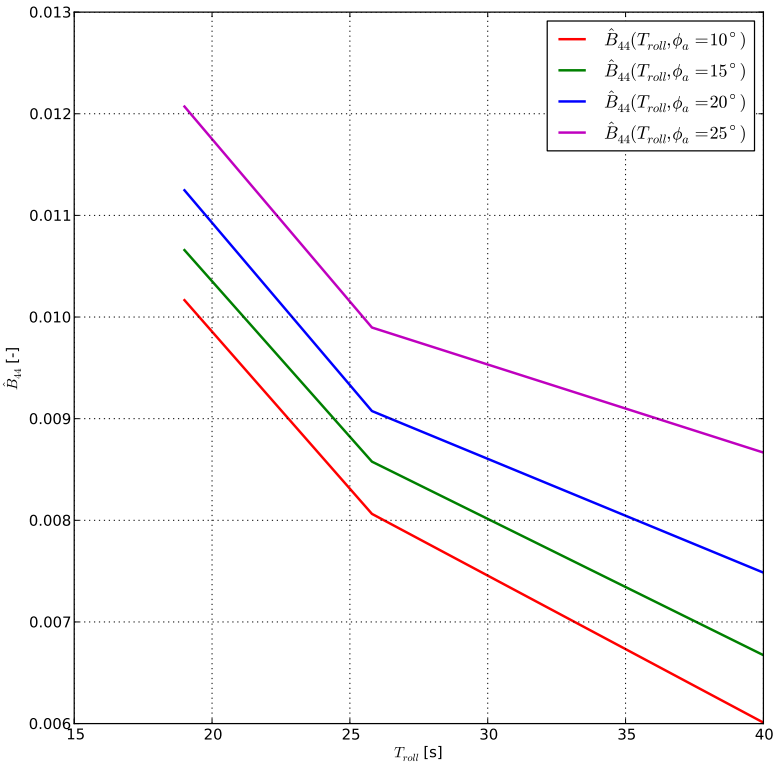

Figure 5.16.: DTC hull at $U = 12.86\frac{m}{s}$; dimensionless linear damping coefficient $\hat{B}_{44}$ over roll period T_{roll} for different roll angle amplitudes ϕ_A

5.3. Damping Prediction

The regression analysis is the final component of the computational framework, that was implemented for the development of a mathematical roll damping model. The methods described in the following section combine the input data and computational results stored in a hydrodynamic database to derive a mathematical expression for the dependency between hull shape and roll damping. Before applying the regression analysis the structure of the unknown damping model has to be further specified. In section 5.1 the generation of the $i \in 1 \dots n$ roll damping test cases was described.

Each parameter set $P_{\alpha,i}$ contains a value for ship speed U_{ship}, roll period T_{roll}, roll amplitude ϕ_A, height of the roll axis raz, beam B_{ship}, draft T, bilge radius R (or alternatively main frame coefficient C_M) and Boolian values (BK $= 1 \rightarrow$ with bilge keel, else without) for the bilge keel BK and rudder rudder.

For each parameter set $P_\alpha = [U_{\text{ship}}, T_{\text{roll}}, \phi_A, \text{raz}, B_{\text{ship}}, T, R, \text{BK}, \text{rudder}]$ a numerical forced roll motion test (Sec. 5.2) and a time series analysis (Sec. 3.2) conducted.

The goal of the regression analysis is to find an expression for $B(P_\alpha)$ that correlates the variation parameter $P_{\alpha,i}$ to the roll damping coefficient B_i:

$$B_i \propto P_{\alpha,i} \rightarrow B(P_\alpha) \tag{5.2}$$

The approach (see Sec. 5.1) to reduce the number of necessary simulations by separating kinematic and geometric parameter, allows to divide the damping model into a product of two sub-models:

$$B(P_\alpha) = B_{\text{geo}}\left(\text{raz}, B_{\text{ship}}, T, R, \text{BK}, \text{Ruder}\right) \cdot B_{\text{kin}}\left(U_{\text{ship}}, T_{\text{roll}}, \phi_A\right) \tag{5.3}$$

The term $B_{\text{kin}}()$ models the nonlinear influence of velocity U, roll period T_{roll} and roll amplitude ϕ_A. The term $B_{\text{geo}}()$ accounts for the roll damping contribution depending on the hull shape and is used to scale the kinematic damping part to fit the total roll damping.

5.3.1. Polynomial Regression

For the determination of the sub-model $B_{\text{kin}}\left(U_{\text{ship}}, T_{\text{roll}}, \phi_A\right)$ the method of multiple linear regression was used. The term *multiple* denotes the existence of multiple input variables (in this case three). The problem of computing the unknown correlation function (5.2) can be approached by reformulating the problem into an over-determined system of linear equations:

$$\underbrace{\mathbf{b}}_{n\times 1} = \underbrace{\mathbf{P}}_{n\times m} \times \underbrace{\boldsymbol{\beta}}_{p\times 1} + \underbrace{\boldsymbol{\epsilon}}_{n\times 1} \tag{5.4}$$

The column vector $\mathbf{b}$ is the so called *dependent variable* or response vector. The term *variable* is somewhat misleading since $\mathbf{b}$ is constant during the regression analysis. It depends on a *independent variable* which is in this case the matrix $\mathbf{P}$ that contains on n rows the parameter sets $P_{\alpha,i}$ with each m columns. The unknown *regression coefficients* are stored in $\boldsymbol{\beta}$ and $\boldsymbol{\epsilon}$ contains the error. The ith line of this system of equations reads:

$$b_i = \beta_1 p_{i,1} + \beta_2 p_{i,2} + \beta_3 p_{i,3} \tag{5.5}$$

A nonlinear transformation of the regression variables $p_{i,j}$ allows to use a linear regression analysis method to determine a nonlinear damping model. Equation (5.6) shows the sub-model for the kinematic parameter that resulted in the best *fit* between model equation and input parameter. The notation in this equation uses the actual variation parameter U_{ship}, T_{roll} and ϕ_A instead of the $p_{i,j}$ entries used for the matrix $\mathbf{P}$ in Eq. (5.5).

$$B_{\text{kin}}\left(U_{\text{ship}}, T_{\text{roll}}, \phi_A\right) = \beta_1 \frac{1}{T_{\text{roll}}} + \beta_2 \frac{1}{T_{\text{roll}}^2} + \beta_3 U_{\text{ship}} + \beta_4 {U_{\text{ship}}}^2 + \beta_5 \phi_A + \beta_6 \phi_A^2 \tag{5.6}$$

The regression model (5.6) is still linear in its coefficients $\boldsymbol{\beta}$, only the variables U_{ship}, T_{roll} and ϕ_A are nonlinear, this type of transformation is termed *polynomial regression*. Besides the linear (U_{ship}), quadratic (${U_{\text{ship}}}^2$) and hyperbolic terms ($\frac{1}{T_{\text{roll}}}$) in Eq. (5.6), it is also common to use logarithm, cubic and root functions to express a nonlinear dependency in the regression model.

The theory of the solution of the above defined regression problem is described in the works of Bühlmann [88] and Hastie et al. [89]. The numerical methods for the computation of the unknown regression coefficients can be found by Venables and Ripley [90].

As mentioned before the procedures for the selection of data, regression analysis and post-processing of the results implemented in the computational framework. To investigate only certain parameter intervals, database filter routines were used to select sub sets of the hydrodynamic database. In some cases the experimental results were faulty or the numerical simulation produced *unphysical* results, it was necessary to remove these statistical outliers by applying the filtering also on the damping coefficients. The numerical solution of the regression analysis was done within python by using an programming interface (python-API `RPy` [91]) to the statistical toolbox `R` [92]. `R` is an open source toolbox that allows to model and solve complex statistical problems.

5.3.2. Model Selection

Once the six β_i regression coefficients of Eq. (5.6) were computed with the above described polynomial regression method, the kinematic damping model

$B_{\text{kin}}(u, T_{\text{roll}}, \phi_A)$ could be used during the second step in the development of the full roll damping prediction model.

A specific requirement in the development of the roll damping model was to find a *mathematical* relationship between roll damping behavior and hull shape. This mathematical model allows a better insight into the physical principles of roll damping than other roll damping prediction methods that just fit a very flexible model with many coefficients to the input data, although these methods often result in a better fitting performance. In order to a derive physically meaningful mathematical expression of the geometric sub-model $B_{\text{geo}}(\text{raz}, B_{\text{ship}}, T, R, \text{BK}, \text{Ruder})$ and finally the full model $B(P_\alpha)$, a different approach was used.

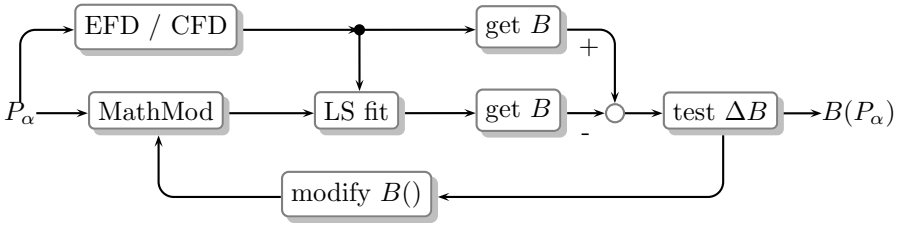

Figure 5.17.: Development procedure for the mathematical roll damping model

To select the best suited damping model, the regression analysis is embedded in the iterative process shown in Fig. 5.17. The process begins on the left side with the definition of the variation parameter P_α. The upper thread/path begins with the generation of the roll motion time series with either experimental or numerical methods. Followed by the application of time series analysis methods in order to obtain the damping coefficients (*get B*).

In parallel, an initial mathematical damping model is fitted to the time series data with the use of a least squares method (*LS fit*). This mathematical model and the variation parameter are used to compute an artificial roll motion time series, for which the damping coefficients are also determined. Next the damping coefficient (or multiple coefficients if higher order damping terms are considered) from the mathematical model is subtracted from the damping coefficient that was derived from the experimental tests or numerical simulation. In the *test* ΔB block, the prediction quality of the mathematical damping model is analyzed and either the current model meets the requirements and the model is approved, or the damping model is modified and the whole procedure is repeated with the improved model.

The development process for the full damping model can be best explained with the final roll damping equation itself. Equation (5.7) shows the mathematical model for the linear damping coefficient that produced the best fit to the input data.

$$\hat{B}_{44}(P_\alpha) = c_1 \left(\frac{B_{\text{ship}}}{2(T + \text{raz})} \right)^2 \left(\frac{1}{1 - C_M} \right) (B_{\text{kin}}(u, T_{\text{roll}}, \phi_A) + c_2) \tag{5.7}$$

Instead of using more regression coefficients and a polynomial expansion as in the previous paragraph (Eq. (5.6)), only two more coefficients c_1 and c_2 were introduced to the full damping model. These coefficients are used to scale (c_1) and shift (c_2) the kinematic sub-model B_{kin} in order to fit the full model to the input data. The geometric sub-model is only composed of shape parameter (in this case beam, draft, roll axis and main frame coefficient) without further unknown coefficients. The objective for the development of the geometrical sub-model was to find a mathematical expression for the damping by using only these given shape parameter.

By combining the variation parameter, instead of using independent polynomial terms, the resulting model is composed of nonlinear coupled variables. This type of nonlinear behavior could not be processed with the polynomial regression method that was used before, but was solved with the method of the least squares (Sec. 3.2).

In addition to the variation parameter in P_α the ship coefficients were stored in the database (see Sec. 5.1) as well. This allows to use any of the available coefficients in the regression analysis. The only restriction is that the used regression variables are independent of each other. For example draft and beam can be used, but not in connection with the beam-to-draft ratio.

The influence of the hull shape is modeled in Eq. (5.7) by a combination of beam B_{ship}, roll axis raz, draft T and main section coefficient C_M. The structure of the equation can be explained geometrically: The term in the first brackets defines the ratio between width and height of the rolling object. Figure 5.4 shows an example of this shape variation. A ratio of one means that the distance of the roll axis to the sides of the hull and the base line is equal, which results in a low damping coefficient. If the the ratio becomes large or smaller, the damping increases.

The term in the second brackets is used to model the influence of the bilge radius. A small bilge radius (and thereby large main frame coefficient) results in a large damping coefficient. The damping of the bilge radius strongly depends on whether a bilge keel is present or not.

The bilge keel parameter is not included in the damping equation (5.7) because of two reasons: The damping contribution of the bilge keel is mainly pressure dominated and can be sufficiently captured with methods using either the K-number (see Sec. 4.2.3) or the Ikeda component for the bilge keel (see appendix A.1). Secondly the addition of a bilge keel leads to a sudden, non-continuous increase of the roll damping which cannot be captured adequately with the smooth, continuous damping model used in Eq. (5.7). The influence of the rudder is similarly difficult to model, because of the complex flow conditions and variable rudder angle.

5.3.3. Model Evaluation

There are several ways to evaluate the quality of the new roll damping model. The simplest one is to compare the numerical values of the damping coefficient obtained from different methods. This approach allows to compute the exact deviation of the mathematical model from the input data, but does not provide insight into the principles of roll damping or the overall performance of the damping model.

Table 5.4.: Comparison of the roll damping coefficient $\hat{B}_{44}$ for OpenFOAM, Ikeda method and the new damping prediction method for the DTC hull at zero velocity

$\hat{B}_{44}$	OpenFOAM	Ikeda	math. model
dS1D3a1031	0.00313	0.00373	0.00300
dS1D3a1032	0.00498	0.00414	0.00382
dS1D3a1033	0.00544	0.00455	0.00472
dS1D3a1034	0.00695	0.00497	0.00663

Table 5.4 shows numerical values of the roll damping coefficient obtained from OpenFOAM simulations, the Ikeda method and the new damping model. Because the Ikeda component method only allows to predict the roll damping for zero forward speed the table only contains cases for $U = 0$. The table lists the roll damping coefficient $\hat{B}_{44}$ for four different roll angle amplitudes $\phi_A = (10°, 15°, 20°, 25°)$ at the intermediate roll period $T_{\text{roll}} = 19[s]$.

The results show a good agreement if it is taken into account that the roll damping at zero speed and without bilge keels is relatively small and suffers a high fluctuation. The trend of the results towards larger roll angle amplitudes show that the damping coefficient for the CFD results and the derived mathematical model have a stronger increase than the Ikeda method. This difference results from the fact that Ikeda only considered relative small roll angle in his prediction method while the new model captures a larger range up to $\phi_A = 25°$.

In addition to the numerical values, the properties of the new damping model can be investigated by studying the prediction results of the whole database. The figures 5.18, 5.19 and 5.20 show the damping coefficients with respect to the parameter sets P_α, obtained from both the numerical simulation and the new damping model. The black plus signs indicate the results from the time series analysis and the red point-symbols are the results computed with the damping model. To illustrate the deviation of the mathematical model from the numerical results the damping values belonging to the same parameter set are connected with a blue

line. The damping coefficients in these three figures provide an overview of the limits within which the roll damping varies, depending on the parameter.

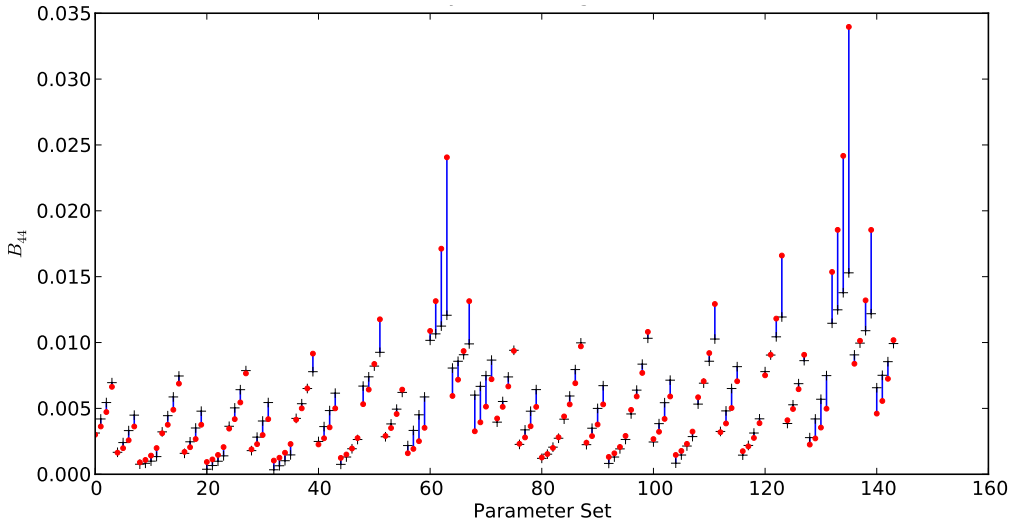

Figure 5.18.: Comparison of the results from the CFD simulations and the new damping model for the 3D DTC hull; linear damping coefficient for 144 simulation cases, black plus sign indicate results from times series analysis, red dots indicate results from the damping model

Figure 5.18 shows the results of all parameter variations within the kinematic variation subset for the 3D DTC base shape. The first 72 of the 144 cases were conducted without a bilge keel, the remaining cases with segmented bilge keel. An added bilge keel may increase the roll damping up to 30% which is much less than the increase in 2D simulation, but still considerably high for the relative small bilge keel (compared to the hull size). Another effect that can be observed in Fig. 5.18 is a strong overshot of the predicted damping for the case, when large roll angle amplitudes were combined with short roll periods and a high ship speed. This effect originates from the superposition of the influence of the kinematic variation parameter (Eq. (5.6)). The new damping models fails to capture this smaller damping increase at these extreme parameter conditions (eg. a 360m ship rolling with $\phi_A = 20°$ while moving at $U = 25$kn), but since these conditions are highly unrealistic, these outliers can be neglected.

The results shown in figure 5.19 and 5.20 were obtained from the 2D roll simulations of the DTC main section, where the influence of the bilge keel is much more significant. The hull section with a bilge keel attached (Fig. 5.19) has a five to ten times higher roll damping than without (Fig. 5.20). This effect originates from the blocking effect described in Sec. 4.2.3 and shows the main drawback of 2D simulations. Despite this flaw, the analysis of 2D simulations allows to investigate

the principle functional relationship between roll damping and hull shape and by using a quantitative measure for the deviation, the 2D results can be incorporated into the damping model.

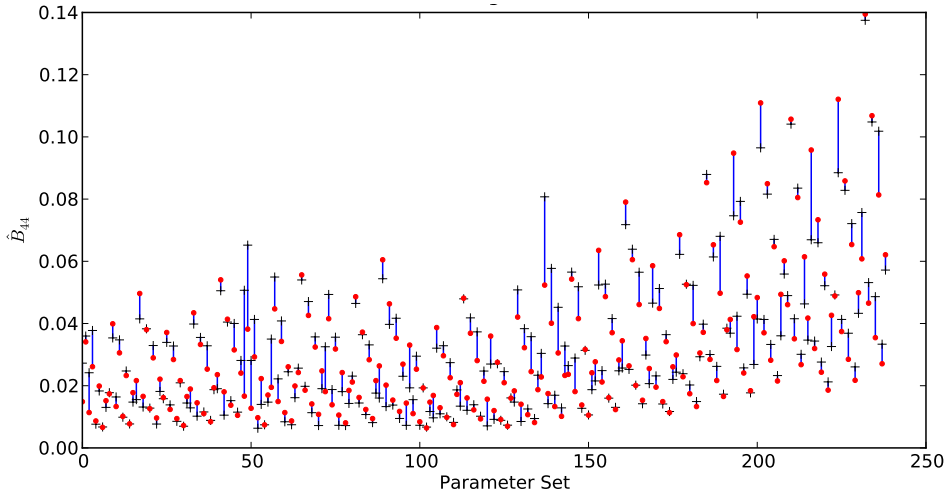

Figure 5.19.: Comparison of the linear damping coefficients from the CFD simulations (black plus sign) and the new damping model (red dots) for the 2D DTC main section **with** bilge keels; 240 2D simulation cases

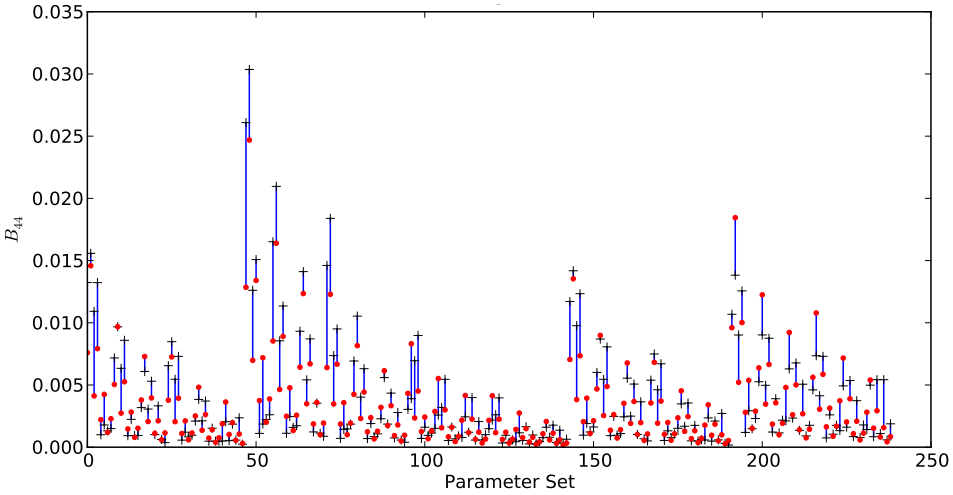

Figure 5.20.: Comparison of the linear damping coefficients from the CFD simulations (black plus sign) and the new damping model (red dots) for the 2D DTC main section **without** bilge keels; 240 2D simulation cases

6. Conclusion

The aim of this thesis is the investigation of the roll damping behavior of modern ship hulls and the development of a mathematical model for roll damping prediction. After an introduction to the thesis topic, the a chapter on the theoretical background and an overview state of the art of roll, the main part is presented. The methodology part is divided into three chapter: the development procedure of the mathematical model (Chap. 3), the numerical simulation of viscous roll damping (Chap. 4) and the application of a regression analysis method (Chap. 5).

In this final chapter the approach and main steps to achieve this aim are briefly summarized, followed by a discussion of the contributions made to the research area of roll damping analysis and an assessment of the limitations of the developed methods. The last paragraph concludes with an outlook on further research in the field of roll damping analysis.

Summary

The general concept for the development of the mathematical roll damping prediction model was to vary the hull shape, determine the damping coefficient from numerical roll motion simulations and then find a functional relationship that correlates the damping coefficients with the shape parameter. To accomplish this development task, a computational framework was developed, that incorporates all the numerical tools, that were implemented in the programming language `python`. The core of the framework is a set of time series analysis routines, that were used to process the time series data obtained from either numerical simulations or model tests, in order to determine the underlying behavior in the form of mathematical equations and model coefficients. These routines had to be robust and versatile enough to handle time series results that were noisy or had a varying sample rate.

Another part of the mathematical model development was a numerical integration algorithm for nonlinear second order differential equations. This solver was used to simulate the roll motion of a ship depending on inertia, damping and restoring coefficients. By comparing the results of the numerical integration with time series data from experiments or numerical field methods, the prediction quality of the damping model could be evaluated.

Chapter 3 concludes with a presentation of the three coefficients – inertia, damping and restoring – that determine the behavior of the roll motion equation. For each coefficient a method was presented that can be used to estimated the numerical value of the coefficient. The damping coefficient was derived from time series data with the described time series analysis methods. The restoring moment and the main ship coefficients were computed using simple hydrostatic equations and the CAD geometry of the hull. To estimate the roll inertia of a 3D hull a 2D potential flow solver in combination with a strip method was developed.

In chapter four, the theory, validation and application of the OpenFOAM CFD toolbox for the simulation of ship roll motion is documented. After a short overview of the governing flow equations, approximation method, turbulence and free surface modeling, mesh generation and setup of an OpenFOAM case, several case studies were presented. These test cases were used to assess and validate OpenFOAM for the use for viscous roll damping simulations. Beginning with simple hull resistance computations, and the simulation of the flow around different bilge keel geometries, the complexity of the test setup was gradually increased until the numerical solver could be validated with the free roll decay measurements that were conducted at the model test basin during the term of the project. Moreover the influence of RANS and LES turbulence models on the time series results and the behavior of vortices 2D and 3D simulations were analyzed.

Based on the results from these case studies, the configuration and mesh generation for the forced motion tests were developed. This type of roll motion simulation was found to be the best suited for the analysis of the systematical shape variations. In the final methodological chapter the use of the previously developed procedures and the application of a regression analysis method was described. In order to process the large number of parameter variations and control the different analysis tools, the developed methods were incorporated into a computational framework that manages all parameters, coefficients and time series in a database and controls the application of the numerical procedures.

The new roll damping model was developed in three stages. First, the database was filled with the variation parameters, that were arranged in such a way that they provide a good compromise between a low number of test cases and an sufficient amount of regression variables. The next step was the most time consuming and computationally demanding. For each set of variation parameters a finite volume mesh and an forced motion case was generated and solved with OpenFOAM. Afterwards the time series analysis method was used to extract the roll damping coefficients. In the final phase the regression analysis method was applied to the variation parameter and the damping coefficients, both stored in the database.

Contributions

The development of the mathematical roll damping model defined in Eq. (5.7) is the central result of this thesis. This equation can be used to predict the roll damping of a container ship whose hull shape and motion parameter are within the investigated range. This prediction method has been compared against the Ikeda method and the OpenFOAM CFD results. Furthermore, the mathematical expression provides the information of how the roll damping depends on the hull shape in a quantitative way, by the numerical value of the coefficients and in a qualitative way, by the polynomial order or nonlinearity of the shape variables. The sensitivity of the roll damping to a change of the hull shape can be tested by varying the according parameters in Eq. (5.7).

Parallel to the development of the roll damping prediction model the objective was to investigate roll damping in general and to gain a deeper insight into the fluid dynamics of a rolling ship hull. This has been done throughout the entire thesis, beginning with the 2nd chapter, where the physical principles of roll motion and a review of the current roll damping simulation, measurement and prediction methods were presented. In chapter 3 the effect of higher order damping terms, large roll angle amplitudes and nonlinear restoring moments were discussed.

The case study in Sec. 4.2.3 showed how the roll damping of a bilge keel in a 3D test setup deviates from pure 2D cases. The influence of a bilge keel was further investigated in Sec. 4.3.1 with a variation of the bilge keel size and in Sec. 4.3.2 with different geometries of the bilge keel tip.

To accomplish the main goal of this thesis several tools had to be developed: A set of time series analysis methods were designed and implemented in order to derive the roll damping coefficients from measured or computed roll motion data. These tools can be used to analyze every type of roll motion measurements and allow to determine the model parameters of any harmonic time series in general. The model parameters can be used combination with the numerical solution routine developed in Sec. 3.1, to simulate the roll motion of a ship and to test the quality of a new damping model.

The set of hydrostatic routines, described in Sec. 3.4, can be used to analyze the CAD file of arbitrary ship hulls and generate a data sheet containing hull parameter, shape coefficients, ship lines and plots of the nonlinear restoring moment. Another tool implemented in connection with the hull shape analysis is the bilge keel CAD designer (Sec. A.5). This program can be used to generate a parametric bilge keel geometry that is aligned to the surface of the hull and oriented by the stream lines along the hull.

Part of the motivation to develop a new roll damping prediction model were the limitations of the Ikeda method. Especially the simple Ikeda method described in Sec. A.4 is restricted to slender hull shapes and zero ship velocity. The principle

damping effects of the empirically and analytically modeled damping components on the other hand are still valid. The Ikeda method could be extended in a similar way as it has been done by Tamiya [52] to include the forward speed (Sec. A.1). By coupling the simple Ikeda method with the method for the inertia coefficient (Sec. 3.5) the limitation to slender bodies or externally obtained shape coefficients could be removed. Furthermore, the method could be linked to hydrostatic routines, to include a nonlinear restoring moment.

Limitations

The application of the new damping model is subject to certain limitations: Although the systematic parameter variation was designed to cover many parameter over a wide range, these parameter represent only a small part of the parameter that influence the roll motion behavior. The prediction of the roll damping for a hull design that lies outside the investigated parameter-domain may result in wrong estimates.

In section 5.1.3 the necessary reduction of the number of test cases was described. This reduction had the effect that the number of the regression points for specific parameter variations were too sparse to derive model terms with higher order. In these cases a linear model was used, fitted to only three points. This approach made it possible to include these *sparsely* distributed parameter at all, but nonlinear effects cannot be captured and outliers in the database have a severe impact on the prediction model.

All experiments and numerical simulations were conducted with calm water conditions, that means the influence of the sea state was not taken into account, although it has a significant influence on the roll motion and therefore also on the roll damping.

Outlook and Recommendations

Some flaws in the presented development method should be addressed if the prediction model is to be further improved. To circumvent the sparse distribution of regression points either the number of test cases has to be significantly increased or the number of variation parameter has to be reduced.

Another approach would be to increase the number of test cases and thereby the quality of the prediction model to improve the efficiency of the numerical simulation. If the setup of a test case could be further simplified and the computational costs reduced, it would allow to conduct more simulations.

At a certain level of computational efficiency, it should be possible to conduct viscous roll damping simulations even in the design phase. Such individual tests

would allow to understand more directly if and how a change in the hull design influences the roll damping.

As mentioned in the previous paragraph, the influence of the sea state was not considered. This is also true for the rudder motion, for which the roll decay tests in Sec. 4.2.5 showed a great influence. In future investigations the effect of waves and the rudder angle should be included.

With respect to the numerical treatment of the turbulent boundary layer at an oscillating wall, more basic research is needed. The combination of a high Reynolds number flow with a cyclic changing cross flow is quite unique and not covered by the turbulent wall functions that were used in the RANS simulation. With a more thorough physical understanding of the viscous friction of an oscillating wall the roll damping model could be greatly improved and the simulation methods extended with a more realistic wall function that incorporates the turning point of the oscillation.

A. Appendix

A.1. Ikeda's Damping Components

This section presents a detailed summary of Ikeda's approach to split the total roll damping coefficients into a sum of components that are related to different flow effects and model damping components. For this purpose the article *Prediction of Ship Roll Damping – State of the Art* published in 1981 by Himeno [45] is described in more detail.

Friction Damping

The friction component B_F results from the friction between fluid and ship hull and has a linear dependency on the roll angle amplitude and the angular velocity.

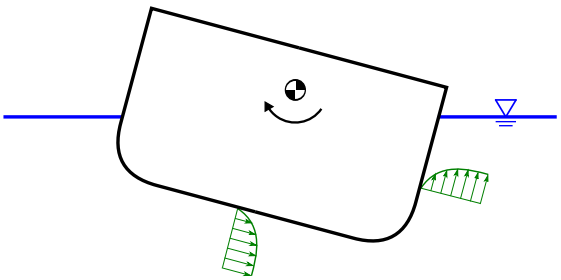

Figure A.1.: Tangential damping forces

The friction component B_F consists of the coefficient B_{F0} for zero forward velocity and a multiplicative factor that takes the ship velocity into account.

$$B_{F0} = 0.787\rho r_S^2\sqrt{\omega\nu}\left(1 + 0.00814\left(\frac{r_s^2\phi_A^2\omega}{\nu}\right)^{0.386}\right) \tag{A.1}$$

The following equations depend on the ship length L, the draft d, the breadth B, the block coefficient C_B, the position of the center of gravity OG, the kinematic viscosity ν, the fluid density ρ, the angular velocity ω, the roll angle amplitude ϕ_A and an estimate for the wetted surface area of the hull S.

$$S = L\left(1.7d + C_B B\right) \tag{A.2}$$

The radius r_S is the mean distance between the hull surface and the roll axis.

$$r_S = \frac{1}{\pi}\left((0.887 + 0.145C_B)\,\frac{S}{L} - 2OG\right) \tag{A.3}$$

Without the influence of the forward velocity the friction damping is considered to be linear. Tamiya [52] developed an empirical equation from his model test with elliptical hull shapes that allowed to extend the equation for the friction damping to include the forward velocity.

$$B_F = B_{F0}\left(1 + 4.1\frac{U}{\omega L}\right) \tag{A.4}$$

Equation A.4 scales the friction damping proportional to the K-number. The friction damping increases strongly with increasing ship velocity and is the only damping component that shows a scale effect proportional to $1/\lambda^{0.75}$ (λ is the model scale).

The linear coefficient for zero velocity are independent of the scale effect (Himeno [45]). Ikeda mentions in [41] that the proportion of the zero velocity friction damping to the total damping can be neglected for full scale ships. Due to the scale effect, for model scale damping prediction the zero velocity friction coefficient has to be taken into account.

Eddy Damping

The roll damping due to eddies shed from the ship hull is another nonlinear component of the total damping coefficient. The eddy damping is attributed to the B_2 coefficient of equation (2.11). Figure A.2 shows the principle effect how eddies detach from blunt edges (small bilge radii, bilge keel or forward and aft section) of the ship hull due to roll motion. After the point of separation these eddies generate a low pressure region on the ship hull that counteracts the roll motion of the hull. This effect is modeled in the eddy damping component B_E and depends on the motion parameter ϕ_A and ω.

The eddy damping component B_E is a combination of the zero forward velocity coefficient B_{E0} and a multiplication factor depending on the ship velocity. The eddy damping can be estimated indirectly from the hull shape. A strip method or a potential flow method is used to compute the shape coefficients which are then used to compute the eddy damping.

Equation (A.5) defines the zero velocity eddy damping depending on the above defined motion and hull parameter and a function $F()$ which is a placeholder for the method that is used to obtain the shape coefficient. The method $F()$ depends

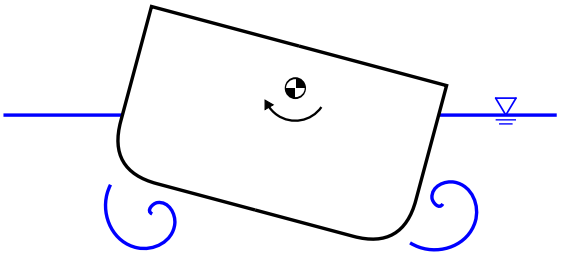

Figure A.2.: Eddy separation

on the draft d, bilge radius R, the half of the breadth-beam quotient H_0, the area coefficient σ and the center of gravity OG.

$$B_{E0} = \frac{4}{3\pi}\rho d^4 \omega \phi_A \left(\frac{r_{\max}}{d}\right)^2 F\left(\frac{R}{d}, H_0, \sigma, \frac{OG}{d}\right) C_P \tag{A.5}$$

At increasing forward velocity the eddies are transported downstream of the hull and their the influence on the eddy damping decreases. If bilge keels are attached to the hull their eddies are account to the bilge keel damping component.

$$B_E = B_{E0} \frac{0.04\omega^2 L^2}{U^2 + 0.04\omega^2 L^2} \tag{A.6}$$

Lift Damping

The rolling ship hull causes a circulation flow that generates low and high pressure fields on the hull surface. The roll damping effect that these zones have on the ship motion are attributed to the lift damping B_L.

$$B_L = \frac{\rho}{2} U l d k_N l_0 l_R \left(1 - 1.4\frac{OG}{l_R} + \frac{0.7OG}{l_0 l_R}\right) \tag{A.7}$$

In addition to the previously defined parameter the equation depends on the factor k_N:

$$k_N = 2\pi\frac{d}{L} + \kappa\left(4.1\frac{B}{L} - 0.045\right) \tag{A.8}$$

and $l_0 = 0.3d$ and $l_R = 0.5d$. The lift damping coefficient (A.7) is proportional to the ship velocity and independent of the roll period.

Wave Damping

Part of the kinetic energy in the roll motion of the ship hull is converted into water waves. The energy loss due to this wave emission is termed wave damping and can be estimated by the mechanical work done by the ship hull. Figure A.3 shows the outline of a rolling cross section. The red arrows indicated the motion of the hull surface which generates the water waves.

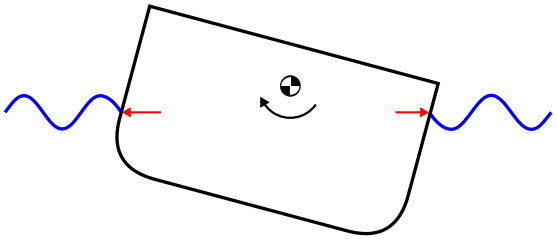

Figure A.3.: Wave radiation

Instead of using the area moment of inertia Ikeda simplified the rotation to a translation and used the drag coefficient for a sway motion. This lateral drag coefficient N_S can be computed for each cross section with the strip method. The wave damping component for zero forward velocity is approximated by multiplying the linear coefficient with the lever $l_W - OG$ (distance between center of gravity and the point of application of the fluid force).

$$B_{W0} = \rho N_S \left(l_W - OG\right)^2 \tag{A.9}$$

For non-zero ship velocity the influence of the wave system around the ship hull has to be included. For this purpose Ikeda used a potential flow method where the ship was modeled with dipole sources. With the results from the potential method and experimental data Ikeda derived an empirical equation for the wave damping B_W.

$$\frac{B_W}{B_{W0}} = 0.5\left(\left(A_2+1\right) + \left(A_2-1\right)\tanh\left(20\tau - b\right)\right) + \left(2A_1 - A_2 - 1\right)e^{-150(\tau-0.25)^2} \tag{A.10}$$

The coefficients used in equation (A.10) are determined with the following definitions:

$$\begin{aligned} A_1 &= 1\zeta_d^{-1.2}e^{-2\zeta_d} \\ A_2 &= 0.5 + \zeta_d^{-1}e^{-2\zeta_d} \\ \zeta_d &= \omega^2\frac{d}{g}, \quad \tau = \frac{U\omega}{g} \end{aligned} \tag{A.11}$$

Bilge Keel Damping

Figure A.4 shows the outline of a rolling cross section with bilge keels and the flow effects that occur around the bilge keels.

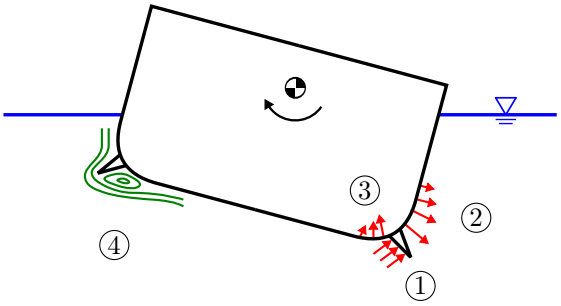

Figure A.4.: Flow effects at the hull surface and bilge keel

In general the roll damping influence of the bilge keels can be divided into two independent components: The normal damping component B_N ① (indicated by the red arrows) acting on the bilge keel area projected in normal direction of the flow. And the normal damping component B_S acting on the hull surface before ③ and behind ② the bilge keel. The high pressure area in upstream direction of the bilge keel is generated by the stagnation pressure of the bilge keel. The low pressure region downstream of the bilge keels is generated by the flow separation at the bilge keel tip ④.

$$B_{BK} = B_N + B_S \tag{A.12}$$

The drag force F_D on the projected area of the bilge keel can be computed with:

$$F_D = C_D \frac{1}{2} \rho A |u| u \tag{A.13}$$

depending on the drag coefficient C_D, the projected area of the bilge keel in directions of the flow A and the flow velocity u in normal direction to area A.

In a steady flow condition the drag coefficient is constant. For oscillating flows the drag coefficient can be defined as a function of the K-number. A bilge keel with the width b_{BK}, the length l_{BK} and a distance r_{BK} to the roll axis, that is oscillating with the roll amplitude ϕ_A and roll period $T = \frac{2\pi}{\omega}$, has a maximum velocity of $u = r_{\mathrm{BK}} \phi_A \omega$. Using these parameter the equation for the K-number (4.22) can be brought into a form required for roll motion.

$$KC = \frac{\pi r_{\mathrm{BK}} \phi_A}{b_{\mathrm{BK}}} \tag{A.14}$$

Based on Eq. (A.14) and his experimental data Ikeda derived an empirical equation for the drag coefficient in an oscillatory flow:

$$C_D = 22.5\frac{b_{\mathrm{BK}}}{\pi r_{\mathrm{BK}}\phi_A} + 2.4 \tag{A.15}$$

In 1996 Sarpkaya and O'Keefe [1] conducted two and three dimensional experiments with oscillating bilge keels and confirmed a good agreement between Ikeda's empirical equation (4.17) and their test results. With this equation for the drag coefficient Ikeda derived an equation for the normal damping component of the bilge keel for zero ship velocity:

$$B_{\mathrm{N}_0} = \frac{8}{3\pi}\rho r_{\mathrm{BK}}^2 b_{\mathrm{BK}}^2 \omega f^2 \left(22.5\frac{1}{\phi f} + 2.4\frac{r_{\mathrm{BK}}\phi_A}{b_{\mathrm{BK}}}\right) \tag{A.16}$$

The parameter f is an empirical correction factor for the roll velocity and σ is the area coefficient of the respective ship cross section.

$$f = 1 + 0.3e^{-160(1-\sigma)} \tag{A.17}$$

The damping component B_{N_0} is a nonlinear coefficient corresponding to B_2 in equation (2.11) (Ikeda [41]). If the bilge keel damping for a ship with forward velocity is required an additional linear coefficient proportional to the forward velocity can be used.

$$B_{\mathrm{N}} = B_{\mathrm{N}_0} + \frac{\pi}{2}\rho b_{\mathrm{BK}}^2 r_{\mathrm{BK}}^2 U \tag{A.18}$$

The additional coefficient in the damping component B_{N} (A.18) is independent of the roll amplitude or roll period and its dependency on the forward velocity is linear.

Schmitke [14] used a similar approach but with the difference that his nonlinear component decreases slightly for forward velocity. Fujino [93] used another more extensive approach to include the influence of the forward velocity by using the lift theory for thin wing sections.

The bilge keel damping component on ship hull B_S is computed in a similar way but with the difference that instead of the drag coefficient the lift coefficient is used.

$$F_p = \frac{1}{2}C_P A|u_\phi|u_\phi \tag{A.19}$$

The pressure force F_p depends on the area A on which the pressure acts and the velocity $u_\phi = r_{\mathrm{BK}} f\dot{\phi}$ (with $\dot{\phi}\widehat{=}$ angular velocity of the ship). The pressure coefficient $C_P^+ = 1.2$ and the size of the area upstream of the bilge keel is assumed

to be constant, while the low pressure zone downstream of the bilge keel depends strongly on roll amplitude and roll period.

$$B_{\mathrm{S}} = \frac{4}{3\pi}\rho r_{\mathrm{BK}}^2 d^2 \omega \phi_A f^2 I \tag{A.20}$$

The bilge keel damping on the hull surface is defined by equation (A.20) depending on the surface integral I that has to be computed for area before and after the bilge keel using either C_{PI}^{+} or C_{PI}^{-}.

$$I = \frac{1}{d^2}\int C_{PI} l_{\mathrm{BK}} ds \tag{A.21}$$

with

$$\begin{aligned} C_{PI}^{+} &= 1.2 \\ C_{PI}^{-} &= -22.5\frac{b_{\mathrm{BK}}}{\pi r_{\mathrm{BK}} f \phi_A} - 1.2 \end{aligned}$$

In Himeno [45] the author notes that the damping coefficients B_1, B_2 and B_3 are partially independent of the roll amplitude ϕ_A and that the relation between the coefficients and the harmonic parameter of the roll motion ω and ϕ_A has to be further investigated. He states furthermore that the nonlinear component of the bilge keel damping decreases for large forward velocities while the linear part increases.

A.2. Analytical Solution of a Damped Harmonic Oscillator

In this section the mathematical derivation of an analytical solution of the damped harmonic oscillator (3.5a) is described. The following mathematical procedure uses the Laplace transformation method to find an analytical solution for the second order differential equation.

In the following the free variable is denoted with y (instead of ϕ) and the terms $\omega_0^2 = \Delta\overline{\mathrm{GM}}/I$ and $2\delta_0\omega_0 = B/I$ are used to simplify the equations. The differential equation:

$$\ddot{y} + 2\delta\omega_0\dot{y} + \omega_0^2 y = 0$$

can be mapped into the Laplace domain by using the transformation rules Eq. (A.22a)-(A.22c):

$$\mathcal{L}\{y\} = \Psi(s) \tag{A.22a}$$
$$\mathcal{L}\{\dot{y}\} = s\Psi(s) - y_0 \tag{A.22b}$$
$$\mathcal{L}\{\ddot{y}\} = s^2\Psi(s) - s\,y_0 - \dot{y}_0 \tag{A.22c}$$
$$\mathcal{L}\left\{e^{at}\right\} = \frac{1}{s-a} \tag{A.22d}$$
$$\mathcal{L}\{\sin(at)\} = \frac{a}{s^2+a^2} \tag{A.22e}$$

This operation results in the function:

$$0 = s^2\Psi(s) - sy_0 - \dot{y}_0 + 2\delta\omega_0\left(s\Psi(s) - y_0\right) + \omega_0^2\Psi(s) \tag{A.23}$$

which is solved for $\Psi(s)$:

$$\Psi(s) = \frac{sy_0 + \dot{y}_0 + 2\delta\omega_0 y_0}{s^2 + 2\delta\omega_0 + \omega_0^2} \tag{A.24}$$

In order to determine the solution for $y(t)$, the function has to be mapped back to the time domain. To do so the zero points of the denominator function have to be determined and the expansion into partial fractions has to be computed.

The zero points for a second order polynom are:

$$0 = \quad s^2 + 2\delta\omega_0 + \omega_0^2 \tag{A.25}$$
$$s_{1/2} = \quad -\delta\omega_0 \pm i\omega_0 D \tag{A.26}$$

with $D = \sqrt{1-\delta^2}$.

Using this expression the coefficients A and B in the relation:

$$\frac{sy_0 + \dot{y}_0 + 2\delta\omega_0 y_0}{s^2 + 2\delta\omega_0 + \omega_0^2} = \quad \frac{A}{s-s_1} + \frac{B}{s-s_2} \tag{A.27}$$

can be determined with:

$$A = \frac{y_0}{2} + \frac{\dot{y}_0 + \delta\omega_0 y_0}{2i\omega D} \tag{A.28}$$

$$B = \frac{y_0}{2} + \frac{-\dot{y}_0 - \delta\omega_0 y_0}{2i\omega D} \tag{A.29}$$

The $\mathcal{L}^{-1}$ inverse Laplace transformation back to the time domain can be derived using the mapping rules Eq. (A.22d) and (A.22e) as well as the trigonometric relations:

$$\sin x = \frac{1}{2i}\left(\mathrm{e}^{ix} - \mathrm{e}^{-ix}\right) \tag{A.30}$$

$$\cos x = \frac{1}{2}\left(\mathrm{e}^{ix} + \mathrm{e}^{-ix}\right) \tag{A.31}$$

By inserting the coefficients A and B and applying the above defined relations, an analytical solution for the damped differential equation can be derived:

$$\begin{aligned} y(t) &= Ae^{(-\delta\omega_0 + i\omega_0 D)t} + Be^{(-\delta\omega_0 - i\omega_0 D)t} \\ &= e^{-\delta\omega_0 t}\left(\frac{y_0}{2}\left[e^{i\omega_0 Dt} + e^{-i\omega_0 Dt}\right] + \left(\frac{\dot{y}_0}{2i\omega_0 D} + \frac{\delta y_0}{2iD}\right)\left[e^{i\omega_0 Dt} + e^{-i\omega_0 Dt}\right]\right) \\ &= e^{-\delta\omega_0 t}\left(y_0 \cos(\omega_0 Dt) + \left(\frac{\dot{y}_0}{\omega_0 D} + \frac{\delta y_0}{D}\right)\sin(\omega_0 Dt)\right) \end{aligned} \tag{A.32}$$

A.3. Numerical Solution of a Nonlinear Differential Equation

In general, the solution of a nonlinear differential equation with an arbitrary damping model has to be computed numerically. In the following section the numerical procedure for the computation of such an nonlinear second order differential equation is described. The nonlinearity is treated with Newton method and the time derivative is approximated with a Crank-Nicolson time integration scheme. The numerical procedure can be explained using the equation (A.33) (same as Eq. (3.7) in Sec. 3.1):

$$A_\phi \ddot{\phi} + \underbrace{B_1\dot{\phi} + B_2|\dot{\phi}|\dot{\phi} + B_3\dot{\phi}^3}_{B(\dot{\phi})} + \underbrace{C_1\phi + C_3\phi^3 + C_5\phi^5}_{C(\phi)} = M_\phi(t) \tag{A.33}$$

The linear coefficient A_ϕ denotes the moment of inertia, the roll damping $B(\dot{\phi})$ is modeled with a third order polynomial and the restoring moment $C(\phi)$ uses a fifth order taylor expansion. The term $M_\phi(t)$ on the right hand side is an external roll moment acting on the ship. In case of a roll decay test the right hand side is zero.

In a first step the order of equation (A.33) is reduced to first order. This is accomplished by isolating the highest derivative left side

$$\ddot{\phi} = -\frac{1}{A_\phi}\left(B_1\dot{\phi} + B_2|\dot{\phi}|\dot{\phi} + B_3\dot{\phi}^3 + C_1\phi + C_3\phi^3 + C_5\phi^5 - M_\phi(t)\right) \tag{A.34}$$

and using the following substitutions:

$$\begin{aligned}\phi &= z_1\\ \dot{\phi} &= \dot{z}_1 = z_2\\ \ddot{\phi} &= \dot{z}_2 = z_3\end{aligned}$$

Through this approach the second order differential equation (A.34) is transformed into a system of first order differential equations (A.35) and (A.36)).

$$\dot{z}_1 = z_2 \tag{A.35}$$

$$\dot{z}_2 = -\frac{1}{A_\phi}\left(B_1 z_2 + B_2|z_2|z_2 + B_3 z_2^3 + C_1 z_1 + C_3 z_1^3 + C_5 z_1^5 - M_\phi(t)\right) \tag{A.36}$$

Equation (A.37) notes the ODE system in vector notation. The Vector $\mathbf{z} = [z_1,\, z_2]^T = [\phi,\, \dot{\phi}]^T$ denotes the dynamic state of the rigid body. The function

$\mathbf{F}(\mathbf{z})$ on the right-hand side defines a nonlinear vector function, depending on the motion state $\mathbf{z}$ and the external moment $M_\phi(t)$.

$$\dot{\mathbf{z}} = \mathbf{F}(\mathbf{z}) \tag{A.37}$$

A numerical approximation of Eq. (A.37) can be computed iteratively with the Crank-Nicolson method (Eq. (A.38), [94]).

$$y^{n+1} = y^n + h\left(\frac{1}{2}f(t^n, y^n) + \frac{1}{2}f(t^{n+1}, y^{n+1})\right) \tag{A.38}$$

The implicit term $f(t^{n+1}, y^{n+1})$ in Eq. (A.38) cannot be computed directly but has also to be approximated with an iterative scheme.

The nonlinearity of $\mathbf{F}$ can be handled with the Newton method [94]. For this type of fix point iteration scheme, equation (A.37) has to be transformed into root form:

$$\mathbf{G}(\mathbf{z}) = \mathbf{F}(\mathbf{z}) - \dot{\mathbf{z}} = 0 \tag{A.39}$$

with

$$G(y^{n+1}) = y^{n+1} - y^n - h\left(\frac{1}{2}f(t^n, y^n) + \frac{1}{2}f(t^{n+1}, y^{n+1})\right) = 0 \tag{A.40}$$

This equation can be approximated with the Newton method ([94]):

$$\mathbf{z}^{n+1} = \mathbf{z}^n - \mathbf{\Phi}^{-1}(\mathbf{z}^n)\mathbf{F}(\mathbf{z}^n) \tag{A.41}$$

The symbol $\mathbf{\Phi}$ denotes the matrix derivative

$$\mathbf{\Phi} = \mathbf{I} - \frac{h}{2}\frac{\partial \mathbf{F}}{\partial \mathbf{z}^{n+1}} \tag{A.42}$$

which depends on the Jacobian matrix

$$\mathbf{J}(\mathbf{z}) = \frac{\partial \mathbf{F}}{\partial \mathbf{z}} = \begin{bmatrix} 0 & 1 \\ -\frac{1}{A_\phi}\left(C_1 + 3C_3 z_1^2 + 5C_5 z_1^4\right) & -\frac{1}{A_\phi}\left(B_1 + 2B_2\,\mathrm{sgn}(z_2) z_2 + 3B_3 z_2^2\right) \end{bmatrix} \tag{A.43}$$

The inverse of matrix $\mathbf{\Phi}$ can be calculated with the explicit expression (A.44) ([60]):

$$\mathbf{A}^{-1} = \begin{bmatrix} a & b \\ c & d \end{bmatrix}^{-1} = \frac{1}{|\mathbf{A}|}\begin{bmatrix} d & -b \\ -c & a \end{bmatrix} \tag{A.44}$$

Algorithm 1 shows the structure of the procedure implemented in a python ([95]). Most of the lines in the algorithm control the nested time-loop and Newton-iteration and the preparation of the required variables. The main computation

is done in line 10 which implements the computation of a new state vector $\mathbf{z}$ by applying an iteration step of the Newton method defined in equation (A.41).

Algorithm 1 Adaptive Newton Method for Nonlinear Differential Equation

1: set parameter
2: set initial state vector
3: **while** $t < T_{\text{end}}$ **do** ▷ main time loop
4: advance time step $t^{n+1} = t^n + \Delta t$
5: get excitation momement $M_\phi(t)$
6: set initial state vector for Newton Method $\mathbf{z}_{\text{old}}$
7: **while** $tol < err$ **do** ▷ Newton Iteration Loop
8: compute $\mathbf{F}(\mathbf{z}_{\text{old}})$
9: compute $\mathbf{\Phi}^{-1}(\mathbf{z}_{\text{old}})$
10: compute new state vector $\mathbf{z}_{\text{new}} = \mathbf{z}_{\text{old}} - \mathbf{\Phi}^{-1}(\mathbf{z}_{\text{old}})\mathbf{F}(\mathbf{z}_{\text{old}})$
11: compute relative error
12: update state vector $\mathbf{z}_{\text{old}} = \mathbf{z}_{\text{new}}$
13: **end while**
14: adapt time step size Δt
15: write state vector
16: **end while**

A.4. Simple Ikeda Method

During the initial phase of this study the so called 'simple Ikeda method' was investigated. The method applies the equations described in the section about Ikeda's component method (appendix A.1). The term 'simple' denotes the use of a fitted polynomial expression to determine the values of certain shape coefficients required for the computation of the roll damping coefficients. The computation procedure of the simple Ikeda method is available in form of a Fortran program code on the website `http://www.marine.osakafu-u.ac.jp/~lab15/roll_damping.html`. In order to use the method within this study the code was ported to a python script.

The simple Ikeda method was used for three purposes: To investigate its suitability for the prediction of roll damping of modern ship hulls, to evaluate the improvements of the new roll damping prediction method and as an design tool for the hull shape variation in an early stage of this study.

The application of the simple Ikeda method is shown in the following section. The method was used to compute the required change in the beam-to-draft coefficient B:T needed to achieve a change of $\pm 10\%$ in the roll damping coefficient. The computation of the range was conducted with the DTC hull. It showed that the dimensions of the large hull geometry exceeded the parameter limits of the Ikeda method.

Table A.1.: Input parameter for simple Ikeda method

L_{pp}	350.0	[m]
B	51.0	[m]
T	14.0	[m]
c_B	0.655	[1]
c_{mid}	0.987	[1]
CoG	0	[m]
$\hat{\phi}$	20.0	[°]
T_w	19.0	[s]
BK_{comp}	1	[boolean]
l_{BK}	5*14.85	[m]
b_{BK}	0.6	[m]

The required input parameter for the Ikeda method are listed in table A.1. In order to estimate the required change in beam-to-draft ratio both parameter were varied in such a way that the displacement was kept constant.

The initial value for the base shape of the DTC was $B{:}T_0 = 51/14 = 3.64$. This value was varied within the range limit ($B{:}T_i \in [2.5, 4.5]$) set by the rules of the Ikeda method. The displacement of the hull was estimated with the equation

$$\nabla = L_{pp} B\, T\, c_B = 164000 m^3$$

By keeping the displacement constant the expressions

$$T = \sqrt{\frac{\nabla}{L_{pp} B{:}T c_B}} \tag{A.45}$$

and

$$B = \frac{\nabla}{L_{pp} T c_B} \tag{A.46}$$

were used to compute the variation range for the draft and the beam of the hull. Figure A.5 shows the value of each damping components and their total value plotted over the for given $B{:}T$ range.

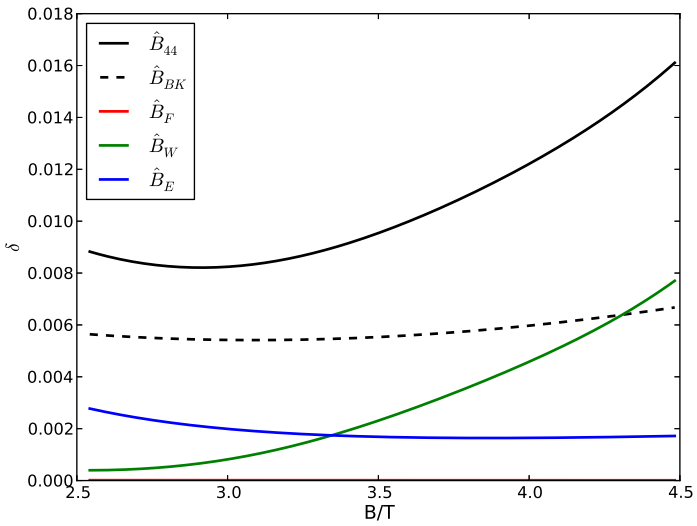

Figure A.5.: Roll damping components depending on the draft-to-beam ratio $B{:}T$

Finally the curve of the total roll damping coefficient $\hat{B}_{44}$ was used to determine that a 10% change of the roll damping coefficient should be achieved by using a $B{:}T$ ration of $B{:}T < 3.4$ or $B{:}T > 3.8$.

A.5. Parametric Bilge Keel Design

In order to automatically generate bilge keels for all hull shapes used in the systematic variation, another python script was implemented. The script uses the shape analysis methods described in Sec. 3.4 and a set of CAD tools [86] which can be controlled via a python interface (python-API).

Figure A.6 shows the construction details of the segmented bilge keel used for the DTC hull. Due to the curvature of the hull surface the positioning of the segments was particularly complicated. The orientation of the segments has to follow three design rules: the segments have to be aligned to the hull surface, the camber line has to be aligned to the flow direction and the bilge keel plate has to have a 90° angle to the hull surface in order to achieve the highest damping effect.

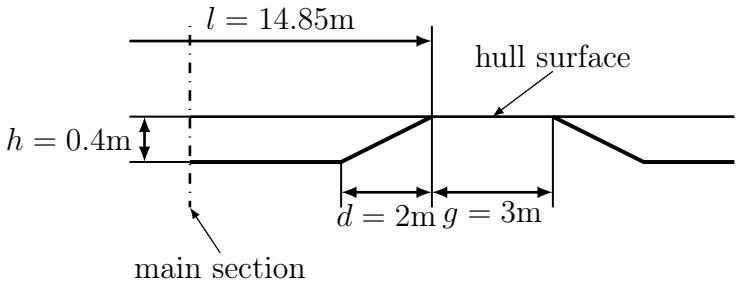

Figure A.6.: Construction details of the segmented bilge keel for the DTC hull

At the start of the python script the geometric parameter of the above described bilge keel are read from a configuration file containing, together with its general position and a path to the STL-file of the hull surface. A simple bilge keel plate is defined by height, length and thickness. In order to enable the generation of suitable prism layer cells with OpenFOAM, a coarser bilge keel geometry was used. The base of the bilge keel shown in Fig. A.7 is wider and the overall thickness is also larger. By this approach the mesh tool `snappyHexMesh` is better able to generate smoothly aligned prism cells around the bilge keel.

Figure A.7 shows the geometry of a segmented bilge keel constructed with the use of OpenCascade [86]. The CAD surface of one bilge keel segment is generated by defining vertices, connecting them with line elements. A closed curve of lines is then used to define the faces of the segment. In an additional step the edges of the CAD object can be rounded in order to create a smoother surface. For the use with `snappyHexMesh` rounded edges on very small geometry details like the the tip of a bilge keel may deteriorate the cell quality.

The camber line of the bilge keel segments can be defined either by the use of stream lines obtained from a previous flow computation or by a simple geometric

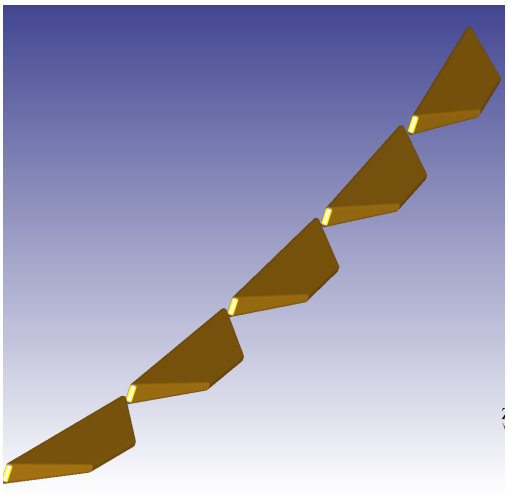

Figure A.7.: Parametric bilge keel design with OpenCascade

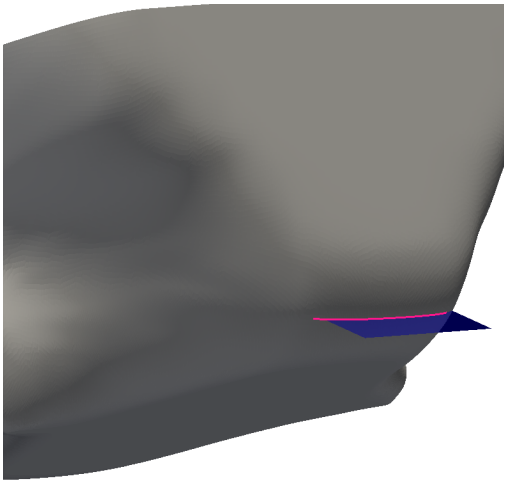

Figure A.8.: Bilge keel camber line and construction plane on feeder hull

operation. In the first case a streamline near the designated location of the bilge keel is picked and projected onto the hull surface. Bilge keel segments placed exactly along this projected line will only generate an additional drag force without a lift effect. By choosing a small inclination angle between the projected streamline and the base line of the bilge keel the resulting lift effect could be used to increase the restoring effect of the hull. But this effect would also add to the ship resistance.

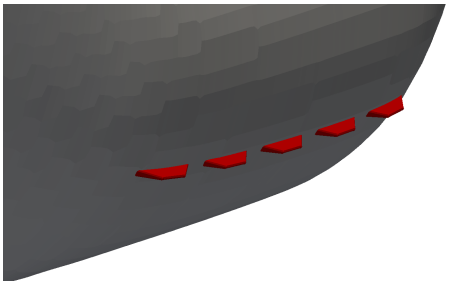

Figure A.9.: segmented bilge keel on DTC hull

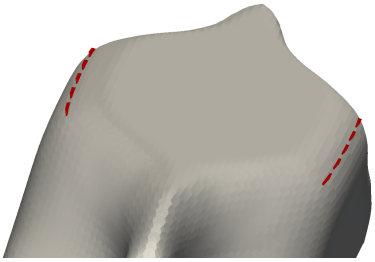

Figure A.10.: segmented bilge keel on DTC hull

A simpler method to find a suitable position and orientation for the bilge keel segments is shown in Fig. A.8. First a start point is defined at the center of the bilge radius on the main section of the hull. In the next step the coordinates of this point are used to define the position of a plane (blue plane in Fig. A.8)

perpendicular to the hull surface. The camber line of the bilge keel segments is then determined by computing the intersection (red line in Fig. A.8) of the plane and the hull surface.

In the last step the CAD objects of the segments are placed along the red camber line and are exported either to an IGES-file or in case of a simple bilge keel geometry (without rounded edges) directly to a STL-file. Figure A.9 and A.10 show the results of the of the described procedure. The shape of bilge keel segments (red) were created depending only on a few geometric parameters and were placed automatically on the DTC hull.

Bibliography

[1] Sarpkaya, T., and O'Keefe, J. L., 1996. "Oscillating flow about two and three-dimensional bilge keels". *Journal of Offshore Mechanics and Arctic Engineering*(118/1).

[2] Piehl, H., and el Moctar, O., 2015. "Development of a mathematical roll damping model with polynomial regression analysis". *Proceedings of the ASME 2015 34st International Conference on Ocean, Offshore and Arctic Engineering.*

[3] Piehl, H., and el Moctar, O., 2014. "Bilge keel forces and vortex shedding – a numerical analysis with openfoam". *Proceedings of the ASME 2014 33st International Conference on Ocean, Offshore and Arctic Engineering.*

[4] Piehl, H., and el Moctar, O., 2013. "Entwicklung von mathematischen Modellen zur Berechnung der Rolldämpfung moderner Schiffsformen – Mat-Roll / Best-Roll". *BMWi Forschungsprogramm – Schiffahrt und Meerestechnik für das 21. Jahrhundert; Abschlußbericht.*

[5] Piehl, H., and el Moctar, O., 2013. "Roll decay model test of a post panamax container ship – experimental and numerical analysis". *Proceedings of the ASME 2013 32st International Conference on Ocean, Offshore and Arctic Engineering.*

[6] Piehl, H., and el Moctar, O., 2012. "Vortex shedding from a bilge keel in a transient turbulent flow". *Proceedings of the ASME 2012 31st International Conference on Ocean, Offshore and Arctic Engineering.*

[7] Piehl, H., Höpken, J., and el Moctar, O., 2011. "Influence of shape variation on hydrodynamic damping of rigid body motion". *Proceedings of the 14th Numerical Towing Tank Symposium*(14).

[8] Ursell, F., 1948. "On the rolling motion of cylinders in the surface of a fluid". *Q. J. Mech. and Appl. Math.*(Vol. II, Pt. 3).

[9] Froude, W., 1862. "On the rolling of ships". *Transactions, Read at the Second Session of the Institute of Naval Architects.*

[10] el Moctar, O., Shigunov, V., and Zorn, T., 2012. "Duisburg test case: Post-panamax container ship for benchmarking". *Ship Technology Research*(Vol. 50, No. 3).

[11] Bass, D., and Haddara, M., 1988. "Nonlinear models of ship roll damping". *Int. Shipbuild. Progr. 35*(401).

[12] Spouge, J., 1987. "Non-linear analysis of large-amplitude rolling experiments". *Int. Shipbuild. Progr. 35*(403).

[13] Chan, H., Xu, Z., and Huang, W., 1995. "Estimation of nonlinear damping coefficients from large-amplitude ship rolling motions". *Applied Ocean Research*(17).

[14] Schmitke, R. T., 1978. "Ship sway, roll and yaw motions in oblique seas". *SNAME Transactions*(86).

[15] Roberts, J., 1985. "Estimation of nonlinear ship roll damping from free-decay data". *Journal of Ship Research*(29).

[16] Taylan, M., 1998. "The effect of nonlinear damping and restoring in ship rolling". *Ocean Engineering*(27).

[17] Umeda, N., Hashimoto, H., Vassalos, D., Urano, S., and Okou, K., 2004. "Nonlinear dynamics on parametric roll resonance with realistic numerical modelling". *Int. Shipbuild. Progr. 51*(2/3).

[18] Jang, T., Son, J., Han, S., Sung, H., Lee, S., and Shin, S., 2010. "A numerical investigation on nonparametric identification of nonlinear roll damping moment of a ship from transient response". *The Open Ocean Engineering Journal*.

[19] Cohen, I. M., and Kundu, P. K., 2004. *Fluid Mechanics*. Academic Press; 3 edition.

[20] Hirt, C. W., and Nichols, B. D., 1981. "Volume of fluid (vof) method for the dynamics of free boundaries". *Journal of Computational Physics*(39,201-225).

[21] Pope, S. B., 2000. *Turbulent Flows*. Cambridge University Press.

[22] Schlichting, H., and Gersten, K., 2006. *Grenzschicht-Theorie*. Springer; 10 edition.

[23] Ferziger, J. H., and Peric, M., 2010. *Computational Methods for Fluid Dynamics*. Springer; 3 edition.

[24] Versteeg, H. K., and Malalasekera, W., 2007. *Computational Fluid Dynamics.* Prentice Hall; 2 edition.

[25] Salvesen, N., Tuck, E., and Faltinsen, O., 1970. "Ship motions and sea loads". *Society of Naval Archictects and Marine Engineers*(12-13).

[26] Salvesen, N., 1978. "Added resistance of ships in waves". *Journal of Hydronautics*(12(1):24-34).

[27] Zhang, X., and Beck, R. F., 2007. "Computations for large amplitude two-dimensional body motions". *Journal of Engineering Mathematics*(58,1-4).

[28] Jaouen, F., Koop, A., Vaz, G., and Crepier, P., 2011. "Rans predictions of roll viscous damping of ship hull sections". *International Conference on Computational Methods in Marine Engineering.*

[29] Graham, J., Sherwin, S., and Kendon, T., 2005. "The prediction of viscous damping of large floating bodies in waves". *20th International Workshop on Water Waves and Floating Bodies.*

[30] Kluwe, F., and Schmode, D., 2005. "Rans based analysis of roll damping moments at bilge keels". *Numerical Towing Tank Symposium.*

[31] Bonfiglio, L., Brizzolara, S., and Chryssostomidis, C., 2011. "Added mass and damping of oscillating bodies: a fully viscous numerical approach". *Recent Advances in Fluid Mechanics, Heat & Mass Transfer and Biology.*

[32] Graham, J., and Cozens, P., 1988. "Vortex shedding from edges including viscous effects". *Fluid Dynamics Research*(3).

[33] Brown, D., and Patel, M., 1985. "A theory for vortex shedding from the keels of marine vehicles". *Journal of Engineering Mathematics*(19).

[34] Seah, R., Celano, T., and Yeung, R. "The roll decay of floating cylinders with bilge keels".

[35] Blume, P., 1979. "Experimentelle Bestimmung von Koeffizienten der wirksamen Rolldämpfung und ihre Anwendung zu Abschätzung extremer Rollwinkel". *Schiffstechnik*(26).

[36] Ali, B., Katayama, T., and Ikeda, Y., 2004. "Roll damping characteristics of fishing boats with and without drift motion". *Int. Shipbuild. Progr 51*(2/3).

[37] Tanaka, N., and Kitamura, H. "A study on the bilge keels part 1".

[38] Tanaka, N., and Kitamura, H., 1958. "A study on the bilge keels part 2. full sized model experiment".

[39] Tanaka, N., 1959. "A study on the bilge keels part 3. the effect of the ship form and the bilge keel size on the action of the bilge keel".

[40] Tanaka, N., 1960. "A study on the bilge keels part 4. on the eddy-making resistance to the rolling of a ship hull".

[41] Ikeda, Y., Himeno, Y., and Tanaka, N., 1976. "Report no. 401: On roll damping force of ship - effect of friction of hull and normal force of bilge keels -". *Journal of the Kansai Society of Naval Architects*(161).

[42] Aloisio, G., and Felice, F., 2006. "Piv analysis around the bilge keel of a ship model in free roll decay".

[43] Irvine, M., Longo, J., and Stern, F., 2004. "Towing-tank tests for surface combatant for free roll decay and coupled pitch and heave motions". *25th Symposium on Naval Hydrodynamics.*

[44] Larsson, L., and Visonneau, M., 2010. "Proceedings gothenburg 2010, a workshop on numerical ship hydrodynamics". *Chalmers University of Technology, Report No. R-10:122, Gothenburg.*

[45] Himeno, Y., 1981. "Prediction of ship roll damping – state of the art". *Report of Department of Naval Architecture & Marine Engineering, University of Michigan*(239).

[46] Ikeda, Y., Komatsu, K., and Yoji Himeno, N. T., 1977. "Report no. 402: On roll damping force of ship - effect of hull surface pressure created by bilge keels -". *Journal of the Kansai Society of Naval Architects*(165).

[47] Ikeda, Y., Himeno, Y., and Tanaka, N., 1977. "Report no. 403: On eddy making component of roll damping force on naked hull". *Journal of the Kansai Society of Naval Architects*(142).

[48] Ikeda, Y., Himeno, Y., and Tanaka, N., 1978. "Report no. 404: Components of roll damping of ship at forward speed". *Journal of the Kansai Society of Naval Architects*(143).

[49] Ikeda, Y., Himeno, Y., and Tanaka, N., 1978. "Report no. 405: A prediction method for ship roll damping".

[50] Ikeda, Y., Fujiwara, T., Himeno, Y., and Tanaka, N., 1978. "Report no. 406: Velocity field around ship hull in roll motion". *Journal of the Kansai Society of Naval Architects*(171).

[51] Kato, H., 1965. "Effect of bilge keels on the rolling of ships". *Society of Naval Architects of Japan*(117:93-114).

[52] Tamiya, S., and Komura, T., 1972. "Topics on ship rolling characteristics with advance speed". *Society of Naval Architects of Japan*(132).

[53] Kawahara, Y., Maekawa, K., and Ikeda, Y., 2008. "Characteristics of roll damping of various ship types and a simple prediction formula of roll damping on the basis of ikeda's method". *The 4th Asia-Pacific Workshop on Marine Hydrodynamics.*

[54] Kawahara, Y., Maekawa, K., and Ikeda, Y., 2010. "A simple prediction formula of roll damping of conventional cargo ships on the basis of ikeda's method and its limitations". *Proceedings of the 10th International Conference on Stability of Ships and Ocean Vehicles.*

[55] Bertin, L. E., 1874. "Données théoriques et expérimentales sur les vagues et le roulis". *Naval Science*(III, p.198).

[56] Molland, A. F., 2008. *The Maritime Engineering Reference Book.* Butterworth Heinemann.

[57] Mesbahi, E., Inzunza, M. S., Brink, K.-E., and Bertram, V., 2001. "Empirical roll damping formula derived by artificial neural network applications". *Jahrbuch der Schiffbautechnischen Gesellschaft*(November, Springer).

[58] Xing, Z., and McCue, L., 2011. "Modeling ship equations of roll motion using neural networks". *Naval Engineers Journal*(122: 49–60).

[59] Han, S., and Kinoshita, T., 2012. "Stochastic inverse identification of nonlinear roll damping of a ship moving at nonzero-forward speeds". *Mathematical Problems in Engineering.*

[60] Bronstein, I. N., and Semendjajew, K. A., 2000. *Taschenbuch der Mathematik.* Teubner.

[61] Dalzell, J. F., 1978. "A note on the form of ship roll damping". *Journal of Ship Research*(22,pp. 178-185).

[62] Python module numpy.fft: Discrete fourier transform. http://docs.scipy.org/doc/numpy/reference/routines.fft.html. Online; accessed 2014-06-01.

[63] Python Module scipy.interpolate.splrep: 1-D B-spline representation. http://docs.scipy.org/doc/numpy/reference/routines.fft.html. Online; accessed 2014-06-01.

[64] Python Module scipy.optimize.leastsq: Nonlinear Least Squares . https://docs.scipy.org/doc/scipy/reference/generated/scipy.optimize.leastsq.html. Online; accessed 2015-11-05.

[65] Schumacher, A., 2010. *Rolldämpfungsversuche mit dem Modell eines großen Containerschiffes, Teilvorhaben Mat-Roll.* Bericht Nr. S 625/10. Hamburgische Schiffbau-Versuchsanstalt.

[66] Open source: Visualization toolkit vtk. http://www.vtk.org/. Online; accessed 2014-06-01.

[67] Biran, A., 2003. *Ship Hydrostatics and Stability.* Butterworth-Heinemann.

[68] Liu, Y. J., 2009. *Fast Multipole Boundary Element Method: Theory and Applications in Engineering.* Cambridge University Press; 1 edition.

[69] Liu, Y. J., and Nishimura, N., 2006. "The fast multipole boundary element method for potential problems: A tutorial". *Engineering Analysis with Boundary Elements, 30, No. 5, 371-381.*

[70] Open Source CFD Toolbox: OpenFOAM. www.openfoam.com. Online; accessed 2014-06-01.

[71] CD-adapco: StarCCM+. http://www.cd-adapco.com/. Online; accessed 2014-06-01.

[72] Jasak, H., 1996. "Error Analysis and Estimation for the Finite Volume Method with Applications to Fluid Flows". PhD Thesis, Imperial College. URL http://powerlab.fsb.hr/ped/kturbo/OpenFOAM/docs/HrvojeJasakPhD.pdf.

[73] Rusche, H., 2002. "Computational fluid dynamics of dispersed two-phase flows at high phase fractions". PhD Thesis, Imperial College. URL http://powerlab.fsb.hr/ped/kturbo/OpenFOAM/docs/HenrikRuschePhD2002.pdf.

[74] Menter, F. R., 1994. "Two-equation eddy-viscosity turbulence models for engineering applications". *AIAA Journal*(Vol. 32, No. 8, pp. 1598-1605).

[75] CFD-Online forum, Nov/2015: Turbulence free-stream boundary conditions. `https://www.cfd-online.com/Wiki/Turbulence_free-stream_boundary_conditions`. Online; accessed 2015-11-05.

[76] Jasak, H., Weller, H., and Gosman, A., 1999. "High resolution nvd differencing scheme for arbitrarily unstructured meshes". *International Journal for Numerical Methods in Fluids,* ***31***(2), pp. 431–449.

[77] Abbott, I., and Von Doenhoff, A., 1959. *Theory of Wing Sections: Including a Summary of Airfoil Data.* Dover Publ.

[78] Nietzschmann, T., 2010. *Widerstands- und Propulsionsversuch für das Modell eines Containerschiffes.* Bericht Nr. 3733. Schiffbau-Versuchsanstalt Potsdam.

[79] "ITTC", 1957. "Proceedings of the 8th international towing tank conference". *International Towing Tank Conference.*

[80] Querard, A., Temarel, P., and Turnock, S., 2010. "Application of rans to hydrodynamics of bilge keels and baffles". *William Froude Conference on Advances in theoretical and applied hydrodynamics – Past and Future, Portsmouth, GB.*

[81] Kinnas, S. A., Yu, Y.-H., Lee, H., and Kakar, K., 2003. "Modeling of oscillating flow past a vertical plate". *Proceedings of The Thirteenth (2003) International Offshore and Polar Engineering Conference.*

[82] Morison, J. R., O'Brien, M. P., Johnson, J. W., and Schaaf, S. A., 1950. "The force exerted by surface waves on piles". *Petroleum Transactions*(189,149-154).

[83] Keulegan, G. H., and Carpenter, L. H., 1958. "Forces on cylinders and plates in an oscillating fluid". *Journal of Research of the National Bureau of Standards*(Vol. 60, No. 5).

[84] el Moctar, O., Kaufmann, J., Ley, J., Oberhagemann, J., Shigunov, V., and Zorn, T., 2010. "Prediction of ship resistance and ship motions using ranse". *Proceedings of the Gothenburg Workshop, Gothenburg, Sweden.*

[85] Oberhagemann, J., and el Moctar, O., 2012. "Numerical and experimental investigations of whipping and springing of ship structures". *International Journal of Offshore and Polar Engineering,* ***22***(2).

[86] Open source: Opencascade. `www.opencascade.org/`. Online; accessed 2014-06-01.

[87] Gschaider, B. Groovy bc openfoam extension libraries. `www.openfoamwiki.net/index.php/Contrib\_groovyBC`. Online; accessed 2013-09-12.

[88] Bühlmann, P., 2007. Computational Statistics. ETHZ Lecture Notes.

[89] Hastie, T., Tibshirani, R., and Friedman, J., 2001. *The Elements of Statistical Learning*. Springer.

[90] Venables, W., and Ripley, B., 2002. *Modern Applied Statistics With S*. Springer; Auflage: 4th ed. 2002.

[91] Open Source: Python interface to the R Programming Language. `http://rpy.sourceforge.net/`. Online; accessed 2014-06-01.

[92] Open source: The r project for statistical computing. `http://www.r-project.org/`. Online; accessed 2014-06-01.

[93] Fujino, M., Ida, T., Maeto, T., and Numata, T., 1979. "A consideration on the hydrodynamic normal forces acting on the bilge keel". *Journal of the Society of Naval Architects of Japan*(144).

[94] Schwarz, H. R., and Koeckler, N., 2011. *Numerische Mathematik*. Vieweg+Teubner.

[95] Wikibooks: Methods for Nonlinear Ordinary Differential Equations. `https://en.wikibooks.org/wiki/Parallel_Spectral_Numerical_Methods/Nonlinear_Ordinary_Differential_Equations_and_Iteration`. Online; accessed 2015-11-05.